

Carbon nanofiber supported nickel catalysts

Martijn van der Lee

ISBN:

Cover printed by Betuwe ProMedia Creation

Drukkerij Ponsen & Looijen, Wageningen

Carbon nanofiber supported nickel catalysts

Koolstofvezels als dragermateriaal voor
nikkelkatalysatoren

(met een samenvatting in het Nederlands)

Proefschrift

ter verkrijging van de graad van doctor aan de Universiteit Utrecht op
gezag van de Rector Magnificus, Prof. Dr. W. H. Gispen, ingevolge het
besluit van het College voor Promoties in het openbaar te verdedigen op
woensdag 19 oktober 2005 des middags te 16:15 uur

door

Martijn Klaas van der Lee

Geboren op 19 juni 1973 te Tilburg

Promotor: Prof. Dr. Ir. K.P. de Jong
Department of Inorganic Chemistry and Catalysis, Debye
Institute, Utrecht University, Utrecht, the Netherlands

Co-promotor: Dr. J.H. Bitter
Department of Inorganic Chemistry and Catalysis, Debye
Institute, Utrecht University, Utrecht, the Netherlands

The work described in this thesis was financially supported by:
Technologiestichting STW - grant UPC 5487.

There are only two ways to live your life.
One is as though nothing is a miracle.
The other is as though everything is a miracle.

Albert Einstein

Contents

Chapter 1:	Introduction to methanation and carbon nanofibers	1
Chapter 2:	Catalytic growth of macroscopic carbon nanofiber bodies with high bulk density and high mechanical strength	15
Chapter 3:	Synthesis of well-dispersed, highly loaded nickel on carbon nanofibers – Preliminary studies	35
Chapter 4:	Deposition precipitation for the preparation of carbon nanofiber supported nickel catalysts – Study on the mechanism	47
Chapter 5:	Sintering of carbon nanofiber supported nickel catalysts used for methanation	73
Chapter 6A:	Summary and concluding remarks	97
Chapter 6B:	Samenvatting en conclusies	101
	Dankwoord	107
	Curriculum Vitae	111

1

Introduction to methanation and carbon nanofibers

Energy demand

The availability of energy is one of the key elements of modern society. It is expected that the energy demand of the society will drastically grow [1]. This is caused by two main reasons i.e., the increasing population, which should reach 10 to 12 billion people by the year 2100 [1] as compared to 6.4 billion in 2005 and the higher energy needs of the developing countries to improve their living standard. Figure 1 indicates the worldwide energy demand and shows a prognosis for the next 2 decades [2].

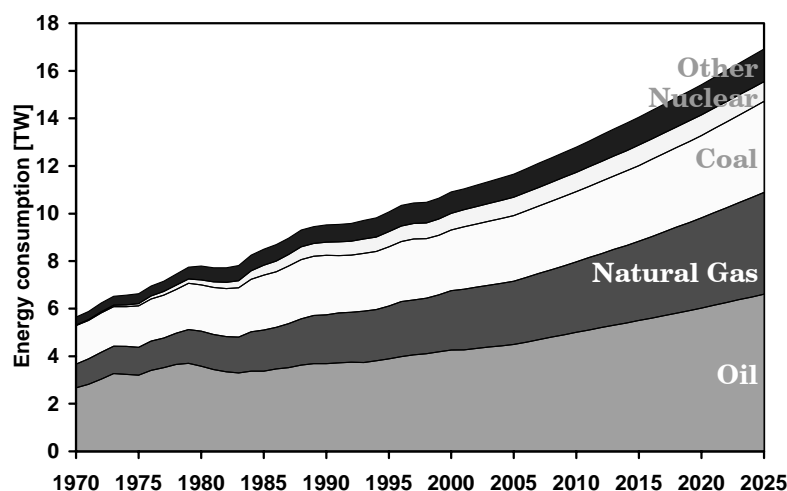


Figure 1: Worldwide energy consumption development.

Irrespective of the availability of natural energy sources saving energy and developing new, environmentally benign, energy is a must for future society. One of the environmentally friendly options is the use of renewable energy sources. In that way energy is produced without negatively affecting nature.

Use of biomass as energy source

The Dutch government has decided by legislation that in the year 2020 10% of the total energy consumption in the Netherlands must originate from renewable sources with 42% from biomass [3,4]. Biomass is a generic term for all organic material a.o. wood, grass and plants and is mainly build up from cellulose type of units ($C_6H_6O_6$) and water. One way to produce energy from biomass is its gasification to synthesis gas, a mixture of carbon monoxide and hydrogen followed by conversion of the synthesis gas to methane or so-called renewable natural gas. The product distribution of CO hydrogenation is tunable via the catalyst used. Nickel is known to show a high selectivity toward methane [5] while iron and cobalt shows a preferred formation of higher hydrocarbons (Fischer Tropsch synthesis [6]). The application of the above sketched process i.e., conversion of biomass into fuels has a few advantages. When applied on large-scale CO hydrogenation is an efficient process in which heat is released [7] that can be used for power generation.

In addition, the methane produced in the above describe process can be, after purification, directly injected into the currently available gas distribution grid thus no new infrastructure is needed. The individual steps, from biomass to renewable natural gas, are schematically shown in Figure 2. The typical composition of the product leaving the gasification reactor is given in Table 1.

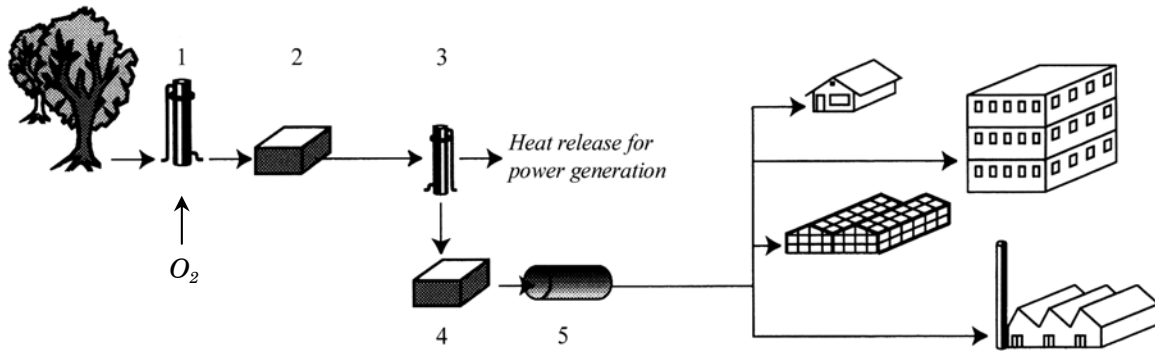


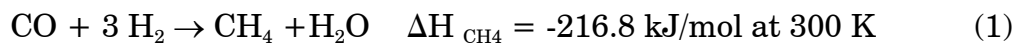
Figure 2: Schematic representation of the processes needed to the production and use of renewable natural gas. 1) gasification of biomass to synthesis gas; 2) gas cleanup (dust, sulfur, nitrogen removal); 3) methanation; 4) pressure control; 5) injection into the distribution grid [7].

Table 1: Gas composition of gasification of biomass after purification.

Gas	Composition [vol%]
CH ₄	0-10
H ₂	20-40
CO	40-55
CO ₂	5-20
N ₂	0-1
H ₂ O	3-12

Thermodynamics of methanation

The methanation reaction is the hydrogenation of carbon monoxide to methane according to:



As can be seen in Table 1 the H₂/CO ratio of the synthesis gas emerging from the gasification reactor is too low to be directly suitable for methanation. However the hydrogen concentration of the gas can be enhanced via the water-

gas shift reaction. Produced steam from the methanation may react with CO to hydrogen and CO₂:

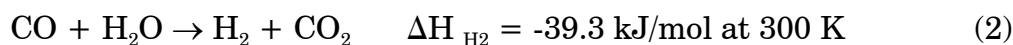


Figure 3A shows the thermodynamical equilibrium composition of the H₂/CO/CO₂/CH₄/H₂O system with input H₂/CO=3/1. Clearly upto 550 K the equilibrium favors methane. Therefore methanation is favored at low temperatures; however, for two reasons the temperature should not be too low. First at low temperature the reaction rates are low i.e. the kinetics are slow and therefore large residence times of the reactants in the reactor are needed to achieve high conversions. In addition at lower temperature the formation of volatile Ni(CO)₄ is favored, in case nickel catalysts are used, (see Figure 3B) which is a highly toxic compound [9]. Thus the optimal operating window for methanation is in the range of 500 to 600 K.

The methanation reaction is exothermic resulting in substantial heat production during the reaction. We calculated that the adiabatic temperature rise to convert 1% CO and 3% H₂ in N₂ to methane at 600 K and 1 bar results in a temperature rise of 77 K. Therefore, heat transport from the catalyst bed and the reactor must be fast. Therefore the choice of reactor and catalyst is very important and will be discussed below.

Methanation – state of the art

The methanation process has been studied extensively in the last 50 years. The aims were to understand and develop catalysts suitable for protecting the iron catalyst in the ammonia synthesis process (Haber-Bosch process) [10]. The hydrogen used always contains traces of CO, since it is formed via reforming and/or partial oxidation of hydrocarbons [10]. These traces of CO are a strong poison to the iron catalysts and need therefore be removed. One elegant way is to convert it with the available hydrogen to methane. The latter compound is harmless to the iron catalyst. For this process different active heterogeneous catalysts are available. Methanation catalysts are based on iron, cobalt, nickel, ruthenium, rhodium, palladium, osmium, iridium or platinum [11]. Since nickel is active and highly selective towards methane and nickel is among the cheapest active phases it is selected as active phase for the bulk methanation process. For methanation nickel can be supported on oxides such as alumina, zirconia, titania and silica [5,13].

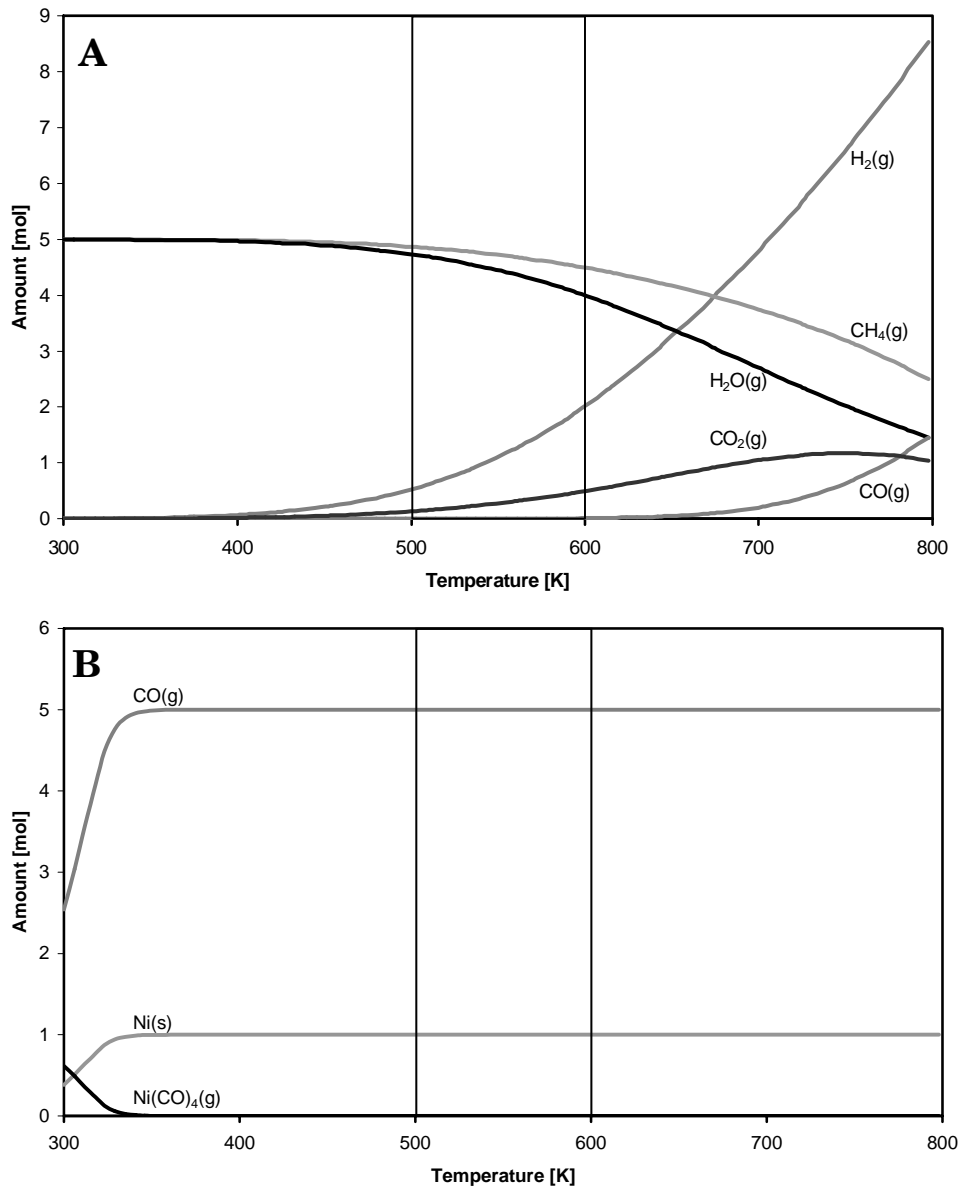


Figure 3: Calculated equilibrium composition at 1.0 bar for (A) CO/H₂/CH₄ input: CO= 5 mol; H₂= 15 mol; CH₄= 0 mol; CO₂= 0 mol and (B) CO/Ni/Ni(CO)₄ input: CO= 5 mol; Ni= 1 mol; Ni(CO)₄= 0 mol.

Bulk methane production and reactor choice

As stated above, the methanation reaction is highly exothermic thus large amounts of heat have to be removed from of the reactor. In this paragraph a comparison will be made between a multi tubular and a fluidized bed reactor.

When we assume that a methanation plant produces $800 \cdot 10^6 \text{ Nm}^3$ per year the related methanation produces $8 \cdot 10^{15}$ Joule of energy per year. The cooling surface area needed the transfer this heat can be calculated by equation 1 [12].

$$A = \frac{Q_{heat}}{h_w \cdot (T_c - T_w)} \quad (1)$$

Q_{heat} is the amount of heat produced per second [W], h_w is the heat transfer coefficient, for fixed bed reactor about 10 [W/m²K], T_c is the temperature of the catalyst [K] and T_w the temperature reactor wall [K]. The difference ($T_c - T_w$) is estimated to be 20 K. According to equation 1 a cooling surface area of about 10⁶ m² is required.

Figure 4 shows a drawing of a multi tubular reactor (MTR) of 5 meter in diameter and 10 meter high. Inside this reactor about 5000 tubes are present each with a diameter of 0.05 meter. Such an individual tube has an external area of 1.6 m². For the methanation process 10⁶ / 1.6 ≈ 600 000 individual reactor pipes are needed to provide the desired cooling area. With 5000 pipes per reactor 120 MTR units are needed in this methanation plant.

In a fluid bed reactor the h_w is estimated to be about 1000 times as high as that of the fixed bed reactor [12]. If we consider the same size of reactor, 5 meters wide and 10 meters high wherein 2000 cooling tubes present (tubes with the same diameter as in the MTR setup). The methanation reaction requires then 6000 cooling tubes with corresponds to 3 fluidized bed reactors units to run the same reaction. Thus much smaller equipment can be used with a fluid bed reactor for the same conversion and heat flux as compared to a multi tubular reactor.

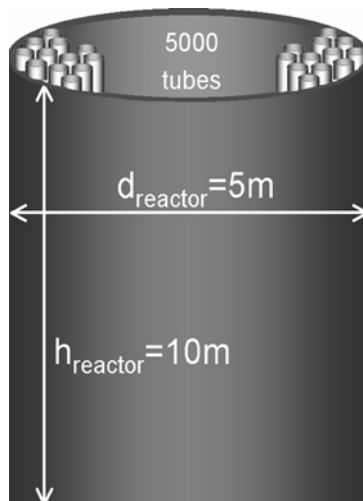


Figure 4: Schematic drawing of a multi tubular reactor equipped with individual tubes.

Consequences of reactor choice

Since in fixed bed reactor the catalyst on the lower part of the reactor, to a certain extent, have to carry the weight of the particles on top strong catalyst particles are needed in order to prevent crushing of the particles in the lower part. In fluid bed reactors the catalysts have to deal with be attrition when the catalyst particles swirl around and may break by collisions with other particles and the reactor wall. For both reactor types mechanically strong catalysts are mandatory.

Bulk methanation with conventional nickel catalysts

For silica supported nickel catalysts, silica reacts with steam and forms mobile $\text{Si}(\text{OH})_4$ species whereby the support structure is damaged thereby loosing surface area [14]. Alumina-supported nickel catalysts deactivate fast by coke formation and sintering [5]. Also spinel formation is possible resulting in the loss of activity [15,16]. Nickel on titania is more stable, however, this catalyst is less selective towards methane (~60%) whereas nickel on alumina results in about 80% methane selectivity and nickel on silica results in 95% CH_4 selectivity [5,13].

Carbon nanofibers as support material might have advantages with respect to steam stability and mechanical strength [16-24] thus are suitable for methanation catalysts. This thesis will focus on the outlook of Ni/CNF as catalyst for methanation.

Carbon nanofibers

Carbon nanofibers are graphite like materials with a high aspect ratio. The diameter is in the nanometer range 10-100 nm and the length can be up to 1 mm. Initially the research on carbon nanofibers was to prevent their formation during hydrocarbon conversion/synthesis reactions e.g., Fischer Tropsch synthesis and steam-methane reforming [25]. About 10-15 years ago the unique properties of the carbon nanofibers like its inertness and strength were noted and appreciated [19-22]. The discovery of carbon nanotubes in 1991 by Iijima turned the research objective from preventing the fiber growth to controlling the growth and therewith the properties of the created fibers [27].

The carbon nanofibers, which can be prepared as macroscopic skeins of intertwined individual microscopic nanofibers, have unique properties which make them potentially suitable as catalyst support [16-26]. CNF skeins are strong, do not show microporosity and can be prepared without contaminants such as sulphur. In addition the surface composition of the CNF surface can be chemically tuned [16,18,19,28].

Mechanism of growth and the carbon nanofiber structures

To our opinion the most convenient way to prepare CNF, especially on a large scale, is via catalytic growth i.e. a hydrocarbon is decomposed over a metal surface in order to form the fiber. This process involves a number of steps: first the hydrocarbon decomposes on the metal surface. Next the carbon atoms diffuse through/over the metal surface in order to segregate on the other side of the metal particle thus forming CNF [17,18,26].

Nickel, iron and cobalt are most often used, since those metals can form metal carbides. The carbon sources, which are most often used, are methane, CO, ethyne and ethane [17,18,22,29-33]. Growth process temperatures are in the range of 650 K to 1150 K. In this way fibers can be collected with a diameter between 10 and 100 nm and length up to 1 mm.

The growth of carbon nanofibers is studied extensively in the last decades. De Jong and Geus [18] have reviewed this subject. The structure of the individual fibers grown is depending on the kind of metal, reaction (growth) temperature and the carbon containing gas [18,34]. The combination between nickel and CO/H₂, as used in the current study, leads to the formation of fishbone type carbon nanofiber. Whereas for example iron leads in general to the formation of carbon nanotubes. Those two types of carbon materials are shown in Figure 6.

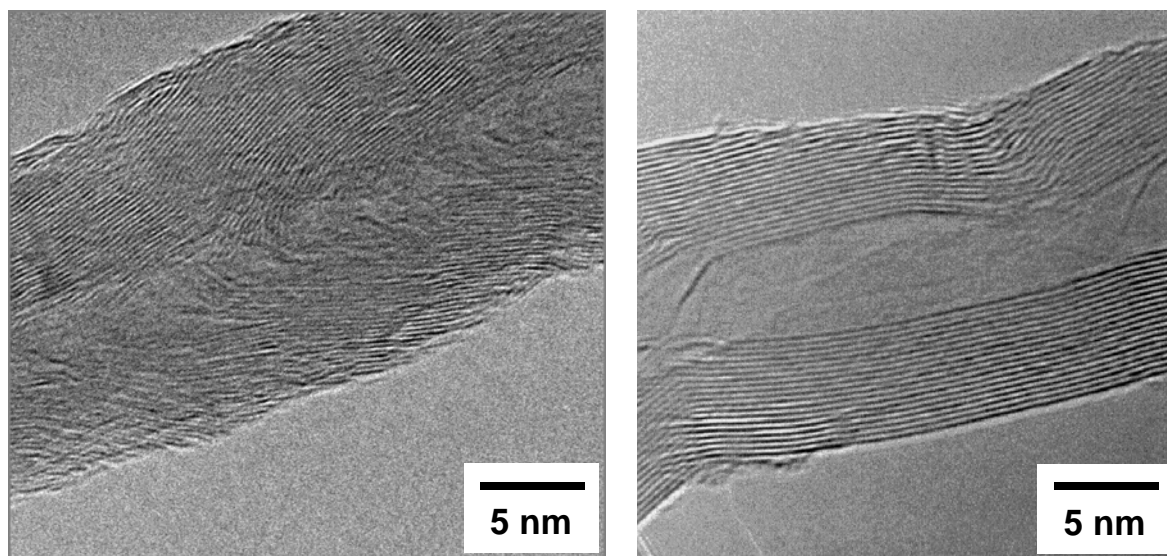


Figure 6: Left a TEM image of a fishbone type carbon nanofiber is shown and right an image of multi walled carbon nanotube is depicted [18].

Preparation of metal based CNF catalysts

After growth of the carbon nanofibers the material is hydrophobic. This non-polar surface can be changed by a chemical oxidation treatment, for example a reaction with an oxidizing agent, e.g. nitric acid and/or sulfuric acid [19,25,28]. As a result of that oxygen containing groups can be introduced to the surface. These groups ensure wettability of the surface by polar solvents (like water) and provide anchoring site for the catalyst precursor and the final catalytic phase. During this fiber treatment a wide range of oxygen containing groups are formed which can be acidic, neutral and basic in nature. Figure 7 shows some oxygen groups, which are introduced to the surface by oxidation. In water those surface groups can be protonated or deprotonated depending on the pH of the solution and their pK_a value. Overall the oxidized carbon nanofibers in water have an iso-electric point of about 2-3 [19] so above this pH the support is mainly negatively charged and interacts strongly with cationic species [35].

In general, the creation of an active phase on a support can be realized by different techniques, a.o., dry or wet impregnation, ion adsorption and deposition precipitation. Some of those preparation techniques can be applied to carbon nanofibers too. However, for example deposition precipitation onto carbon nanofibers seems to be less obvious.

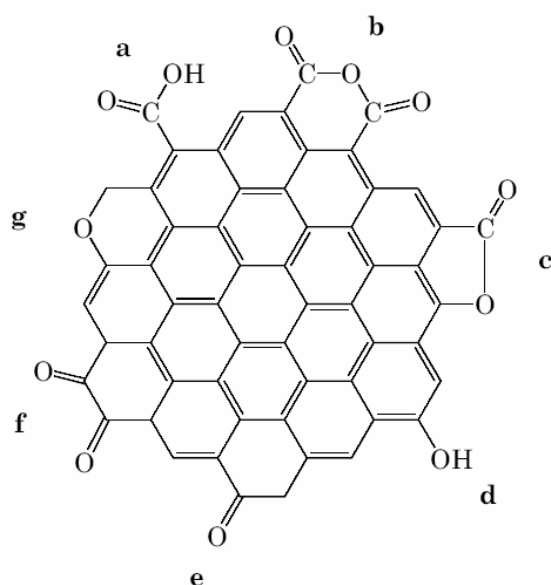


Figure 7: Different oxygen-containing surface groups on carbon. a) carboxyl groups, b) carboxylic anhydride groups, c) lactone groups, d) phenol groups, e) carbonyl groups, f) quinone groups, g) xanthene or ether groups [25].

Scope and outline of this thesis

Aim of the work described in this thesis is the exploration of carbon nanofibers as support material for metallic nickel, to create new catalyst suitable for bulk production of renewable natural gas from concentrated synthesis gas streams.

Chapter 2 describes the preparation of carbon nanofiber bodies with a high mechanical strength and high bulk density. The bulk density is an important property of the support material from a commercial point of view. The higher the bulk density the more efficient a reactor volume is used. This chapter describes a macroscopic carbon nanofiber growth mechanism based on the microscopic mechanism described in this introduction chapter.

Chapter 3 describes the possibilities and shortcomings of preparation techniques like incipient wetness impregnation and deposition precipitation applied to hydrophilic carbon nanofibers. This chapter describes how to create a highly dispersed and highly loaded nickel catalyst on carbon nanofibers. We found that the deposition precipitation, surprisingly, is also suitable to prepare nickel onto carbon nanofibers.

Chapter 4 is an extended study about the deposition precipitation process. The mechanism in which nickel hydroxide is precipitated on the oxidized carbon nanofibers is investigated and compared to the mechanism of deposition precipitation of nickel onto silica.

Chapter 5 deals with the methanation process and sintering and deactivation of the nickel catalyst during time on stream. Since this exothermic methanation reactions runs at temperatures above 500 K, thermal stability of catalysts were investigated up to 773 K. Since thermal sintering did not play a role, chemical sintering via Ostwald Ripening was examined.

Finally, in Chapter 6 a summary of the results of the previous chapters is given and some concluding remarks are presented.

References

1. World Population Data Sheet, Population Reference Bureau, 1875 Connecticut Ave., NW, Suite 520. Washington, DC 20009-5728 USA, (2004), 1-16.
2. International Energy Agency (IEA) - World Energy Outlook, Report (2004).
3. Gastec NV, Apeldoorn- Internal publication.
4. Report on “Groene stroom”, Algemene Rekenkamer, the Netherlands, (2003).
5. Vannice, M.A., Garten, R.L., *J. Catal.*, (1979), 56, 236.
6. Rodriguez-Reinoso, F., De Dios López-González, J., Moreno-Castilla, C., Guerrero-Ruiz, A., Rodriguez-Ramos, I., *Fuel*, (1984), 63, 1089.
7. Gastec, De toekomst voor een efficiënt gebruik van biomassa - duurzaam gas, Gastec NV Apeldoorn, the Netherlands.
8. Sutton, D., Kelleher, B., Ross, J.R.H., *Biomass Bioenerg.*, (2002), 23, 209.
9. Material Safety Data Sheet - Safety (MSDS) data for nickel carbonyl, PEL 0.001 ppm.
10. “Catalysis: An Intergrated Approach – Second, revised and enlarged edition”, (Van Santen, R.A., Van Leeuwen, P.W.N.M., Moulijn, J.A., Averill, B.A., Eds.), NIOK, Elsevier, (1999).
11. Takenaka, S., Shimizu, T., Otsuka, K., *Int. J. Hydrogen Energ.*, (2004), 29, 1065.
12. Perry chemical engineers handbook 7th edition (Perry, R., Green, D.W., Eds.), (1997).
13. Van de Loosdrecht, J., Van der Kraan, A.M., Van Dillen, A.J., Geus, J.W., *J. Catal.*, (1997), 170, 217.
14. Sato, S., Takahashi, R., Sodesawa, T., Kobayashi, C., Miura, A., Ogura, K., *Phys. Chem. Chem. Phys.*, (2001), 3, 885.
15. Twigg, M.V., Richardson, J.T., *Appl. Catal. A-Gen.*, (2000), 190, 61.
16. Xu, Z., Li, Y., Zhang, J., Chang, L., Zhou, R., Duan, Z., *Appl. Catal. A-Gen.*, (2001), 210, 45.
17. Turlier, P., Dalmon, J.A., Martin, G.A., *Stud. Surf. Sci. Catal.*, Elsevier, Amsterdam, (1982), 203.
18. De Jong, K.P., Geus, J.W., *Catal. Rev.–Sci. Eng.*, (2000), 42, 481.
19. Hoogenraad, M.S., Ph.D. thesis, Utrecht University, Utrecht, the Netherlands, (1995).

20. Hoogenraad, M.S., Onwezen, M.F., Van Dillen, A.J., Geus, J.W., *Stud. Surf. Sci. Catal.*, (1995), 101, 1331.
21. Geus, J.W., Hoogenraad, M.S., Van Dillen, A.J., in "Synthesis and Properties of Advanced Catalytic Materials" (Iglesia, E., Lednor, P.W., Nagaki, D.A., Thompson, L.T., Eds.), *Materials Res. Soc.*, Pittsburgh, (1995), 87.
22. Baker, R.T.K., *Carbon Fibers, Filaments and Composites NATO ASI Series*, Kluwer, Dordrecht, (1990), 405.
23. Serp, P., Corrias, M., Kalck, P., *Appl. Catal. A-Gen.*, (2003), 253, 337.
24. Serp, P., Kalck, P., Feurer, R., *Chem. Rev.*, (2002), 102, 3085.
25. Ros, T.G., Ph.D. thesis, Utrecht University, Utrecht, the Netherlands, (2002).
26. Teunissen, W., Hoogenraad, M.S., in "heteroGeneUS Catalysis, Preparation, Characterization and application" (De Jong, K.P., Van Dillen, A.J., Eds.), *Publicard*, Utrecht, (1998), 137.
27. Iijima, S., *Nature*, (1991), 351, 56.
28. Schlogl, R., Che, M., Clause, O., Marchilly, C., in "Preparation of Solid Catalysts", *Wiley-VCH*, Weinheim, (1999), Chapter 3 and 4.
29. Rodriguez, N.M., *J. Mater. Res.*, (1993), 3, 3233.
30. Baker, R.T.K., *Carbon*, (1989), 27, 315.
31. Rodriguez, N.M., Kim, M.-S., Baker, R.T.K., *J. Phys. Chem.*, (1994), 93, 13108.
32. Geus, J.W., Van Dillen, A.J., Hoogenraad, M.S., *Mat. Res. Soc. Symp. Proc.*, (1995), 363, 87.
33. Trimm, D.L., *Catal. Rev.-Sci. Eng.*, (1977), 16, 155.
34. Toebes, M.L., Bitter, J.H., Van Dillen, A.J., De Jong, K.P., *Catal. Today*, (2002), 76, 33.
35. Rodriguez-Reinoso, F., *Carbon*, (1998), 36, 159.



Catalytic growth of macroscopic carbon nanofiber bodies with high bulk density and high mechanical strength

Abstract

Carbon nanofibers (CNF) are non-microporous graphitic materials with a high surface area (100-200 m²/g), high purity and tunable surface chemistry. Therefore the material has a high potential for use as catalyst support. However, in some instances it is claimed that the low density and low mechanical strength of the macroscopic particles hamper their application. In this study we show that the bulk density and mechanical strength of CNF bodies can be tuned to values comparable to that of commercial fluid-bed and

fixed-bed catalysts. The carbon nanofibers used in this study were prepared by the chemical decomposition of synthesis gas (CO/H₂) over Ni/SiO₂ catalysts. The resulting CNF formed bodies (1.2 μm) which were replicates of the Ni/SiO₂ bodies (0.5 μm) from which they were grown. The bulk density of carbon nanofibers bodies crucially depended on the metal loading in the Ni/SiO₂ growth catalyst. Over 5 wt% Ni/SiO₂ low density bodies (0.4 g/ml) are obtained while 20 wt% Ni/SiO₂ leads to bulk densities up to 0.9 g/ml with a bulk crushing strength of 1.2 MPa. We could relate the difference in properties of the fiber bodies to the difference in extent of sintering of the Ni particles in the two growth catalysts. In the 20 wt% catalyst the Ni particles are in close proximity to each other resulting in a more significant sintering of the Ni particles during growth. This results in larger diameter CNF (~22 nm) for the highly loaded catalyst since the fiber diameter is determined by the Ni particles size. These thicker fibers are known to grow more irregularly in space, resulting in a higher entanglement of the fibers and a concomitant higher density and strength as compared to the thinner fibers (~12 nm) grown from 5 wt% Ni.

Introduction

Carbon fibers (CNF) are graphite-like materials, which hold great potential as catalyst support [1-23]. However, at a number of occasions it is claimed that these materials are obtained as “fluffy materials” i.e., having a low bulk density [2,24-26] and a low mechanical strength [2]. This would not allow the economic use in a reactor since the mass of catalyst per reactor volume is too low. In addition, due to the mechanical weakness of those materials, application in large fixed-bed reactors, fluidized-bed or slurry-phase reactors is not viable. Therefore synthesis routes to CNF bodies with high bulk densities and high strength are much desired.

Different methods to prepare CNF are described in literature, a.o., arc discharge [27-30], decomposition of organometallic compounds [31-33] or chemical vapor deposition [34-37] of carbon containing gases over metal catalysts, i.e. catalytic growth [38-43]. The latter option is preferred for large-scale production of CNF [44,45]. Essential in the growth of CNF is the decomposition of the carbon source on the surface of the metal particles. The thus formed carbon atoms migrate through/over the metal to assemble into CNF [1,2,46,47]. CNF growth critically depends on a number of factors such as temperature, nature of the catalyst and source of carbon [1,2,41,48-57].

It is claimed that the CNF can form 3-dimensional networks of interwoven fibers resulting in bodies of micrometer size which are replicates of the original shape of the catalyst particles from which they were grown [2,58-61]. Typically

the formed CNF bodies increase with a factor 3 in diameter compared to the size of the catalyst particles [58]. Thus when a fine powder is used as starting material the resulting CNF bodies also consist of small bodies. This can explain why some authors obtain CNF as powder while others obtain macroscopically shaped CNF bodies [58-61].

Literature revealed that when CNF are grown with a low rate irregularly shaped fibers can be formed which strongly entangle with each other [1,2,46]. This potentially can lead to highly dense materials, which can be mechanically strong as well. The final density of the material depends crucially on the way in which the CNF are grown. For example Hoogenraad et al [2] obtained CNF with a bulk density of 0.35 g/ml grown from 20 wt% Ni/Al₂O₃ using methane as the carbon source while Reshетенko [25] obtained a bulk density of 0.76 g/ml over a highly loaded 90 wt% Ni/Al₂O₃ catalyst. Besides the different nickel loading, Reshетенko used a vibro-fluid-bed reactor and pure methane as carbon source at 773 K while Hoogenraad et al used a fixed-bed reactor with diluted methane gasflows at 823 K.

In the current contribution we investigate the role of the growth catalysts, in particular the metal loading, on the bulk density and strength of the prepared CNF bodies.

We chose Ni/SiO₂ as the growth catalyst because SiO₂ has significant advantages over the use of Al₂O₃ when pure CNF are desired. SiO₂ is conveniently removed by a treatment of the prepared materials by a solution of KOH [46]. In case of Al₂O₃ acid extraction is needed while full removal of the support is cumbersome [47]. For the silica-based catalyst in a separate step the exposed growth catalyst (Ni) is removed by a treatment in concentrated HCl [15,46].

General agreement exists on the fact that the diameter of the CNF is always similar to that of the metal particle from which it is grown [2,58-61]. In earlier studies it is found that the size of Ni particles in the CNF can be significantly larger than those in the fresh growth catalysts [1,2,42,58]. Clearly a sintering step is involved during the CNF growth. This sintering only occurred during CNF growth since in inert or hydrogen atmospheres at temperatures even higher than the CNF growth temperature sintering did not occur [62,63]. Since sintering appears to be an important issue in CNF preparation we choose to use for our study two Ni/SiO₂ catalysts having similar Ni particles sizes but different metal loadings (5 and 20 wt%) i.e., different sintering rates can be expected. The influence of the metal loading will be shown to have a crucial influence on the properties (yield and density) of the CNF bodies.

Experimental

Preparation of growth catalyst

5 or 20 wt% Ni/SiO₂ catalysts were prepared by deposition precipitation as described by Van Dillen et al. [65] using 10.0 gram silica (Degussa, Aerosil 200, powder), nickel nitrate (Acros) and urea (Acros). After washing, filtration and drying at 393 K the catalyst precursor was calcined in static air at 873 K.

CNF preparation

Prior to the carbon nanofiber growth 0.4 gram of the nickel-silica growth catalyst, sieve fraction 425 – 850 μm, was placed in a quartz upflow fixed-bed reactor (internal diameter 25 mm) and reduced in situ for 2 hours in a flow of a mixture of H₂ (80 ml/min) and N₂ (320 ml/min) at 1 bar and at 973 K (heating rate 5 K/min). Next, the fibers were grown at 823 K in a mixture of CO (120 ml/min), H₂ (42 ml/min) and N₂ (238 ml/min) for 1, 2, 4, 6 or 20 hours. The product (including the growth catalyst) was refluxed for 2 h in 200 ml of an aqueous 1 M KOH solution to remove the silica support. Next, after filtering and thoroughly washing with de-ionised water, the fibers were refluxed in concentrated HCl, to remove exposed nickel followed by washing and drying.

Characterization

XRD patterns were recorded at room temperature with an Enraf Nonius PDF 120 powder diffractometer system equipped with a position-sensitive detector with a 2θ range of 120° using Co Kα₁ (λ = 1.78897 Å) radiation. Average particle sizes were calculated using the Debye-Scherrer equation.

Nitrogen physisorption was carried out at 77 K using a Micromeritics Tristar 3000 V 6.01. Prior to the physisorption measurement the samples were dried in a He flow at 573 K. For the analysis of the average pore diameter the BJH method was applied to the desorption isotherm.

Scanning electron microscopy (SEM) was carried out using a Philips XL30 FEG apparatus. The samples were placed on a carbon coated sample holder. In case of the CNF bodies, both intact and cleaved CNF bodies were investigated. The intact bodies were used to scan the outside of the skeins. The cleaved bodies were analyzed both on the outside as well as on the cleaved facet of the body.

TEM samples were prepared by suspending the fibers after grinding in ethanol under ultrasonic vibration. Some drops of the thus produced suspension were brought onto a holey carbon film on a copper grid. The grid was transferred to a FEG-Technai-20 TEM apparatus operated at 200 KeV.

Bulk density of carbon nanofiber bodies

The bulk density of grown carbon nanofibers was determined by measuring the mass of a fixed volume. A fixed volume, i.e., a glass cylinder, was filled without vibration, with the CNF bodies in accordance to the American Standard Test Methods (ASTM D1895-96 B).

Bulk Crushing strength

About 17 ml of carbon nanofibers bodies with a body size larger than 425 μm were packed in a steel container. Pressures from 0.2 to 3.1 MPa were applied on the stacked CNF bodies via a steel dye. With increasing pressure the CNF bodies break and as a result fines (bodies < 425 μm) were formed. The cumulatively weight of the fines was determined as function of the applied pressure. The bulk crushing strength (BCS) is defined as the pressure at which cumulatively 0.5 wt% fines are formed.

Results

Some of the physico-chemical properties of the Ni/SiO₂ growth catalysts have been compiled in Table 1. Although the Ni-particle size of Ni-5 and Ni-20 are similar, the density of particles is much higher for Ni-20, see Figure 1. The Ni particle size distribution of Ni-20 seems to be somewhat broadened as well. Low magnification SEM images have been collected to report the bodies shapes and sizes. Figure 2A and 2B show the SEM images of the original Ni/SiO₂ growth catalyst Ni-5 and Ni-20. Figure 2C-F gives a macroscopic overview of the CNF bodies formed after 1 and 20 hours over Ni-5 and Ni-20 resulting in CNF-5-x or CNF-20-x with x representing the growth time in hours. It can be noted that irrespective of the applied growth conditions the CNF skeins have similar shapes as the original growth catalysts. However, after 1 hour the bodies are smaller than the original Ni/SiO₂ bodies while after 20 hours they are larger.

Table 1: Some physico-chemical properties of Ni/SiO₂ growth catalysts reduced at 973 K for 2 hours in H₂.

	Nominal Ni loading [wt%]	Ni d _p [nm]		S _{BET} [m ² /g]	PV [ml/g]
		XRD	TEM		
Ni-5	5	4	4	181	1.26
Ni-20	20	5	5	217	0.85

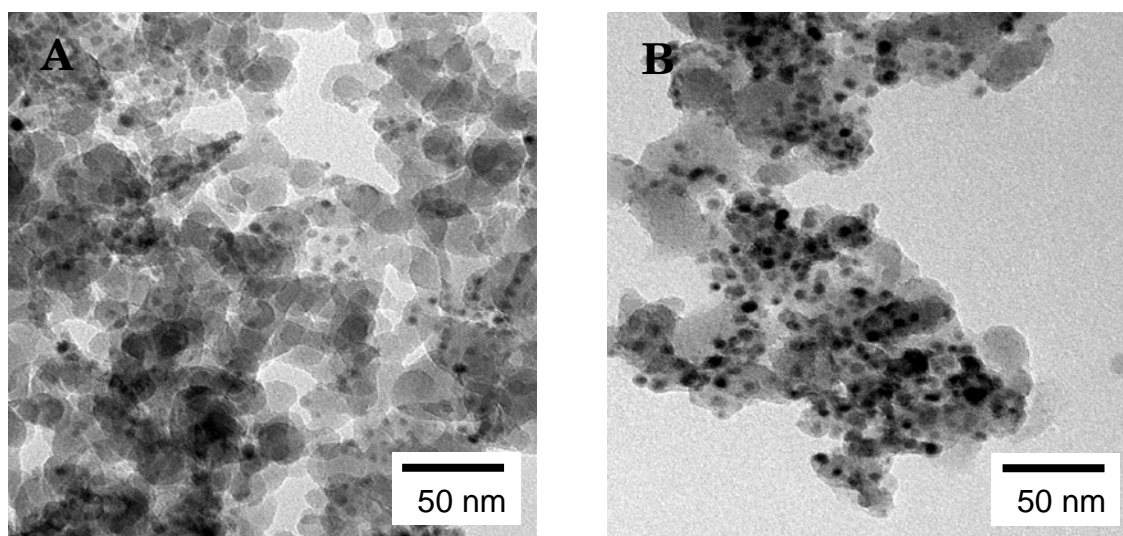


Figure 1: TEM images of growth catalysts after reduction at 973 K. (A) 5 wt% Ni/SiO₂ and (B) 20 wt% Ni/SiO₂.

On a mesoscopic scale significant differences can be observed among the different samples. In Figure 3 SEM micrographs of CNF-5-20 and CNF-20-20 are shown. The top part of Figure 3 (A-B) shows the outer surface of the CNF bodies while the lower part (C-D) displays the inside. The diameter distributions of the fibers on the surface the inside of the bodies after 1 and 20 hour of growth obtained from SEM images have been compiled in Figure 4. After 1 hour of growth clearly from Ni-5 smaller diameter (8-16 nm) CNF were grown compared to those from Ni-20 (16-30 nm).

The fiber diameter distribution of CNF-5-1 and CNF-20-1 (Figure 4) both shift to larger diameters with longer growth times. SEM images show that for CNF-5-20 well defined individual CNF can be observed (Figure 3), while for CNF-20-20 a densely packed structure is formed inside the CNF bodies. Some textural and structural properties of the prepared samples are given in Table 2. In line with the decrease in BET surface area the observed diameter of the CNF increases. From the BET surface area and assuming a carbon density of 2.25 g/cm³ and closed solid fibers a diameter for the fibers can be calculated (Table 2; d_{calc}). Clearly the calculated fiber diameter based on BET is smaller than those obtained from SEM although the trends in diameter variation with time are similar. Recently we have reported that CNF may contain internal cylindrical pores of about 5-10 nm which explains the higher diameter values from TEM compared to those from the specific surface areas [66].

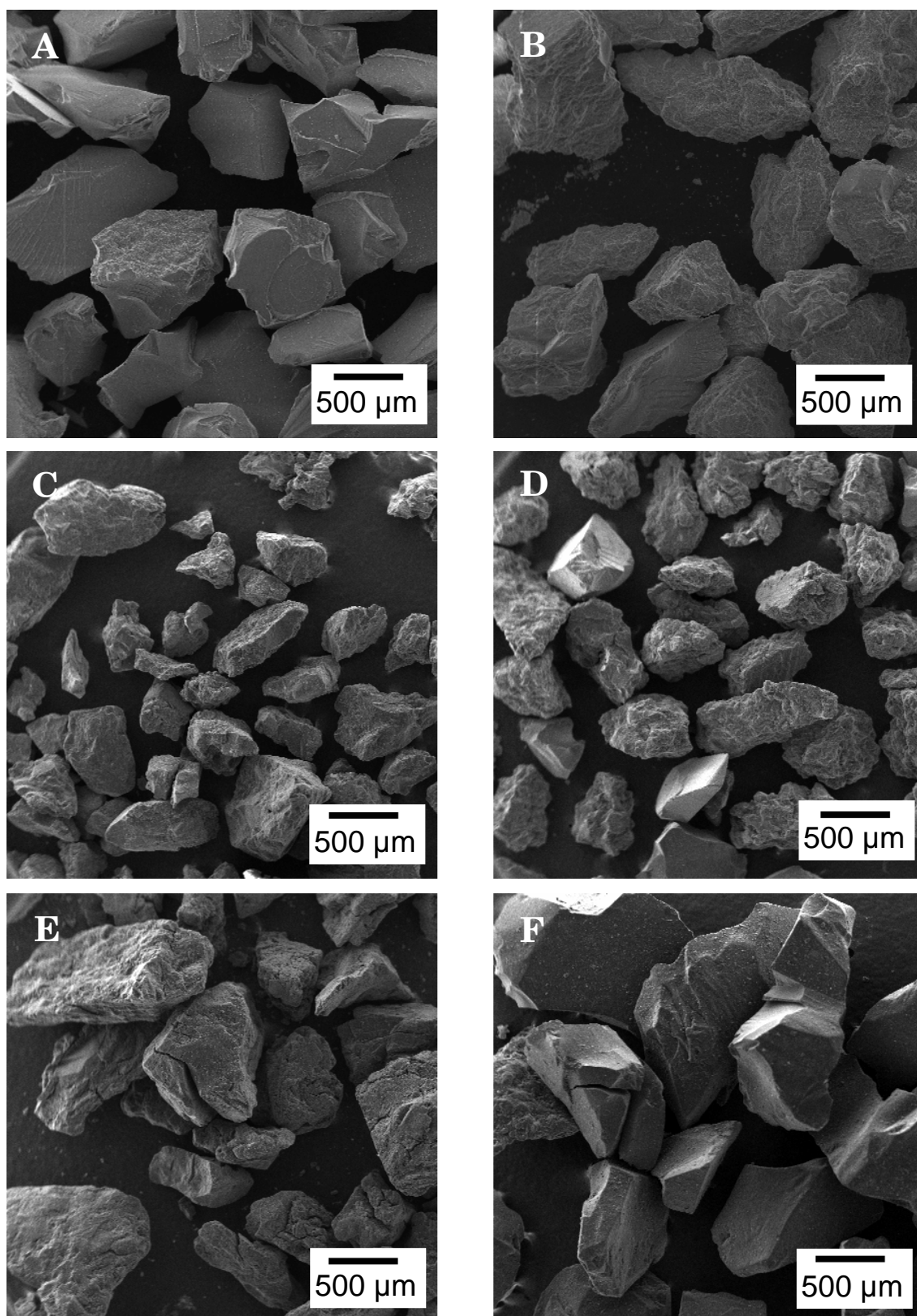


Figure 2: Low magnification SEM images of growth catalyst after reduction 973 K and grown CNF bodies. (A) 5 wt% Ni/SiO₂; (B) 20 wt% Ni/SiO₂; (C) CNF bodies CNF-5-1; (D) CNF bodies CNF-20-1; (E) CNF bodies CNF-5-20; (F) CNF bodies CNF-20-20.

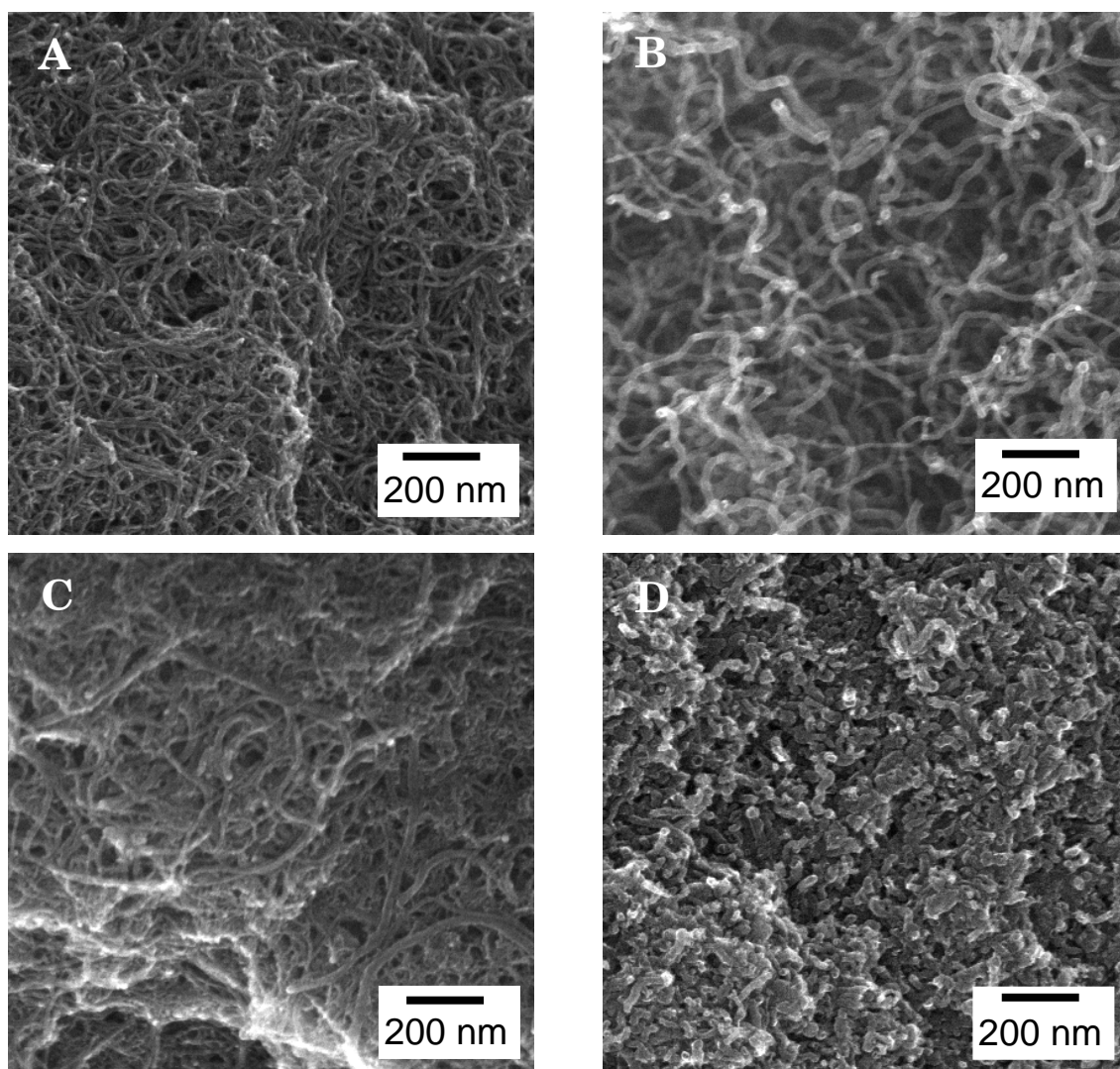


Figure 3: High magnification SEM images of carbon nanofibers grown for 20 hours using Ni-5 or Ni-20 growth catalyst. (A) Outside CNF-5-20; (B) Outside of CNF-20-20; (C) Inside CNF-5-20; (D) Inside of the CNF-20-20.

Figure 5 shows the yield of CNF per gram nickel as function of the growth time and as function of the growth catalyst. Ni-5 shows a linear increase in CNF yield as function of time. On the other hand, Ni-20 initially grows CNF with a higher rate but the rate declines with time.

The bulk density of the CNF bodies as function of growth catalyst and growth time is displayed in Figure 6. For CNF-5 an initial decrease in the bulk density was observed after which it remained constant around 0.4 g/ml. For CNF-20 an initial sharp increase of the bulk density was found from 0.5 after 1 hour CNF growth to 0.8 g/ml after 6 hours of growth. Finally after 20 hours of growth skeins with a bulk density of 0.9 g/ml were obtained.

Table 2: Some physico-chemical properties of the CNF bodies.

	Growth Catalyst	Growth time [h]	S_{BET} [m²/g]	PV [ml/g]	d_{obs} [nm] (TEM)	d_{calc} [nm] (BET)
CNF-5-1	Ni-5	1	232	0.69	10	8
CNF-5-4	Ni-5	4	167	0.85		11
CNF-5-6	Ni-5	6	208	0.84		9
CNF-5-20	Ni-5	20	197	0.73	12	9
CNF-20-1	Ni-20	1	165	0.68	20	11
CNF-20-4	Ni-20	4	160	0.32		11
CNF-20-6	Ni-20	6	151	0.25		12
CNF-20-20	Ni-20	20	130	0.19	24	14

Silica from growth catalysts was removed by refluxing CNF bodies in 1M KOH for 2 hours. BET and pore volume are based on nitrogen physisorption.

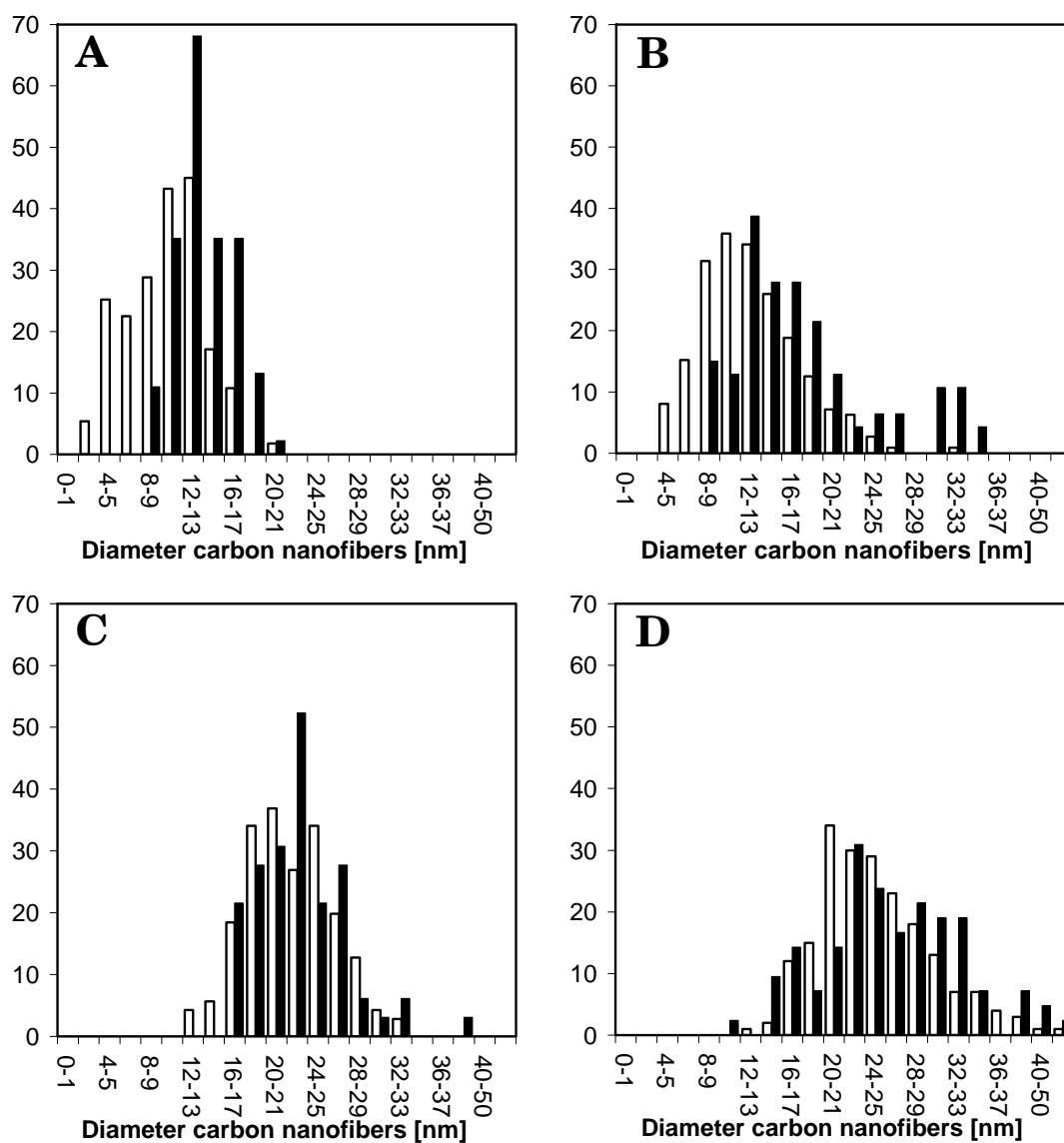


Figure 4: Carbon nanofiber diameter distribution inside (black bars) and at outside (open bars) of the CNF body, (A) CNF-5-1; (B) CNF-5-20; (C) CNF-20-1; (D) CNF-20-20.

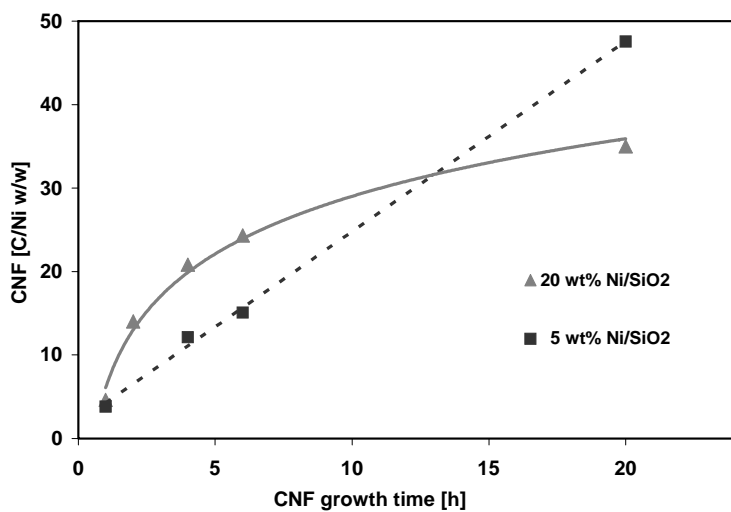


Figure 5: CNF yield (gram carbon per gram nickel) as function of time and metal loading in the growth catalyst.

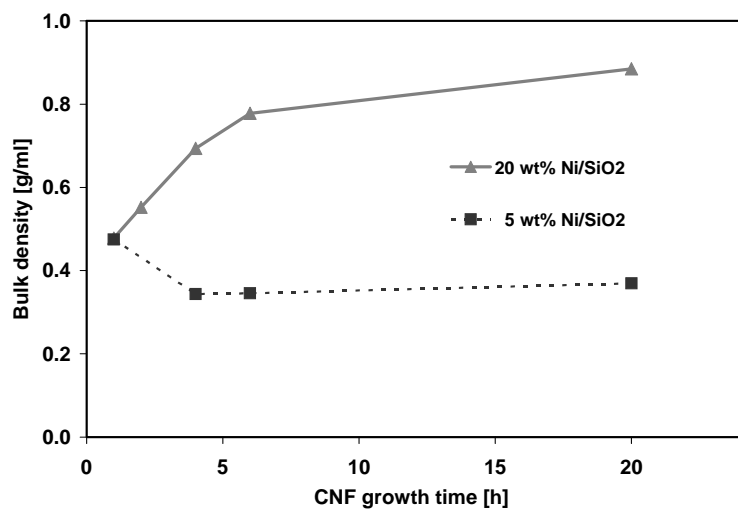


Figure 6: Bulk density of CNF as function of the metal loading in the growth catalyst and growth time.

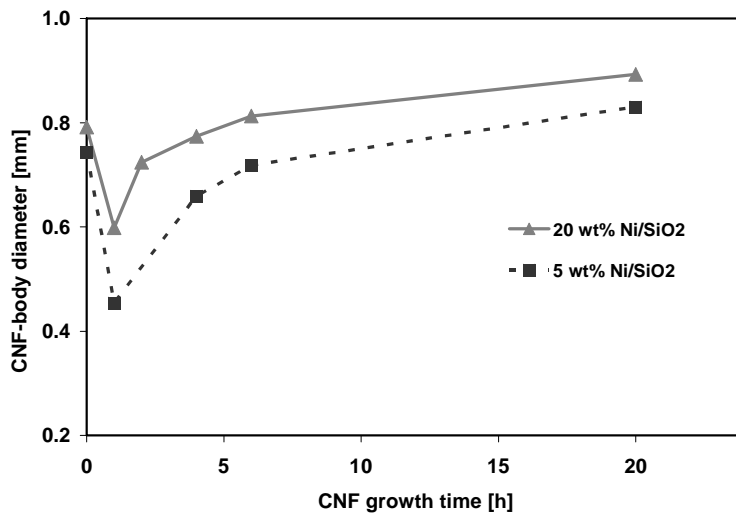


Figure 7: CNF-body size as function of growth time. At 0 hours the average diameter of original Ni/SiO₂ particles are shown for Ni-5 and Ni-20 catalysts.

As shown in Figure 5 the mass of CNF produced increases with time. On the other hand the bulk density increases for CNF prepared with Ni-20 but remains constant with time over Ni-5 (Figure 6). Therefore it is interesting to know what the influence of growth time and nickel catalyst loading is on the size of the CNF bodies prepared. Figure 7 shows the average body size as function of time. For CNF prepared over both catalysts an initial decrease in the body size is observed while after 1 hour of growth the size increases again. The latter being with a higher rate over Ni-5 compared to Ni-20.

The high bulk density of the Ni-20-20 material (0.9 g/ml) is comparable to or above that of commercial catalysts [68]. In addition the bulk crushing strength of the CNF-20-20 bodies was found to be 1.25 MPa (Figure 8) which make them suitable for fixed-bed applications [58].

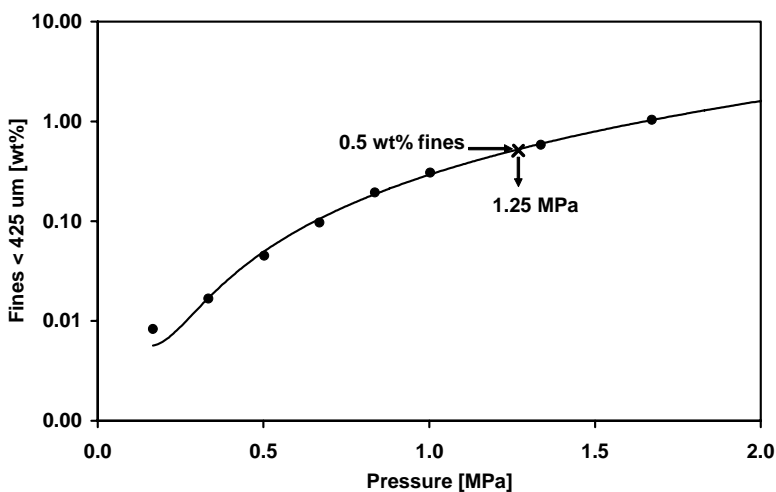


Figure 8: Cumulative amount of fines measured as function of pressure during bulk crushing strength analyses of the Ni-20-20 CNF bodies.

Discussion

Figures 1 and 2 give an overview of the used Ni/SiO₂ catalyst. The physico-chemical properties of these materials are summarized in Table 1. Close inspection and analysis of the micrographs of the CNF (Figure 3) reveals that all fibers in the bodies, irrespective of the growth conditions, have a larger diameter (8-40 nm, Figure 4) than the Ni particles from which they were grown (~5 nm; Table 1 and Figure 1). At many occasions it has been shown that the diameter of the grown CNF closely matches that of the Ni particles at the top of the fibers [2,34,46,58,66,67] from which the fibers were grown. Thus it must be concluded that in some stage the initial small Ni particles (~5 nm) have sintered to larger particles (8-40 nm).

Most likely, sintering occurs prior to the start of the CNF growth. This is also supported by the fact that small metal particles (<5 nm) retard the formation of graphene sheets since their surface is strongly curved [2,46]. In earlier studies [46,64] we showed that the Ni particles in Ni/SiO₂ do not sinter significantly in H₂ atmosphere. Therefore the carbon containing gas is a prerequisite for sintering. Since in Ni-20 the concentration of Ni particles is higher compared to that in Ni-5 it can be expected that a) the sintering is more significant over Ni-20 due to the closer proximity of the Ni particles and b) the CNF growth rate is higher over Ni-20 due to the higher amount of active metal which is in line with what is observed (Figure 5). This is in agreement with the thicker fibers, which are formed over Ni-20 (Figure 4). From Ni-5 with an initial particle size of 4 nm (Table 1) CNF with an average diameter of 12 nm were grown (Figure 3 and 4) while from Ni-20 with an initial Ni particle size of 5 nm (Table 1) CNF with an average diameter of 22 nm were grown (Figure 4). From this it can be estimated that roughly 6 times more Ni is involved in the growth of a single fiber from Ni-20 as compared to Ni-5 which is not too remote from the difference in metal loading in both catalysts.

The thicker fibers e.g., CNF-20-20, grow in bodies with a higher bulk density as compared to the thin fibers which grow in less dense bodies (Figure 6). This can be explained by the different growth mechanism of large and small diameter fibers. Large diameter fibers grow via the so-called rice-shell mechanism resulting in irregular shaped fibers [1,2,46]. Here the growth of CNF is not a continuous process but is periodical [2,58,69]. The metal particle is converted to metal carbide while a significant fraction of the metal surface is encapsulated by carbon. When a certain carbide concentration has been reached the encapsulating shell bursts and the Ni whole particle becomes available again for growth. The driving force for the excretion of the fiber is a lowering of the density of the metal/carbide phase via demixing of the metal and the carbide. In this “start-stop-start-stop” mechanism every start of growth can be in a

different direction resulting in curved fibers which strongly entangle. The thin CNF grow via a continuous carbon dissolution-excretion model. In the latter mechanism the rate of carbide formation in the metal particle is balanced by the formation of the carbon fibers, which results in the continuous growth rate of CNF, which are more straight (Figure 3) [2,69].

After having established the nature of the CNF growth processes on a mesoscopic scale it turns out that the growth conditions also have an influence on the size of the formed bodies (Figure 2 and 7) i.e., on a macroscopic scale. Figure 7 shows clearly that irrespective of the growth catalyst first a decrease in body size is observed as function of the amount of CNF formed. This is the result of fragmentation of the initial Ni/SiO₂ bodies into smaller bodies. Because the bulk density of CNF-5 does not increase with time (Figure 6) while the yield of CNF does (Figure 5) it must be concluded that this material grows in a voluminous way in which the increase in CNF yield results in a continuous expansion of the bodies resulting in a constant bulk density. This does not hold for Ni-20, since after the initial decrease of the CNF body size it increases, however, with a lower rate as compared to Ni-5 as inferred from Figure 5 by the lower slope between 4-20 g C/g Ni. Thus the newly formed CNF in CNF-20 grow in the empty spaces inside the bodies resulting in a lower expansion rate of the bodies, thus, resulting in a higher bulk density as compared to CNF-5. The higher bulk density of CNF-20-x compared to that of CNF-5-x is in line with the mesoscopic growth mechanism discussed above. Since thicker fibers, i.e., those in CNF-20-x grown in an irregular way, are bent resulting in a high entanglement resulting in a high bulk density. The straight thinner fibers in CNF-5-x on the other hand grow faster and do not entangle very well resulting in a low bulk density.

Since we were never able to detect large patches of SiO₂ by TEM/EDX, before SiO₂ removal, it is concluded that the SiO₂ is completely fragmented during the growth process. This is schematically shown in Figure 9. The initially formed CNF break up the weak Ni/SiO₂ body in smaller fragments. Next the fibers on the inside start to grow in all directions thus continuously expanding the much stronger CNF body resulting in replicates of fragments of the original SiO₂ body [58-61]. The properties of the CNF-20-20 bodies are such that they are suitable for commercial application at least in fixed-bed reactors [68]. Different ways of metal deposition on these materials are put forward in literature [e.g.,13,16,22,23,68,71] resulting in catalyst which can be among the most active one for e.g. cinnamaldehyde hydrogenation [16].

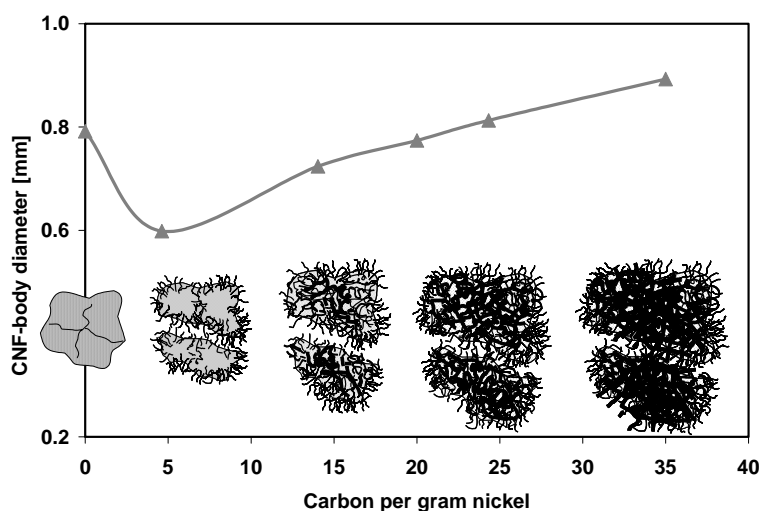


Figure 9: Schematic representation of macroscopic bodies consisting of dense CNF growth from left to right: Ni/SiO₂ body with cracks – growing CNF fragmentize the body – start of large diameter growth CNF in interior – further expansion of CNF body.

Conclusions

The diameter of carbon nanofibers (CNF) formed over Ni/SiO₂ was dependent on the metal loading in the growth catalyst. When starting with identical nickel particle sizes (5 nm) a highly loaded Ni/SiO₂ catalyst (20 wt%) resulted in fibers with a average diameter of ~22 nm. These bodies had a high bulk density of 0.9 g/ml and high mechanical strength making these materials suitable for applications in a fixed-bed reactor. Lower loaded Ni/SiO₂ (5 wt%) led to straight ~12 nm fibers throughout the CNF body. The formation of straight fibers relates to the lower density of the formed CNF bodies, which are replicas of the Ni/SiO₂ growth catalyst. The thicker fibers formed over 20 wt% Ni/SiO₂ were more entangled due to their bent shapes which resulted in high bulk density and high mechanical strength of the CNF bodies.

Acknowledgments

The authors acknowledge J.W. Geus for helpful discussions about high density carbon nanofiber bodies, performing the TEM and SEM measurements and the financial support of STW (grant UPC 5487).

References

1. De Jong, K.P., Geus, J.W., *Catal. Rev.-Sci. Eng.*, (2000), 42, 481.
2. Hoogenraad, M.S., Ph.D. thesis, Utrecht University, Utrecht, The Netherlands, (1995).
3. Serp, P., Corrias, M., Kalck, P., *Appl. Catal. A-Gen.*, (2003), 253, 337.
4. Hoogenraad, M.S., Onwezen, M.F., Van Dillen, A.J., Geus, J.W., *Stud. Surf. Sci. Catal.*, (1995), 101, 1331.
5. Geus, J.W., Hoogenraad, M.S., Van Dillen, A.J., in "Synthesis and Properties of Advanced Catalytic Materials" (Iglesia, E., Lednor, P.W., Nagaki, D.A., Thompson, L.T., Eds.), *Materials Res. Soc.*, Pittsburgh, (1995), 87.
6. Hoogenraad, M.S., Van Leeuwarden, R.A.G.M.M., Van Breda Vriesman, G.J.B., Broersma, A., Van Dillen, A.J., Geus, J.W., in "Preparation of Catalysts VI" (Poncelet, G., Eds.), Elsevier, Amsterdam, (1995), 263.
7. Mojet, B.L., Hoogenraad, M.S., Van Dillen, A.J., Geus, J.W., Koningsberger, D.C., *J. Chem. Soc. Faraday Trans.*, (1997), 93, 4371.
8. Rodriguez, N.M., Kim, M.-S., Baker, R.T.K., *J. Phys. Chem.*, (1994), 98, 13108.
9. Chambers, A., Nemes, T., Rodriguez, N.M., Baker, R.T.K., *J. Phys. Chem. B.*, (1998), 102, 2251.
10. Park, C., Baker, R.T.K., *J. Phys. Chem. B.*, (1998), 102, 5168.
11. Park, C., Baker, R.T.K., *J. Phys. Chem. B.*, (1999), 103, 2453.
12. Salman, F., Park, C., Baker, R.T.K., *Catal. Today*, (1999), 53, 385.
13. Pham-Huu, C., Keller, N., Charbonniere, L.J., Ziessel, R., Ledoux, M.J., *Chem. Comm.*, (2000), 1871.
14. Planeix, J.M., Coustel, N., Coq, B., Brotons, V., Kumbhar, P.S., Dutartre, R., Geneste, P., Bernier, P., Ajayan, P.M., *J. Am. Chem. Soc.*, (1994), 116, 7935.
15. Ang, L.-M., Andy Hor, T.S., Xu, G.-Q., Tung, C.-H., Zhao, S., Wang, J.L.S., *Chem. Mater.*, (1999), 11, 2115.
16. Toebes, M.L., Zhang, Y., Hajek, J., Nijhuis, T.A., Bitter, J.H., Van Dillen, A.J., Murzin, D.Y., Koningsberger, D.C., De Jong, K.P., *J. Catal.*, (2004), 226, 215.
17. Jarrah, N., Van Ommen, J.G., Lefferts, L. *Catal. Today*, (2003), 79, 29.
18. Toebes, M.L., Prinsloo, F.F., Bitter, J.H., Van Dillen, A.J., De Jong, K.P., *J. Catal.*, (2003), 214, 78.

19. Pham-Huu, C., Keller, N., Ehret, G., Charbonniere, L.J., Ziessel, R., Ledoux, M.J. *J. Mol. Catal. A-Chem.*, (2001), 170, 155.
20. Chambers, A., Nemes, T., Rodriguez, N.M., Baker, R.T.K., *J. Phys. Chem. B.*, (1998), 102, 2251.
21. Salman, F., Park, C., Baker, R.T.K., *Catal. Today*, (1999), 53, 385.
22. Ros, T.G., Keller, D.E., Van Dillen, A.J., Geus, J.W., Koningsberger, D.C., *J. Catal.*, (2002), 211, 85.
23. Reshetenko, T.V., Avdeeva, L.B., Ismagilov, Z.R., Chuvilin, A.L., *Carbon*, (2004), 42, 143.
24. Qiu, J., Li, Y., Wang, Y., *Carbon*, (2004), 42, 2359.
25. Reshetenko, T.V., Avdeeva, L.B., Ismagilov, Z.R., Pushkarev, V.V., Cherepanova, S.V., Chuvilin, A.L. *Likholobov, V.A.*, *Carbon*, (2003), 41, 1605.
26. Wang, Y., Wei, F., Gu, G., Yu, H., *Physica. B.*, (2002), 323, 327.
27. Li, L., Li, F., Liu, C., Cheng, H.-M., *Carbon*, (2005), 43, 623.
28. Huang, H., Kajiura, H., Murakami, Y., Ata, M., *Carbon*, (2003), 41, 615.
29. Seraphin, S., Wang, S., Zhou, D., Jiao, J., *Chem. Phys. Lett.*, (1994), 228, 506.
30. Kajiura, H., Huang, H., Tsutsui, S., Murakami, Y., Miyakoshi, M., *Carbon*, (2002), 40, 2423.
31. Tibbetts, G.G., *Carbon*, (1989), 27, 745.
32. Schnitzler, M.C., Oliveira, M.M., Ugarte, D., Zarbin, A.J.G., *Chem. Phys. Lett.*, (2003), 381, 541.
33. Satishkumar, B.C., Govindaraj, A., Sen, R., Rao, C.N.R., *Chem. Phys. Lett.*, (1998), 293, 47.
34. Zheng, G.-B., Kouda, K., Sano, H., Uchiyama, Y., Shi, Y.-F., Quan, H.-J., *Carbon*, (2004), 42, 635.
35. Yoon, Y.J., Baik, H.K., *Diam. Relat. Mater.*, (2001), 10, 1214.
36. Serp, P., Madroño, A., Figueiredo, J. L., *Fuel*, (1999), 78, 837.
37. Ci, L., Li, Y., Wei, B., Liang, J., Xu, C., Wu, D., *Carbon*, (2000), 38, 1933.
38. Trimm, D.L., *Catal. Rev.-Sci. Eng.*, (1977), 16.
39. Rostrup-Nielsen, J.R., Trimm, D.L., *J. Catal.*, (1977), 48, 155.
40. Bartholomew, C.H., *Catal. Rev.-Sci. Eng.*, (1982), 24, 67.
41. Figueiredo, J.L., *Erdol Kohle-Erdgas-Petrochem.*, (1989), 42, 294.
42. Rodriguez, N.M., *J. Mater. Res.*, (1993), 8, 3233.
43. Baker, R.T.K., *Carbon Fibers, Filaments and Composites NATO ASI Series*, Kluwer, Dordrecht, (1990), 405.
44. Hammel, E., Tang, X., Trampert, M., Schmitt, T., Mauthner, K., Eder, A., Pötschke, P., *Carbon*, (2004), 42, 1153.

45. Wang, Y., Wei, F., Luo, G., Yu, H., Gu, G., *Chem. Phys. Lett.*, (2002), 364, 568.
46. Toebes, M.L., Bitter, J.H., Van Dillen A.J., De Jong, K.P., *Catal. Today*, (2002), 76, 33.
47. Ros, T.G., Ph.D. thesis, Utrecht University, Utrecht, The Netherlands, (2002).
48. Rodriquez, N.M., Chambers, A., Baker, R.T.K., *Langmuir*, (1995), 11, 3862.
49. Colomer, J.-F., Piedigrosso, P., Willems, I., Cournet, C., Bernier, P., Van Tendeloo, G., Fonseca, A., Nagy, J.B., *J. Chem. Soc. Faraday Trans.*, (1998), 94, 3753.
50. Chen, P., Zhang, H.-B., Lin, G.-D., Hong, Q., Tsai, K.R., *Carbon*, (1997), 35, 1495.
51. Boellaard, E., De Bokx, P.K., Kock, A.J.H.M., Geus, J.W., *J. Catal.*, (1985), 96, 481.
52. Baker, R.T.K., Kim, M.S., Chambers, A., Park, C., Rodriquez, N.M., *Stud. Surf. Sci. Catal.*, (1997), 111, 99.
53. Alstrup, I., *J. Catal.*, (1988), 109, 241.
54. Audier, M., Oberlin, A., Coulon, M., *J. Crystal Growth*, (1981), 55, 549.
55. Schouten, F.C., Kaleveld, E.W., Bootsma, G.A., *Surf. Sci.*, (1977), 63, 1.
56. Schouten, F.C., Gijzeman, O.L.J., Bootsma, G.A., *Surf. Sci.*, (1979), 87, 460.
57. Kim, M.-S., Rodriquez, N.M., Baker, R.T.K., *Mat. Res. Soc. Symp. Proc.*, (1995), 368, 99.
58. Teunissen, W., Ph.D. thesis, Utrecht University, Utrecht, The Netherlands, (2000).
59. Kuvshinov, G.G., Mogilnykh, Y.I., Kuvshinov, D.G., Yermakov D.Y., Yermakova, M.A., Salanov, A.N., Rudina, N.A., *Carbon*, (1999), 37, 1239.
60. Ledoux, M.-J., Pham-Huu, C., *Catal. Today*, (2005), article in press.
61. Vieira, R., Ledoux, M.-J., Pham-Huu, C., *Appl. Catal. A*, (2004), 274, 1.
62. Hadjiivanov, K., Mihaylov, M., Klissurski, D., Stefanov, P., Abadjieva, N., Vassileva, E., Mintchev, L., *J. Catal.*, (1999), 185, 314.
63. Pina, G., Louis, C., Keane, M.A., *Phys. Chem. Chem. Phys.*, (2003), 5, 1924.
64. Van Stiphout, P.C.M., Stobbe, D.E., V.D. Scheur, F.T., Geus, J.W., *Appl. Catal.*, (1988), 40, 219.
65. Van Dillen, A.J., Geus, J.W., Hermans, L.A.M., Van der Meijden, J.J., *Proc. Int. Congr. Catal.*, (1977), 2, 677.
66. Winter, F., Bezemer, G.L., Van der Spek, C., Meeldijk, J.D., Van Dillen, A.J., Geus, J.W., De Jong, K.P., *Carbon*, (2005), 43, 327.

67. Anderson, P.E., Rodriguez, N.M., Chem. Mater., (2000), 12, 823.
68. International patent number 04076211.4, Application date: 2004.
69. Teunissen, W., Hoogenraad, M.S., in “heteroGENeUS Catalysis, Preparation, Characterization and application” (De Jong, K.P., Van Dillen, A.J., Eds.), Publicard, Utrecht, (1998).
70. Bitter, J.H., Van der Lee, M.K., Slotboom, A.G.T., Van Dillen, A.J., De Jong, K.P. Catal. Lett., (2003), 89, 139.
71. Toebes, M.L., Van der Lee, M.K., Tang, L.M., Huis in 't Veld, M.H., Bitter, J.H., Van Dillen, A.J., De Jong, K.P., J. Phys. Chem. B., (2004), 108, 11611.

3

Synthesis of well dispersed, highly loaded nickel on carbon nanofibers – Preliminary studies

Abstract

In order to prepare nickel-on-carbon nanofiber catalysts, both incipient wetness impregnation and deposition precipitation techniques have been applied. To create a well dispersed metallic nickel phase on the fishbone type carbon nanofibers some prerequisites had to be fulfilled. The solvent containing the metal-precursor must wet the CNF support. Secondly, the CNF support must contain anchoring sites in order to immobilize the metal ion precursor entities and later on the metallic metal particles. The hydrophobic as-synthesized carbon nanofibers do not fulfill these prerequisites by the lack of

anchoring sites. Surface activation of the carbon nanofibers by refluxing the support in a mixture of nitric and sulphuric acid resulted in hydrophilic carbon nanofibers with oxygen-containing surface groups. Impregnation on the thus created oxidized carbon nanofibers via water resulted in well dispersed nickel (5-7 nm) on carbon nanofibers with a maximal loading of 10 wt% since this support fulfills both prerequisites. Deposition precipitation via thermal decomposition of urea leads also to a well dispersed nickel phase on the oxidized carbon nanofibers. Using the latter technique we have realized nickel loadings on carbon nanofibers up to 45 wt%.

Introduction

Nickel based catalysts are widely used in processes like hydrogenations [1], hydrodesulphurization [2] and steam reforming of hydrocarbons [3]. In general, these catalysts consist of small nickel clusters (nm range) dispersed on oxidic carriers like SiO_2 and Al_2O_3 .

Nowadays new support materials for metal based catalysts with properties potentially surpassing those of conventional supports are available. Carbon nanofibers (CNF) comprise such a material. It is suitable for both gas and liquid phase applications [4-6]. The material is pure, mechanically strong and chemically inert. Moreover metals can be easily recovered from a spent catalyst by burning-off the support. The inertness of CNF is an advantage in many metal catalyzed reactions because side reactions on the support are suppressed, however, it makes the deposition of metal-precursors difficult due to the lack of anchoring sites. This can be addressed by an oxidative pre-treatment which results in oxygen containing surface groups thus forming anchoring sites while the hydrophilicity is increased [7,8]. By using oxidized CNF it appeared possible to deposit metal-precursors on the surface via impregnation or ion exchange at low loadings with high dispersions and narrow size distributions [4-6,9,10]. Up to now deposition precipitation (DP), which has been developed for preparing highly loaded highly dispersed metal/oxide catalysts [11-18], has not been used for the deposition of metal precursors on CNF. Most likely this is due to the supposed absence of a strong interaction between the support and metal precursor which is thought to be indispensable for DP [11-18]. For metal on oxide catalysts this interaction is believed to be the formation of a surface co-precipitate between the support and the metal precursor. After reduction of the co-precipitate a well dispersed supported metal catalyst is obtained [11-18].

In this chapter, we will show however, that it is possible to prepare highly loaded (~ 50 wt% Ni), highly dispersed Ni/CNF via DP. Furthermore, we compare results with those obtained via impregnation and drying.

Experimental

CNF growth

Fishbone carbon nanofibers were grown from a CO/H₂ mixture at 823 K using a nickel on silica growth catalyst as described elsewhere [4-6,19,20]. After fiber growth the carbon nanofibers together with the remaining Ni/SiO₂ catalyst were collected.

The silica was removed by refluxing the collected product for 2 hours in a potassium hydroxide solution (1M). Subsequently the material was filtered, washed and dried at 393 K. The thus obtained product (CNF with nickel) was divided in two portions, see Figure 1. One portion was refluxed in concentrated hydrochloric acid in order to remove exposed nickel. After washing and drying 'as-synthesized' carbon nanofibers (CNF-as) are obtained. From the second portion oxidized CNF (CNF-ox) were prepared by refluxing the potassium hydroxide pre-treated carbon nanofibers in a mixture of HNO₃ and H₂SO₄ (1:1 v/v) [7,8]. This treatment removes the exposed nickel and induces oxygen containing surface groups on the carbon nanofibers. Some physico-chemical properties of the CNF and nickel loaded CNF are compiled in Table 1.

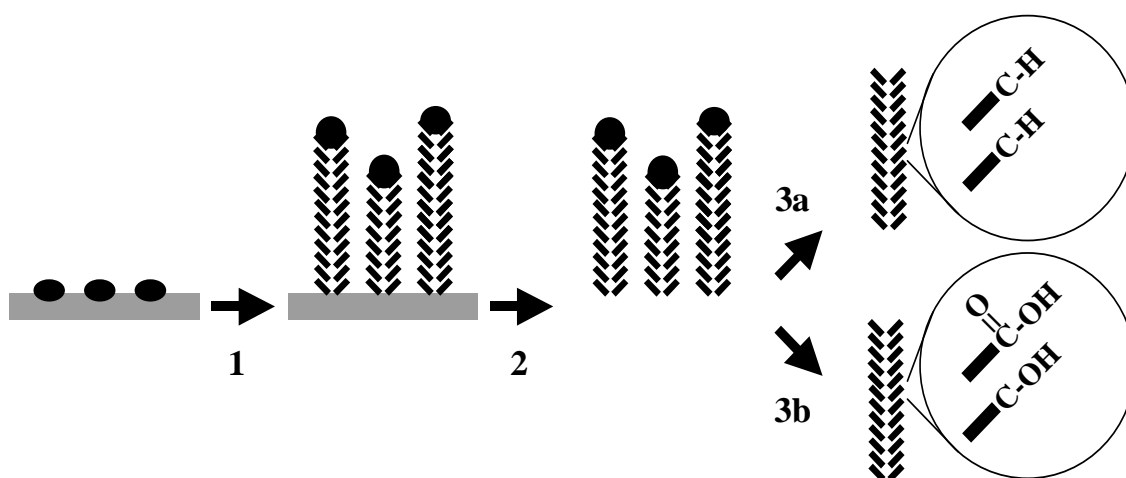


Figure 1: Schematic drawing of fishbone carbon nanofibers growth using a nickel on silica growth catalyst (step 1), the removal of silica by refluxing the rough product in KOH (step 2) and (step 3a) the removal on exposed nickel by refluxing in HCl or (step 3b) removal of exposed nickel by HNO₃/H₂SO₄ and introduction of oxygen containing surface groups.

Incipient wetness impregnation on CNF

The nickel precursor was deposited on the oxidized CNF by both incipient wetness impregnation and deposition precipitation. We prepared with both techniques materials containing 10 wt% of nickel. In addition 30 wt% Ni/CNF-ox was prepared by incipient wetness impregnation while 50 wt% Ni/CNF-ox was prepared via deposition precipitation.

For incipient wetness impregnation 1.0 gram carbon nanofibers was evacuated at room temperature for 30 minutes and the carbon nanofiber supports were once impregnated with of an aqueous solution of nickel nitrate ($[\text{Ni}^{2+}] = 0.2 \text{ g/ml}$) resulting in a 10 wt% metal loading. The impregnated carbon nanofibers were dried overnight at 393 K and subsequently reduced in a 20 vol% hydrogen in argon flow at 773 K for 1 hour. After cooling in argon to room temperature and subsequent exposure to air, the Ni/CNF were stored for further use. For the 30 wt% sample successive impregnations were performed with a solution of 0.2 g Ni^{2+} /ml prepared from nickel nitrate. In between each impregnation the material was dried at 373 K.

Deposition precipitation on CNF

For deposition precipitation 0.8 gram of nickel nitrate hexahydrate was dissolved in 200 ml de-ionized water and 1.5 grams of the oxidized CNF was added. When needed the solution was brought to pH~3 with a few drops of HNO_3 . While stirring, the suspension was brought at 363 K and kept at that temperature during the precipitation. An aqueous solution (10 ml) containing 0.6 g urea was added at the final temperature. After deposition for 18 hours and cooling to room temperature the loaded carbon nanofibers were thoroughly washed, dried at 393 K and subsequently reduced in a 20 vol% hydrogen in argon flow at 773 K for 1 hour at 1 bar. After cooling to room temperature and subsequent exposure to air, the Ni/CNF were stored for further use. In this way 10 wt% Ni on carbon nanofiber samples were prepared.

Characterization

The nickel loading of these systems were established by thermogravimetric analysis (TGA). The same procedure but with a higher concentration of nickel in the solution was applied with the aim of preparing 50 wt% nickel on carbon nanofibers.

The reduced CNF-supported nickel catalysts were examined in a Philips Tecnai-20 FEG TEM operated at 200 kV. Samples were prepared by suspending the fibers in ethanol under ultrasonic vibration. Some drops of the thus produced suspension were brought onto a holey carbon film on a copper grid.

Table 1: Some properties of reduced Ni/CNF materials as function of the preparation history.

Synthesis	Treatment	Loading [wt%]	Particle size[#] [nm]	Ni PSD	S_{BET} [m²/g]
-	-	-	-	-	169
-	Ox	-	-	-	179
IW	Ox	10	9-11	Narrow	162
DP	Ox	10	5-7	Narrow	165
IW	Ox	30	8-60	Broad	167
DP	Ox	45	8-10	Narrow	156

IW = Incipient Wetness Impregnation

DP = Deposition Precipitation

PSD = Particle Size Distribution

= Determined on basis of TEM

Results and discussion

In Figure 2A a TEM micrograph of a reduced 10 wt% Ni/CNF prepared by DP is shown. Figure 2B shows a TEM micrograph the same sample at a higher magnification. Clearly the sample contains well-dispersed metallic nickel particles (6 nm) with a narrow size distribution on the surface of the CNF (Table 1). Also the 10 wt% Ni/CNF sample prepared by impregnation shows well dispersed nickel particles. A TEM analysis revealed that the average nickel particle in this case was 10 nm (Table 1) also with a narrow size distribution.

Thus both techniques lead to well-dispersed metallic nickel at 10 wt% loading (Table 1). This is tentatively explained by the similar processes occurring during preparation independent of the intended deposition method. When it is assumed that the Ni precursor is deposited by sorption on the surface of the oxidized CNF one can calculate that a maximum loading of 10 wt% can be obtained. It must be assumed that 2 oxygen-containing groups per nm² exist [21], the nickel precursor is present as Ni₄ clusters in solution [22] and sorbs as such in a 1 to 1 ratio on the oxygen-containing groups. Please note that the oxygen-containing groups are indispensable since the use of as synthesized CNF resulted in the formation nickel aggregates not attached to the support with a size ranging between 10 and 60 nm, independent of the synthesis technique (a representative TEM micrograph is shown in Figure 3).

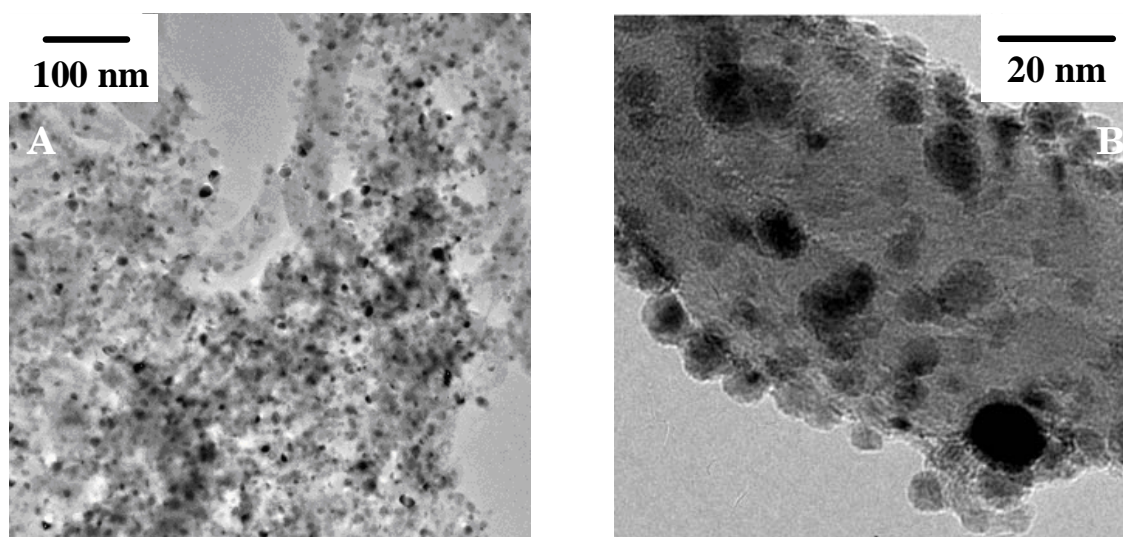


Figure 2: TEM micrograph of reduced 10 wt% Ni/CNF-ox prepared via deposition precipitation, (A) low magnification and (B) high magnification.

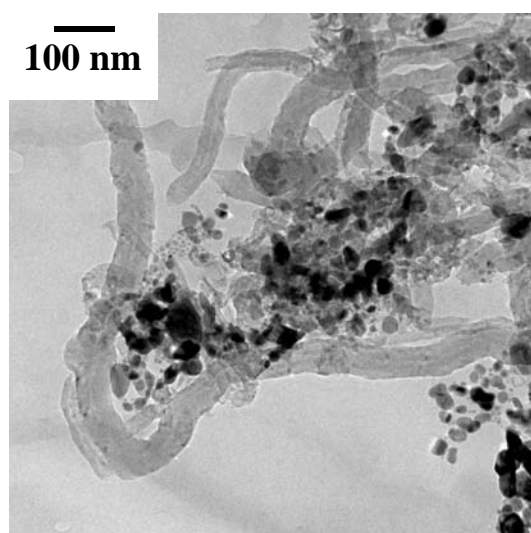


Figure 3: TEM of reduced 10 wt% Ni/CNF-as prepared by deposition precipitation.

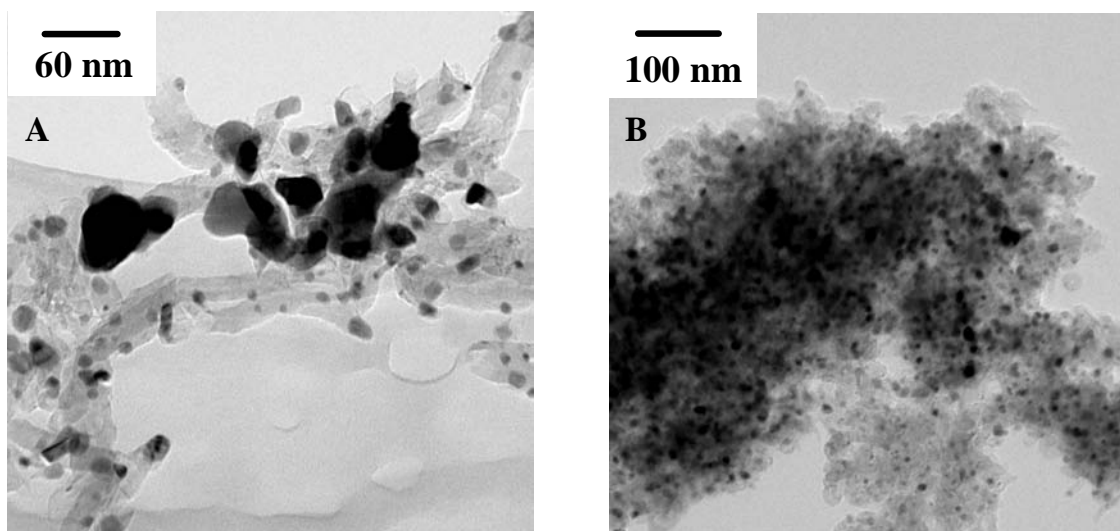


Figure 4: (A) TEM of reduced 30 wt% Ni/CNF-ox prepared via incipient wetness impregnation, (B) TEM image of reduced 45 wt% Ni/CNF-ox prepared via DP.

In order to demonstrate the potential of the DP technique on CNF we prepared 30 wt% Ni/CNF-ox via impregnation and 50 wt% Ni/CNF-ox via DP. The impregnated sample of 8-60 nm (Figure 4A) while the sample prepared by DP contained well dispersed nickel (9 nm) with a narrow-size distribution (Table 1 and Figure 4B). The DP sample contained only 45 wt% of nickel instead of the aimed 50 wt%. The discrepancy between the intended weight loading (50 wt%) and the actual loading (45 wt%) can be explained by the formation of soluble nickel-amine species [11,12] during the deposition.

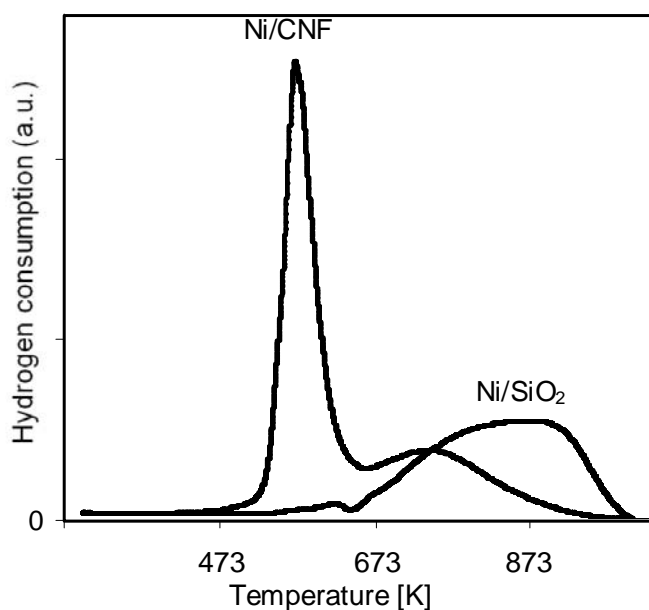


Figure 5: TPR results of 50 wt% Ni/SiO₂ and 45 wt% Ni/CNF-ox.

We have shown above that DP is eminently suitable for the preparation of Ni/CNF catalysts even though the interaction between support and metal precursor is low as can be demonstrated by means of temperature programmed reduction (TPR). In Figure 5 the TPR data of the catalysts precursor i.e., after deposition of the nickel compound onto the support by DP, are shown for Ni/SiO₂ and for Ni/CNF both containing about 50 wt% nickel. Clearly Ni/SiO₂ is reduced at much higher temperature (maximum at 873 K) compared to the Ni/CNF precursor system (573 K). The reduction peak at 773 K in Ni/CNF is most likely due to some gasification of the CNF by hydrogen. The high reduction temperature needed for Ni/SiO₂ is caused by the presence of difficult to reduce nickel-hydrosilicates which is the form in which nickel is deposited during synthesis [11-18]. Nevertheless reduction at 1023 K of this material results in small nickel particles (7 nm) with a homogeneous size distribution. Because Ni²⁺ in Ni/CNF is reduced at a lower temperature (Figure 6) it is evident that it is present in a different form in this system compared to the Ni/SiO₂ system. Since it is now not possible to form a chemical compound between support and metal precursor, like the nickel-hydrosilicate in Ni/SiO₂, we believe that in the Ni/CNF system nickel-hydroxides nucleated on and anchored to the oxygen containing groups of the CNF support are present after deposition. Clearly, reduction of nickel hydroxide proceeds easily (Figure 5).

The weaker interaction between CNF and nickel is also reflected in the evolution of the nickel particle size as function of the reduction temperature. Reduction at 773 K of Ni/CNF resulted in metallic nickel particles of 9 nm (Table 1) while reduction at 1023 K of Ni/SiO₂ resulted in metallic nickel particles of 7 nm. This clearly indicates a somewhat higher thermostability of the Ni/SiO₂ catalyst.

Conclusions

Both deposition precipitation and incipient wetness impregnation applied on oxidized, hydrophilic carbon nanofibers resulted in well dispersed metallic nickel on carbon nanofibers. Impregnation of nickel nitrate in aqueous solutions lead to a maximal nickel loading of 10 wt%, which is restricted by the pore volume of the support and the solubility of nickel salt. Deposition precipitation was shown to combine high nickel loadings (up to 45 wt%) with good nickel dispersions. In this way nickel particles of 9 nm were obtained with a narrow particle size distribution over the surface. The oxygen containing groups on the surface of the carbon nanofibers act as anchor/deposition sites for nickel.

Acknowledgment

The authors acknowledge for their contributions to this work V. Koot (TPR), C. van der Spek (TEM), M. L. Toebes (preparation of Ni/SiO₂), F. Broersma (TGA), and the financial support of STW (grant UPC 5487).

References

1. Hoffmann, G. *The chemistry and Technology of Edible Oils and Fats and their High Fat Products*, Academic Press, (1989). M.V. Rajashekharam, *J. Sci. Ind. Res.*, (1997), 56, 595.
2. Reinhoudt, H.R., Troost, R., Van Langeveld, A.D., Van Veen, J.A.R., Sie, S.T., Moulijn, J.A., *J. Catal.*, (2001), 203, 509.
3. Aasberg-Petersen, K., Bak Hansen, J.H., Christensen, T.S., Dybkjaer, I., Christensen, P.S., Stub Nielsen, C., Winter Madsen, W.E.L., Rostrup-Nielsen, J.R., *Appl. Catal. A-Gen.*, (2001), 221, 379.
4. De Jong, K.P., Geus, J.W., *Catal. Rev.-Sci. Eng.*, (2000), 42, 481.
5. Rodriguez, N.M., Kim, M.-S., Baker, R.T.K., *J. Phys. Chem B.*, (1994), 8, 13108.
6. Phan-Huu, C., Charbonniere, L.J., Ziessel, R., Ledoux, M.J., *Chem. Comm.*, (2000), 19, 1871.
7. Geus, J.W., Van Dillen, A.J., Hoogenraad, M.S., *Mater. Res. Soc. Symp. Proc.*, (1995), 368, 87.
8. Ros, T.G., Van Dillen, A.J., Geus, J.W., Koningsberger, D.C., *Chem. Eur. J.*, (2002), 8, 1151.
9. Liu, Z.-J, Xu, Z., Yuan, Z.-Y, Lu, D., Chen, W., Zhou, W., *Catal. Lett.*, (2001), 72, 203.
10. Toebes, M.L., Prinsloo, F.F., Bitter, J.H., Van Dillen A.J., De Jong, K.P., *J. Catal.*, (2003), 214, 78.
11. Van Dillen, A.J., Geus, J.W., Hermans, L.A.M., Van der Meijden, J., *Proc. 6th Int. Congr. Catal.*, (1977), 2, 677.
12. Hermans, L.A.M., Geus, J.W., *Stud. Surf. Sci. Catal.*, (1979), 3, 113.
13. De Jong, K.P., *Stud. Surf. Sci. Catal.*, (1991), 63, 19.
14. Burattin, P., Che, M., Louis, C., *J. Phys. Chem. B.*, (1997), 101, 7060.
15. Burattin, P., Che, M., Louis, C., *J. Phys. Chem. B.*, (1998), 102, 2722.
16. Burattin, P., Che, M., Louis, C., *J. Phys. Chem. B.*, (1999), 103, 6171.
17. De Jong, K.P., *Curr. Opin. Solid State Mater. Sci.*, (1999), 4, 55.
18. Burattin, P., Che, M., Louis, C., *J. Phys. Chem. B.*, (2000), 104, 10482.
19. Hoogenraad, M.S., Van Leeuwarden, R.A.G.M.M., Van Breda Vriesman, G.J.B., Broersma, A., Van Dillen, A.J., Geus, J.W., *Stud. Surf. Sci. Catal.*, (1995), 91, 263.
20. Toebes, M.L., Bitter, J.H., Van Dillen, A.J., De Jong, K.P., *Catal. Today*, (2002), 76, 33.
21. Toebes, M.L., Unpublished results, Utrecht University, Utrecht, the Netherlands, (2002).

22. Baes Jr, C.F., Mesner, R.E., "The hydrolysis of Cations", John Wiley and Sons, p244, D.T. Richens, "The chemistry of aqua ions", John Wiley and Sons, (1997), 496.

4

Deposition precipitation for the preparation of carbon nanofiber supported nickel catalysts – Study on the mechanism

Abstract

Deposition precipitation of nickel hydroxide onto modified carbon nanofibers has been studied and compared to deposition onto silica. The carbon nanofiber support materials consisted of graphite-like material of the fishbone type with a diameter of 20-50 nm and a specific surface area of 150 m²/g. Modification involved surface oxidation (CNF-O) optionally followed by partial reduction (CNF-OR) or thermal treatment (CNF-OT). Titration of the support materials showed the presence of 0.17 and 0.03 mmol/g carboxylic acid groups for CNF-O and CNF-OR, respectively. For the CNF-OT only basic groups were

present. The deposition precipitation of 20 wt% nickel onto these supports has been studied by time dependent pH and nickel loading studies. With silica nickel-ion adsorption did not occur prior to nucleation of the nickel hydroxide phase at pH=5.6. With CNF-O nickel ion adsorption took place right from the start of the deposition process at pH=3.5 and at pH=5.6 already 4 wt% nickel was adsorbed. Nucleation of nickel hydroxide onto adsorbed nickel ion clusters proceeded subsequently. Characterization of the dried Ni/CNF-O samples with TEM and XRD showed well dispersed and thin (5 nm) platelets of nickel hydroxide adhering to the carbon nanofibers. After reduction at 773 K in hydrogen the Ni/CNF-O contained metallic nickel particles of 8 nm homogeneously distributed over the fibers. With CNF-OR and CNF-OT precipitation of large platelets (> 500 nm) separate from the support took place. Clearly, the presence of carboxylic acid groups is essential to successfully deposit nickel hydroxide onto modified carbon nanofibers.

Introduction

Supported metal and metal oxide catalysts are indispensable for energy and chemical industries to reduce consumption of raw materials and to minimize the production of waste. Control over the preparation of supported metal catalysts is necessary to improve their key properties as activity, selectivity and stability. The most important methodologies to prepare supported catalysts in both industry and academia involve impregnation and drying [1-5], metal-ion adsorption [6-14], deposition precipitation [15-17] and chemical vapor deposition [18-19]. Reviews on catalyst preparation are available both from a practical [20-23] and a fundamental point of view [2, 3, 24].

The advent of nanostructured support materials such as ordered mesoporous materials [25-27], carbon nanofibers [28-31] and carbon nanotubes [32-33] provides opportunities for novel supported metal and metal oxide catalysts. Carbon nanofibers and carbon nanotubes are promising support materials in view of, amongst others, the control of surface properties, chemical inertness, the high accessibility, thermal stability, mechanical strength and tunable bulk density. The field of carbon nanofiber supports has been pioneered by the groups of Baker [34-35], Geus [36-38], Ledoux [39-40] and De Jong [41-43]. Recently, Serp and co-workers [44] have written a review on the status of the use of carbon nanofibers (CNF) and carbon nanotubes (CNT) as support material. In this paper we will focus on the use of carbon nanofibers as support material while using deposition precipitation (DP) for the preparation of

supported nickel catalysts. Nickel-based catalysts are widely used in processes like hydrogenations, steam reforming, amination and hydrodesulphurization.

Deposition precipitation involves the precipitation of a metal precursor onto a suspended support material. Usually precipitation is brought about by a controlled increase of the pH of an aqueous solution of the metal salt in question. Hydrolysis of urea typically at 363 K is a convenient method to slowly increase the pH. This method has been explored by Geus, Hermans, and Van Dillen [45-48] and De Jong [49] and mechanistic studies have been published for nickel-on-silica by Burattin et al. [50-53]. From these studies it is clear that nucleation and growth of the nickel compound – either turbostratic nickel hydroxide or nickel phyllosilicate – coincides with a significant interaction with the silica support. This interaction was studied by pH measurements during synthesis and by characterization of the loaded silica support materials [17, 46, 49-54]. The deposition process including this interaction for silica is summarized in Figure 11A-D.

Deposition precipitation has hardly been studied for carbon-supported catalysts. Using activated carbon Wigmans [55] obtained non-uniform distributions of nickel over the support probably due to intraparticle diffusion limitation during precipitation. Prinsloo [56] prepared Fe/CNT and Co/CNT materials with low metal dispersion most likely due to a low interaction of the metal precursors with the carbon nanotubes. These results might be anticipated since the nature of the carbon support materials strongly deviates from the silica supports and the formation of mixed compounds of the metal precursor and the support is not possible.

Recently, we reported the preparation of highly-loaded, well-dispersed nickel catalysts using DP with surface-oxidized CNF support material [57]. The mechanism of interaction during preparation was not discussed in this preliminary paper. Therefore, we have carried out a detailed study for the preparation of nickel-on-CNF catalysts using deposition precipitation and different types of surface-modified carbon nanofibers with surface groups ranging from acidic to basic. Titrations were done to assess the nature and the number of surface groups on the modified CNF. The measurement of pH during DP in combination with the extent of nickel removal from solution was used to obtain key information on nucleation and growth. These measurements were compared to experiments with a silica support under identical conditions of temperature and concentrations. The precipitated Ni/CNF catalysts were characterized both after drying and after reduction using in particular TEM and XRD.

Experimental

CNF growth

One gram of a calcined 20 wt% Ni/SiO₂ (particle size 425-850 μm) precursor prepared according to Toebe et al. [58] was placed in a quartz reactor and reduced at 973 K. Next, carbon nanofibers were grown at 823 K for 6 hours. Afterwards, the reactor was cooled to room temperature while it was flushed with nitrogen. The resulting product (approx. 5 gram) was collected and coded as CNF-A. From the product silica was removed via a treatment in refluxing 1M KOH solution for 2 hours. The remaining product was refluxed in a mixture of concentrated nitric acid and sulphuric acid (1:1) for 30 minutes. This results in removal of the accessible nickel originating from the growth catalyst and surface oxidation of the carbon nanofibers. After thoroughly washing, the carbon nanofibers were dried over night at 393 K in air (code CNF-O).

In order to reduce the oxygen content of the carbon nanofibers, 0.5 gram of CNF-O was thermally treated in nitrogen atmosphere at 873 K (heating rate 5 K/min) for 30 minutes. The thus obtained fibers were designated CNF-OT.

Another 0.5 gram of CNF-O fibers were partly reduced with lithium aluminum hydride (LiAlH₄) under a dry nitrogen atmosphere. To this end 500 mg of CNF-O was suspended in 50 ml freshly distilled THF while 85 mg LiAlH₄ (Merck) was suspended in 25 ml freshly distilled THF. Under nitrogen flow the LiAlH₄ suspension was carefully added to the CNF-O suspension and the total volume was subsequently stirred for 20 hours. After reaction the mixture was neutralized by slowly adding water to the suspension and resulting CNF were thoroughly washed with 1M HCl and subsequently water. Finally the CNF were dried at 393 K for 18 hours (CNF-OR).

CNF acid-base titrations

Acid-base titrations were carried out using a titralab-TIM880 automatic titration setup equipped with a combined pH electrode and automatic burettes. All titrations were carried out at room temperature using 50 mg ground CNF support and 70 ml water. During the titration N₂ gas was flushed over the liquid to avoid CO₂ to dissolve into the water. The titrations of the CNF supports were done after the addition of 5 ml 0.10 M oxalic acid to the support slurry. After stabilization of the pH, titration with NaOH (0.010 M) was started and continued to pH 10. Also a blank experiment was done with 70 ml H₂O and 5 ml oxalic acid solution. The number of acid sites present on the CNF supports was determined by the difference in volume added compared to the blank. For example the difference in volume added between blank and sample at pH 8

provided the required amount of base to neutralize all groups with a $pK_a < 8$. For basic materials (CNF-OT) we report pK_b values rather than pK_a .

Nickel deposition on CNF materials

20 wt% Ni on powdered CNF-O, CNF-OT or CNF-OR were batch-wise prepared via DP using aqueous solutions. A reactor vessel equipped with baffles, pH electrode, thermometer and stirrer was loaded with 250 ml water, 300 mg of CNF support and 371 mg of nickel nitrate hexahydrate (Acros 99%). The pH was adjusted to ~ 3.5 by adding a few drops of diluted HNO_3 (Merck). After heating this mixture to 363 K, a solution of 230 mg urea (Acros) in 3 ml water was added. After 18 hours, the slurry was cooled to room temperature and filtered. The loaded CNF were thoroughly washed and dried at 393 K for 18 hours. The obtained supported nickel precursor was reduced in a 100 ml/min flow of 20 vol % hydrogen in nitrogen at 573 K (heating rate 5 K/min) for 1 hour. After cooling to room temperature and subsequent gradual exposure to air, the catalyst was collected.

20 wt% Ni on silica (Degussa, Aerosil, specific surface area 200 m^2/g) was prepared via the same procedure as described for CNF.

Nickel-ion concentration during deposition precipitation and loading

The aqueous nickel-ion concentrations during the DP process were determined via flame atomic absorption spectroscopy (AAS) at 352.5 nm using a Varian Spectra 10 apparatus. Samples (1 ml) were collected from the DP solution, acidified with diluted HNO_3 and diluted to a concentration between 1-25 ppm, which was the range of the nickel calibration curve.

Nickel ion-adsorption on the support, before urea was added to the suspension, was determined both via the liquid phase as described above and via the 'solid phase'. In the latter case, 300 mg support was suspended in 250 ml water and the pH was set to ~ 3.5 . Next 371 mg nickel nitrate was added to the solution. The reaction mixture was heated to 363 K. After 0.5 hours the support was collected by filtration, washed thoroughly and dried at 393 K. 100 mg CNF-O (including the adsorbed nickel) was resuspended in 50 ml of 0.1 mol/l HNO_3 ; after filtration the nickel-ion concentration in the aqueous phase was determined via AAS as described above. For silica 150 mg was resuspended in 50 ml of 0.1 mol/l HNO_3 to analyze the amount of nickel adsorbed.

With thermal gravimetric analysis (TGA) the loading of nickel on the CNF was verified. The loaded fibers were heated in 5 vol% oxygen in nitrogen to 1173 K (ramp 5 K/min). Resulting yields were corrected for the amount of nickel in unloaded CNF-O fibers.

Characterization

Samples were prepared for TEM by suspending the fibers in ethanol under ultrasonic vibration. Some drops of the thus produced suspension were brought onto a holey carbon film on a copper grid. The grids was transferred to a Technai transmission electron microscope operated at 200 KeV with a FEG. Scanning Electron Microscopy, performed with a Philips XL30 FEG apparatus, was used to assess the morphology of the carbon nanofiber bodies.

For XRD an Enraf Nonius PDS 120 powder diffractometer system equipped with a position-sensitive detector with a 2 theta range of 120° using Co K α_1 ($\lambda=1.78897$ Å) radiation was used.

Prior to the physisorption measurement the samples were dried at 473 K. For N₂ physisorption at 77 K a Micromeritics Tristar 3000 apparatus was used.

The total pore volume based on mercury porosimetry was determined using Pascal 440 apparatus at 296 K. With this setup pore radii between 7500 and 1.8 nm were analyzed.

Results and discussion

Carbon nanofiber supports

The as-synthesized (CNF-A), the purified and surface-oxidized (CNF-O) and the oxidized-reduced (CNF-OR) carbon nanofibers have been characterized by XRD (Figure 1). A broad and intense diffraction line close to 30° 2 θ and weaker lines at 50°, 62° and 95° reveal the graphite-like character of the CNF materials. With the CNF-A the presence of metallic nickel is apparent from the XRD pattern. For CNF-O and CNF-OR this nickel has been largely removed although some encapsulated nickel is still present (< 0.1 wt%).

SEM and TEM images of CNF-A are displayed in Figure 2. The macroscopic CNF bodies or skeins have a size of 0.3 - 0.8 mm. The mechanically strong bodies consist of interwoven fibers with a diameter of 20-50 nm (Figure 2B). The individual fibers consist of turbostratic graphite-like material while the graphene sheets run under an angle with the main axis of the fiber (Figure 2C). These so-called fishbone or herringbone type arrangement of the graphene sheets is characteristic of the carbon nanofibers. It has been checked that neither the mesoscopic (Figure 2B) nor the microscopic (Figure 2C) structure did change upon further treatment of the fibers (samples CNF-O, CNF-OT, CNF-OR).

The texture of the support materials has been studied using nitrogen physisorption and mercury porosimetry, the results of which are summarized in Table 1. From t-plot analysis it was established that micropores (<2 nm) were absent in all the materials studied. The specific surface area of the CNF-O and CNF-OR materials of $\sim 150 \text{ m}^2/\text{g}$ can be largely attributed to the external surface of the cylindrical fibers. The pore volume obtained from nitrogen physisorption of 0.3-0.4 ml/g (Table 1) must be present in pores <100 nm in view of the technique limitations. These mesopores represent the open space between closely packed fibers. The presence of macropores can be deduced from the larger pore volume obtained from Hg-porosimetry compared to that obtained from N_2 physisorption. For CNF-O the macropore volume amounts to 0.26 ml/g and is in line with the large voids between fibers that can be observed in Figure 2B.

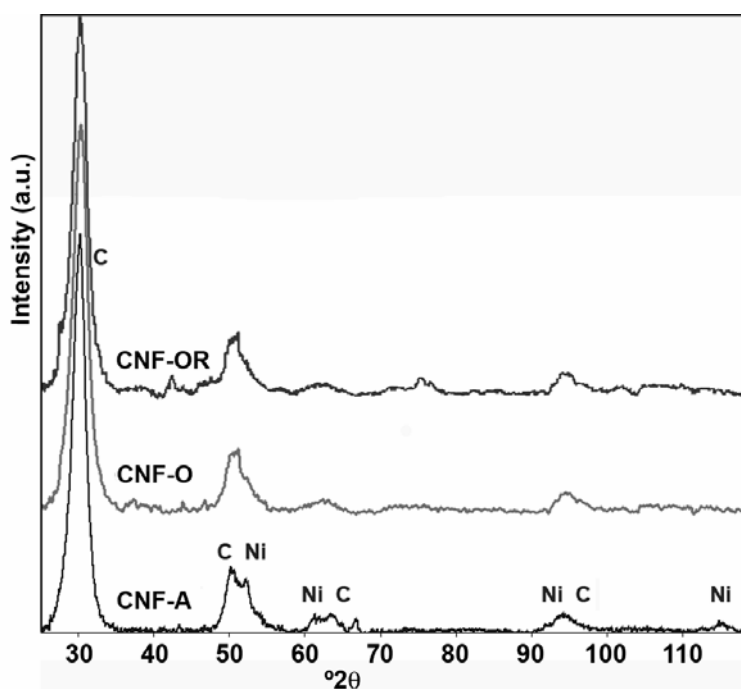


Figure 1: X-ray diffraction pattern of untreated (CNF-A), surface oxidized (CNF-O) and reduced carbon nanofibers (CNF-OR).

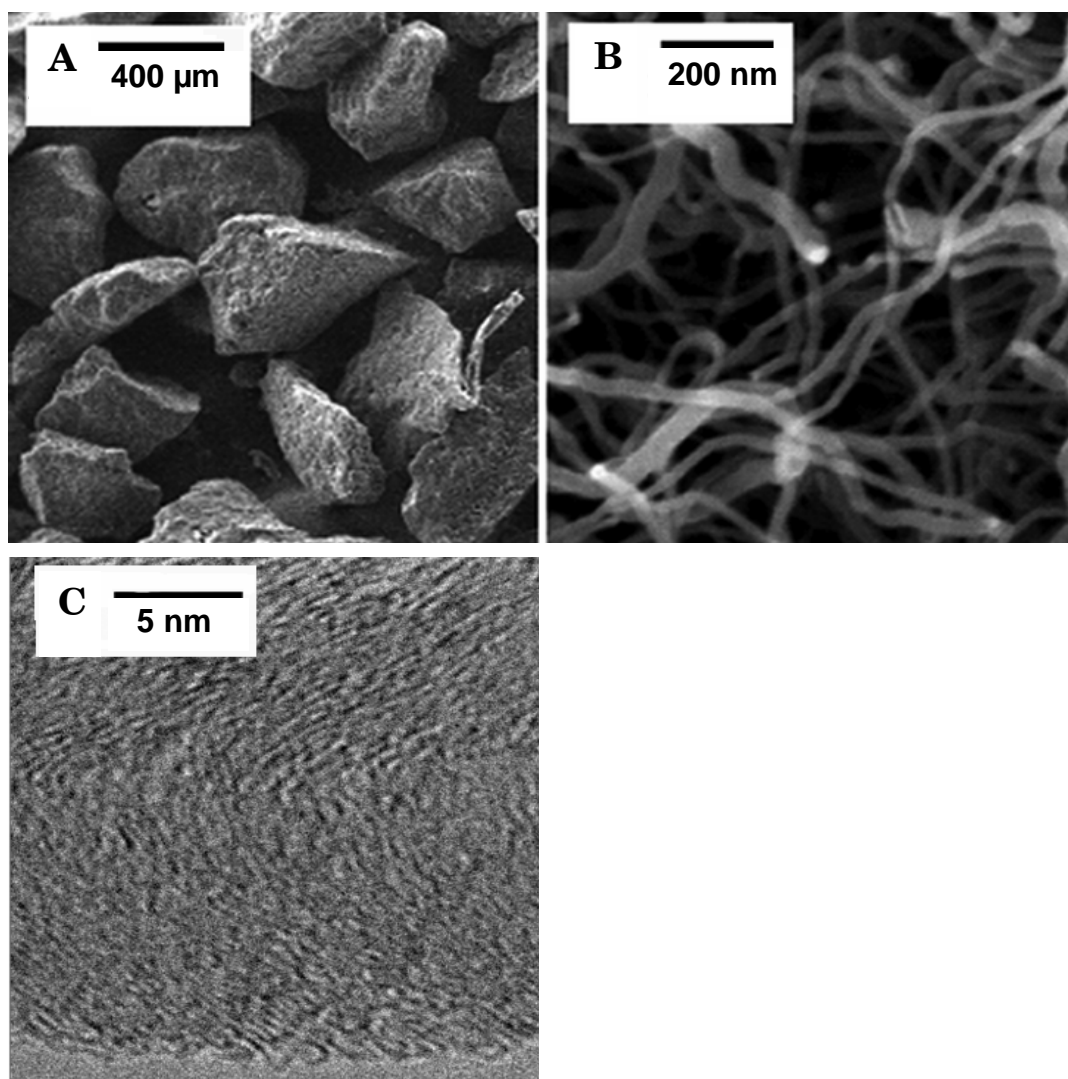


Figure 2: (A) Carbon nanofiber bodies at low magnification in SEM; (B) At higher magnification the interwoven fibers are visible in the SEM image; (C) HRTEM image of a single fish-bone type carbon nanofiber.

Table 1: Physical properties of different treated carbon nanofiber support materials.

CNF type	S_{BET} [m^2/g]	PV_{meso} [ml/g]	ϕ_{pore} [nm]	PV_{total} [ml/g]
CNF-O	150	0.32	15	0.58
CNF-OR	152	0.36	14	n.d.
CNF-OT	172	0.37	14	n.d.

n.d.: not determined, PV_{meso} : mesopore volume, ϕ_{pore} : average pore diameter, PV_{total} : total pore volume based on Hg porosimetry

Titration experiments in aqueous suspensions have been done similar to those described by Boehm [59-60]. In view of the absence of micropores in the CNF skeins the equilibration during titration was fast in all cases. For CNF-O the amount of base added to arrive at a certain pH in all cases exceeds the amount needed with the blank solution (Figure 3). From this the acidic surface groups present on CNF-O are revealed. The oxidation treatment applied to obtain CNF-O is known to lead to formation of a range of oxygen-containing groups, viz. carboxylic acid, carboxylic anhydride, lactone, phenolic quinone and cyclic peroxide groups [28, 30, 37, 59-62]. Roughly speaking, carboxylic acid groups display $pK_a < 5$ and OH-groups attached to large polyaromatic rings $pK_a = 8-9$ [64-68]. The broad range of pK_a values is reflected by the low slope of the titration curve for CNF-O compared to that of the blank. The differences between the blank and CNF-O curves has been established at different pH values and from that the amount of acid groups with different ranges of pK_a have been calculated and are summarized in Table 2. Taking into account the specific surface area (Table 1) and the total number of sites with $pK_a < 8$ of 0.32 mmol/g (Table 2) we calculate 1.3 oxygen-containing surface groups per nm^2 for CNF-O. This number is well in line with a study of Toebe et al. [63] on the surface oxidation of carbon nanofibers.

For CNF-OR the results of Figure 3 and Table 2 show that the total number of oxygen-containing groups has not decreased to a large extent as a result of the reduction treatment. However, the number of strongly acidic sites in particular carboxylic acid groups ($pK_a < 5$) has decreased substantially. From the data of Table 2 it is apparent that the number of phenol-type groups ($pK_a = 8-9$) on CNF-OR is larger than that of CNF-O. The chemical reduction of carboxylic acid groups with $LiAlH_4$ has clearly led to formation of additional phenol-type groups although the total number of groups has decreased slightly.

Table 2: Oxygen containing surface groups on different treated carbon nanofibers.

CNF-type	Surface groups [mmol/gram]			
	$pK_a < 5$	$pK_a 5-8$	$pK_a 8-9$	Total
CNF-O	0.17	0.15	0.08	0.40
CNF-OR	0.03	0.15	0.13	0.31

CNF-type	Surface groups [mmol/gram]			
	$pK_b 4-5$	$pK_b 5-8$	$pK_b 8-9$	Total
CNF-OT	0.03	0.03	0.00	0.06

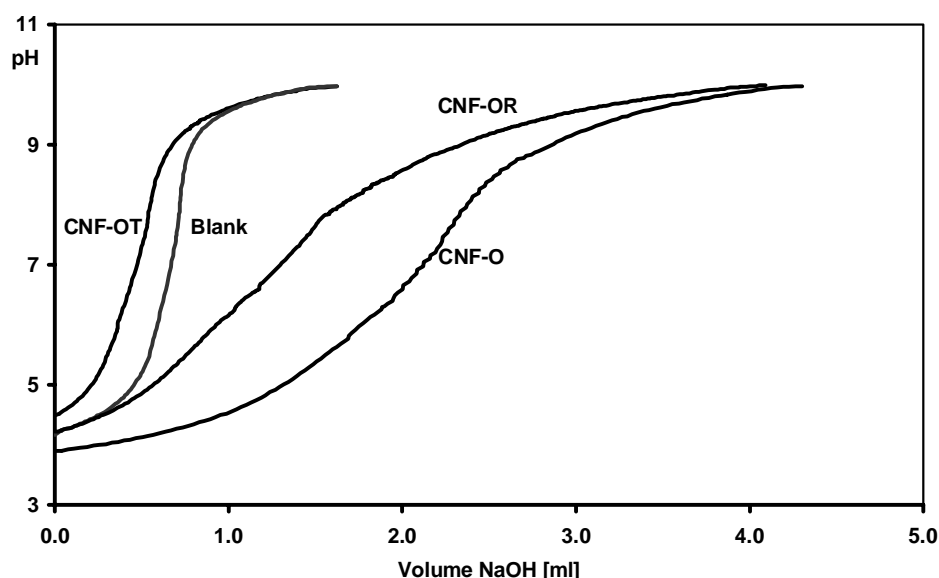


Figure 3: Titration curves of CNF-O, CNF-OR, CNF-OT and the blank solution without support.

With CNF-OT the pH curve runs left of the blank curve indicating the base character of this material. In line with literature [29, 60, 69], thermal treatment has led to removal in particular of carboxylic acid groups that give rise to formation of basic groups on the one hand and reduction of the total number of oxygen-containing groups on the other hand. The total number of basic sites with $pK_b < 8$ is obtained by the differences at $pH=6$ assuming equal alkali consumption at $pH=10$ and amounts to 0.06 mmol/g (cf. Table 2).

Deposition precipitation experiments

Deposition precipitation of nickel onto a suspended silica support was monitored with pH measurements. The results are summarized in Figure 4 (curve 4) together with blank experiments of urea only (curve 1), urea with silica (curve 2) and urea with nickel nitrate (curve 3). In all cases an initially rapid increase of pH is observed. This increase is caused by neutralization of the nitric acid present by the ammonium hydroxide generated by the hydrolysis of urea, reaction (1).



At more elevated pH the rate of increase drops for a number of different reasons. For the urea-only system the pH levels of around 7 due to, on the one hand, buffering effects and conversion of carbon dioxide into bicarbonate and, on the other hand, evaporation of ammonia, reaction (2).



With both urea and silica present the pH runs slightly below the urea-only case (Figure 4, curve 2). Earlier Burattin et al. [51] have explained this deviation between the two curves as being due to the acid-reacting silanol groups present at the support. With urea and nickel nitrate (Figure 4, curve 3) the pH curve coincides with urea only until pH=5.5. Beyond pH=5.5 the presence of nickel ions appears to retard the rise of pH. Hydrolysis of nickel ions starts at this value of pH according to reaction (3)



and in line with earlier proposals [15,48,51]. The maximum of the pH curve (curve 3, pH=6.4, t=2.0 h) is attributed to a super saturated solution and the nucleation of a solid phase, viz. $\text{Ni}(\text{OH})_2$ [10, 46]. Subsequently, the pH drops slightly to a (pseudo-)steady state value of 6.3. This value coincides roughly with the solubility product of nickel hydroxide [70-71].

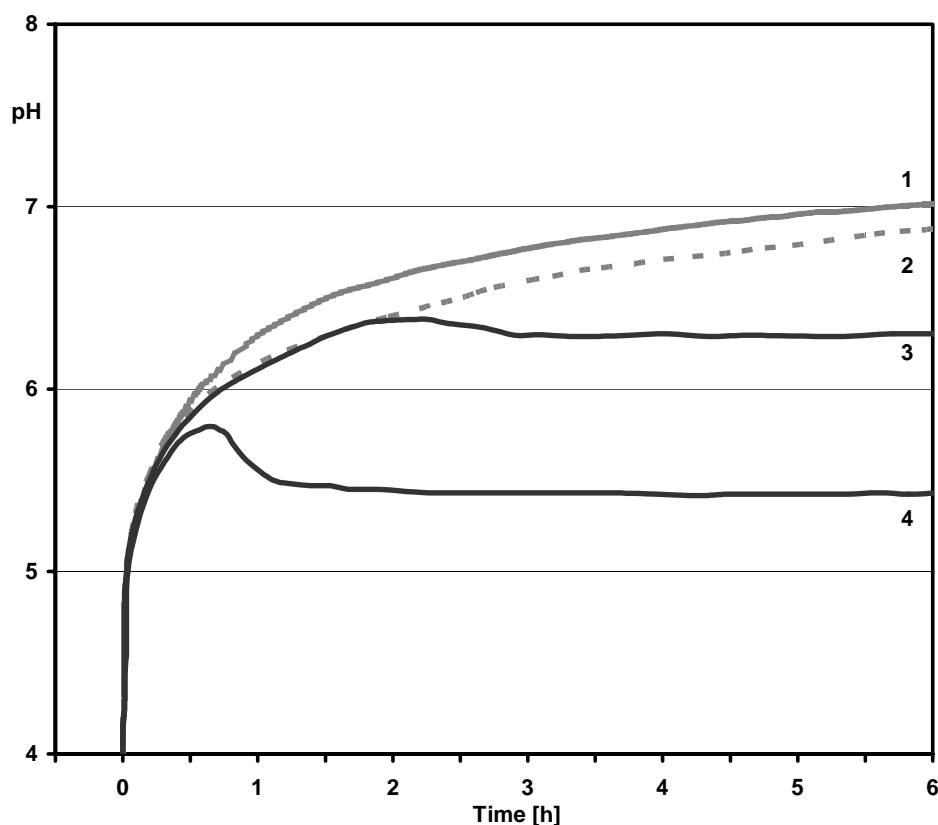
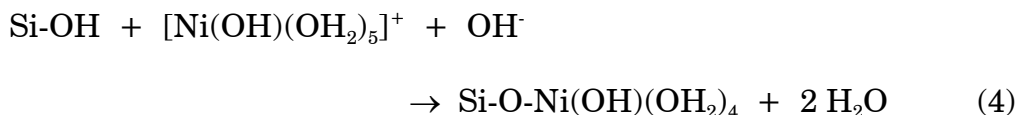


Figure 4: pH development during DP process for nickel-on-silica at 363 K with 15.3 mmol/l urea. (1) Urea only; (2) 1.2 g/l silica; (3) 5.1 mmol/l nickel nitrate; (4) 5.1 mmol/l nickel nitrate and 1.2 g/l silica.

With urea, nickel and silica present (Figure 4, curve 4) a maximum of pH occurs at $t=0.7$ h and $\text{pH}=5.8$. Clearly, nucleation of a new phase occurs much earlier in the process of urea hydrolysis pointing to formation of a nickel phase that is more stable than bulk $\text{Ni}(\text{OH})_2$. According to the literature [50, 51] this phase is turbostratic nickel hydroxide in strong interaction with silica that is converted into a nickel phyllosilicate after prolonged precipitation. For this nickel phase the solubility as apparent from the steady state $\text{pH}=5.4$ is lower than that of unsupported nickel hydroxide ($\text{pH}=6.3$). The nucleation has been suggested to be preceded by nickel-ion adsorption, a theme that we will discuss more extensively below. Here it suffices to say that the pH curves 3 and 4 hardly deviate from each other prior to the maximum in curve 4, which might suggest that nickel ion adsorption onto silica is not extensive below $\text{pH}=5.8$.

As a preliminary conclusion we propose that the adsorption of nickel ions and the nucleation coincide and can be represented by reaction (4).



First we turn now to the experiments with CNF supports. The pH curves of deposition precipitation onto CNF supports together with relevant blank experiments are summarized in Figure 5. From the experiment with urea and CNF-O (curve 1) it appears that the pH levels off slightly above $\text{pH}=7$. In fact this curve coincides largely with curve 1 of Figure 4 (urea only) thus proving that the number of acid groups of CNF-O is not sufficient to affect significantly the pH curve. From the acid site density (Table 2) and the amount of CNF-O in the reaction vessel, the total amount of support acid groups with $\text{pK}_a < 5$ can be calculated to be 0.2 mmol/l whereas the initial urea concentration is 15.3 mmol/l. These values rationalize the very limited impact of CNF-O on the pH increase.

The precipitation of unsupported nickel (no support, curve 2 in Figure 5) has been discussed above. For the Ni/CNF-OT (curve 3) the pH increase largely coincides with curve 2. The initial pH rise is slightly steeper and it is tempting to ascribe this to basic groups present on this support (Table 2). Admittedly, also the number of basic groups is small and a full explanation for the steeper rise is lacking at this point in time. More importantly, the precipitation of nickel with CNF-OT largely takes place at $\text{pH}=6.3$, very close to the precipitation plateau for bulk nickel hydroxide. From this we expect that nickel hydroxide precipitates largely separate from the support with CNF-OT. Further characterization of the samples obtained will shed further light on this (*vide infra*). For CNF-OR similar results are obtained (Figure 5, curve 4) albeit that

at intermediate time ($t < 3$ h) a more significant deviation from the blank experiments is apparent. This deviation is now first discussed for CNF-O (Figure 5, curve 5).

With CNF-O (Figure 5, curve 5) the pH increase drops below that of the blanks (curves 1 and 2) already at $\text{pH} = 4.5$, close to time zero. Nucleation of a new phase, most likely nickel hydroxide, is characterized by a maximum of $\text{pH} = 5.8$ that occurs much later, viz. $t = 2.8$ h. Again, the number of acid groups on CNF-O is by far not sufficient to delay the rise of pH over prolonged times. The only explanation that remains, is that significant amounts of nickel containing species are deposited prior to the maximum of pH has been reached. Since the pH values apparent with CNF-O are significantly below that observed with CNF-OT and CNF-OR it is likely that a nickel phase interacting with CNF-O is obtained.

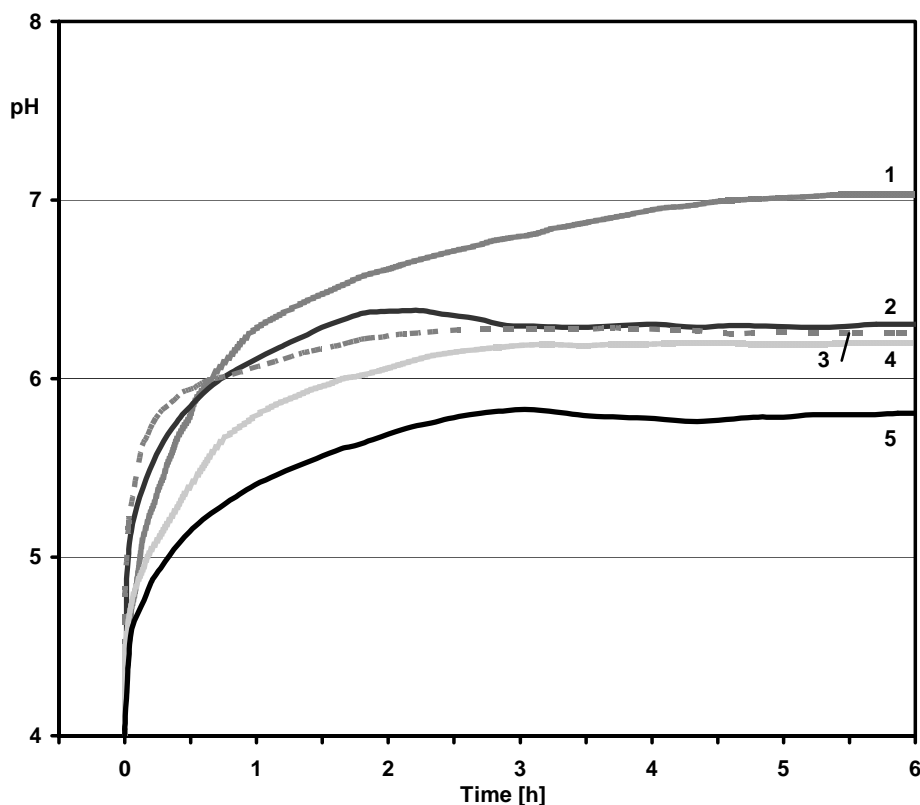
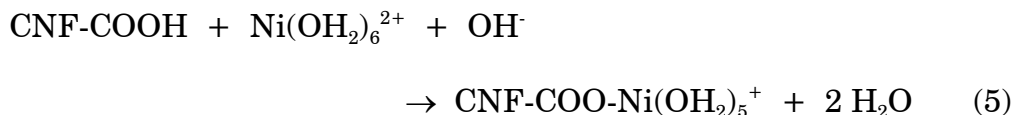


Figure 5: pH development during DP process for nickel-on-CNF at 363 K with 15.3 mmol/l urea. (1) 1.2 g/l CNF-O; (2) 5.1 mmol/l nickel nitrate; (3) 5.1 mmol/l nickel nitrate and 1.2 g/l CNF-OT; (4) 5.1 mmol/l nickel nitrate and 1.2 g/l CNF-OR; (5) 5.1 mmol/l nickel nitrate and 1.2 g/l CNF-O.

In order to obtain more insight we have determined the amounts of nickel present on the silica and the CNF-O supports as a function of time. The results are summarized in Table 3 and Figure 6. With silica until $t=0.7$ h the loading of nickel is zero within the experimental error. Beyond $t=0.7$ h the loading seems to increase linearly with time although data do not allow firm statements about the kinetics of deposition. After 24 hours with SiO_2 quantitative precipitation of Ni^{2+} has taken place, whereas about 80% of Ni^{2+} has been removed from solution with CNF-O.

With silica extensive nickel-ion adsorption does not take place for $\text{pH}<5.8$ and adsorption coincides with nucleation of a new nickel phase (equation 4) at the maximum of the pH curve. The nickel loading at zero time, i.e. before addition of urea, for CNF-O amounts to 0.85 wt% Ni, which corresponds to 0.14 mmol nickel per gram support. Since hydrolysis of the nickel aqua ions does not take place at such a low pH, the adsorption is described by reaction (5).



If we assume that only acid sites with $\text{pK}_a < 5$ are involved in reaction (5) the ratio of nickel over acid sites amount to 0.84 mol/mol, close to unity. Beyond time zero a smooth and linear increase of the nickel loading with time is observed for CNF-O (Figure 6B). At the maximum $\text{pH}=5.8$ at $t=2.8$ h the nickel loading from interpolation of the data is estimated at 3.8 wt% Ni or 0.65 mmol/g that corresponds to Ni/acid-site ratio of 3.8 ($\text{pK}_a < 5$) or 2.0 ($\text{pK}_a < 8$) mol/mol. The growth of bi-nuclear or larger complexes of nickel on the CNF-O support coincides with extensive consumption of hydroxyl ions as revealed by a significant delay of the increase of pH between $\text{pH}=3.5$ to $\text{pH}=5.8$ (Figure 6A). This consumption of hydroxyl ions can be accounted for by reaction (6) for which bi-nuclear nickel complexes are assumed.

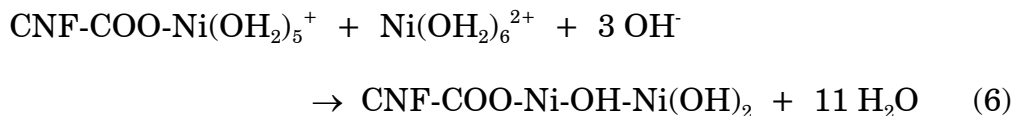


Table 3A: pH and nickel loading during DP process onto CNF-O and the corresponding nickel loading per active site on the support surface. Deposition time starts with the addition of urea to the solution.

Time [h]	pH at 363 K	Ni-loading [wt%] (Yield [%])	Ni/site $pK_a < 5$ [mol/mol]
0.0*	3.1	0.9 (4)	0.9
0.5	5.1	1.5 (7)	1.5
1.5	5.5	2.3 (12)	2.3
2.5	5.8	3.6 (18)	3.6
4.0	5.7	4.6 (22)	4.7
24	5.7	15.3 (77)	18
26	5.7	15.5 (78)	18

*measured prior to urea addition; both solid and liquid phase analysis, see experimental session.

Table 3B: pH and nickel loading during DP process onto silica and the corresponding nickel loading. Deposition time starts with the addition of urea to the solution.

Time [h]	pH at 363 K	Ni-loading [wt%] (Yield [%])
0.0*	3.2	0.0 (0)
0.25	5.3	0.2 (1)
0.50	5.7	0.2 (1)
0.75	5.8	0.0 (0)
1.0	5.7	0.8 (4)
2.7	5.4	1.9 (10)
5.0	5.4	5.4 (27)
24	5.4	20 (100)

*measured prior to urea addition; both solid and liquid phase analysis, see experimental session.

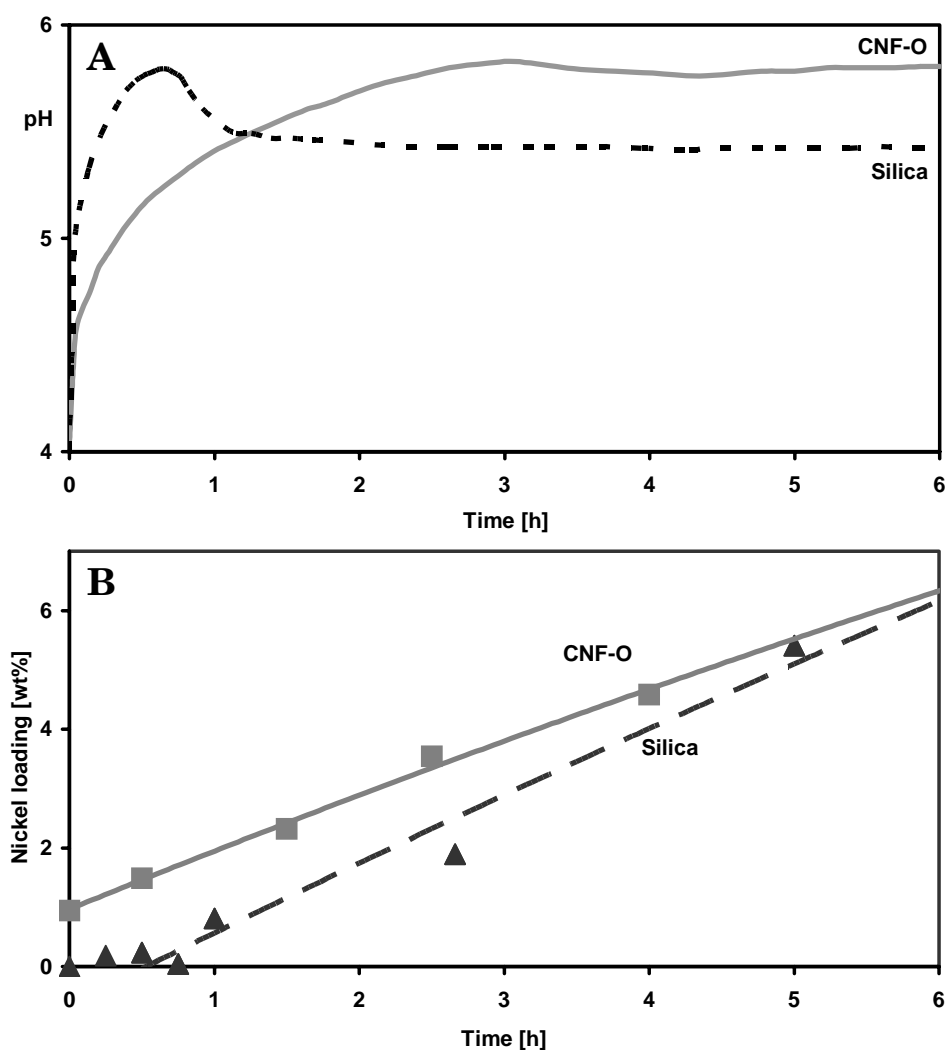


Figure 6: (A) pH curves of DP process onto CNF-O and silica, (B) nickel loading as function of deposition time.

Beyond $t=2.7$ h it is assumed that the small nickel clusters assist in nucleation that leads to a nickel hydroxide phase ($\text{pH}=5.7$). In order to study this phase we turn in the next section to the characterization of the CNF-supported nickel samples obtained after washing and drying.

Comparison of the pseudo steady region of nickel deposition (Figure 6, $t=1-5$ h) shows that the rate of deposition onto silica exceeds that onto CNF-O. In order to understand this difference of rates the lower steady state pH with silica is of importance. It has been argued in the past [49] that the rate-determining step for DP is the hydrolysis of urea, the rate of which is not dependent on pH. However, the evaporation of ammonia (reaction 2) will be more important at more elevated pH thus lowering the selectivity of the utilization of urea for precipitation of nickel hydroxide.

Characterization of nickel-loaded carbon nanofibers

The TEM images of CNF-O and Ni/CNF-O obtained by deposition precipitation are displayed in Figure 7. The rather smooth unloaded carbon nanofiber (Figure 7A) has turned into a fiber with many striations (Figure 7B). We assign the striations to platelets of nickel hydroxide with dimensions of 40-50 nm along the basal plane and 5-10 nm thickness. The platelets adhere to the surface of CNF-O as can be deduced from Figure 7B and from the fact that more extensive TEM studies revealed the absence of free nickel hydroxide platelets on the carbon film. Some platelets stick out of the fiber and are most likely edge bonded whereas other platelets run parallel with the main axis of the fiber and adhere via the basal plane of the nickel hydroxide. For Ni/CNF-OR and Ni/CNF-OT electron microscopy images were obtained as well and a representative one for both samples is shown in Figure 8. With the lower magnification of Figure 8 carbon nanofibers (~ 30 nm diameter) and a large platelet of nickel hydroxide (> 500 nm) separate from each other are apparent. This points to precipitation of nickel hydroxide in the bulk solution as was already suggested before upon considering the pH curves of Figure 5.

XRD patterns of the dried samples corrected for graphite contributions are shown in Figure 9. Broad diffraction lines for the nickel hydroxide phases are apparent in all cases. The intensities of peaks do vary considerably, however, for the samples with similar nickel loadings. For the CNF-O supported nickel phase a very broad and low-intensity diffraction pattern is apparent. The low-angle diffraction line peaks around $17^\circ 2\theta$ which corresponds to a d-value of 6.2 \AA characteristic of the stacking of brucite-type layers of $\alpha\text{-Ni(OH)}_2$. This nickel hydroxide phase consists of turbostratic, defect-rich nickel hydroxide with anions such as carbonate or nitrate intercalated between the brucite layers [50]. The very weak but sharper peak at $39^\circ 2\theta$ can be attributed to an in-plane diffraction line of the nickel hydroxide. The broad lines relate to both the small size and the low degree of crystallinity of the $\alpha\text{-Ni(OH)}_2$ platelets present in the CNF-O sample, well in line with the TEM results. For the CNF-OR and the CNF-OT supported samples more intense diffraction patterns are obtained with an additional peak at $23^\circ 2\theta$ or $d = 4.6 \text{ \AA}$ assigned to the (001) line of $\beta\text{-Ni(OH)}_2$, a more ordered form of nickel hydroxide. Clearly, larger and more ordered platelets of nickel hydroxide are present in the latter two samples, again in accordance with TEM results. A closer inspection of the $17^\circ 2\theta$ lines of CNF-OT and CNF-OR sample suggests a bi-modal distribution of platelets. In other words next to large crystals of nickel hydroxide separate from the support some smaller platelets might be present.

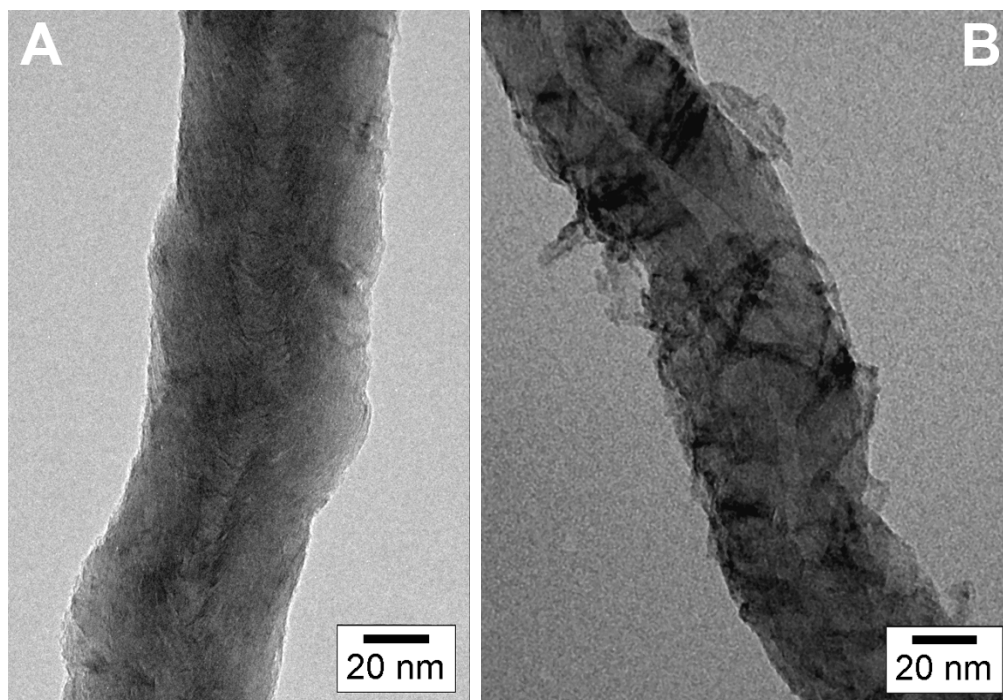


Figure 7: TEM image of a bare carbon nanofiber (A) and a dried nickel hydroxide loaded CNF-O fiber (B).

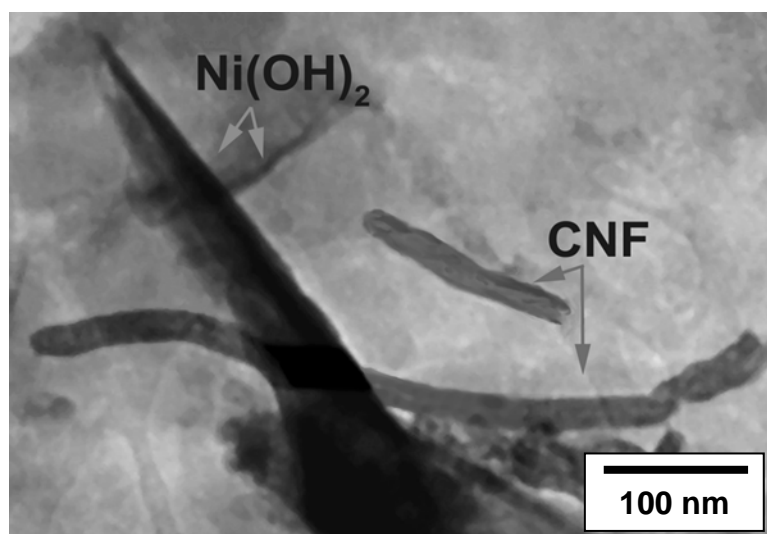


Figure 8: TEM image of large platelets of nickel hydroxide (dark) which are separated from CNF-OR fibers.

Briefly, we return to the pH data of Figure 5 that reveal a lower steady state pH ($t > 3\text{h}$) for precipitation onto CNF-O (curve 5) than for unsupported nickel hydroxide (curve 2). Following the above characterization the lower pH for CNF-O cannot be due to a different nickel phase (cf. Figure 9). Tentatively, the lower pH is ascribed to kinetic phenomena, viz. the much higher surface area of the nickel hydroxide phase for the supported case leads to faster precipitation that maintains a lower pH. This kinetic basis of the DP onto CNF-O is less robust than the thermodynamic basis with silica that relies on a more stable nickel hydroxide phase. This conclusion is supported by the experimental observation that a powdered CNF support is mandatory to prevent bulk precipitation during the preparation process, whereas DP with silica can also be carried out with granules [49].

For sample Ni/CNF-O after reduction at 773 K TEM results are displayed in Figure 10. The metallic nickel particles are evenly distributed over the fibers and well dispersed with an average particle size of 8 nm. The latter average particle size has been confirmed by XRD line broadening (data not shown). The thermal stability of this Ni/CNF-O catalyst is high as apparent from the particle size in combination with the reduction temperature. A more detailed study of the final metallic catalyst including stability and catalytic properties is outside the scope of this paper and will be published elsewhere.

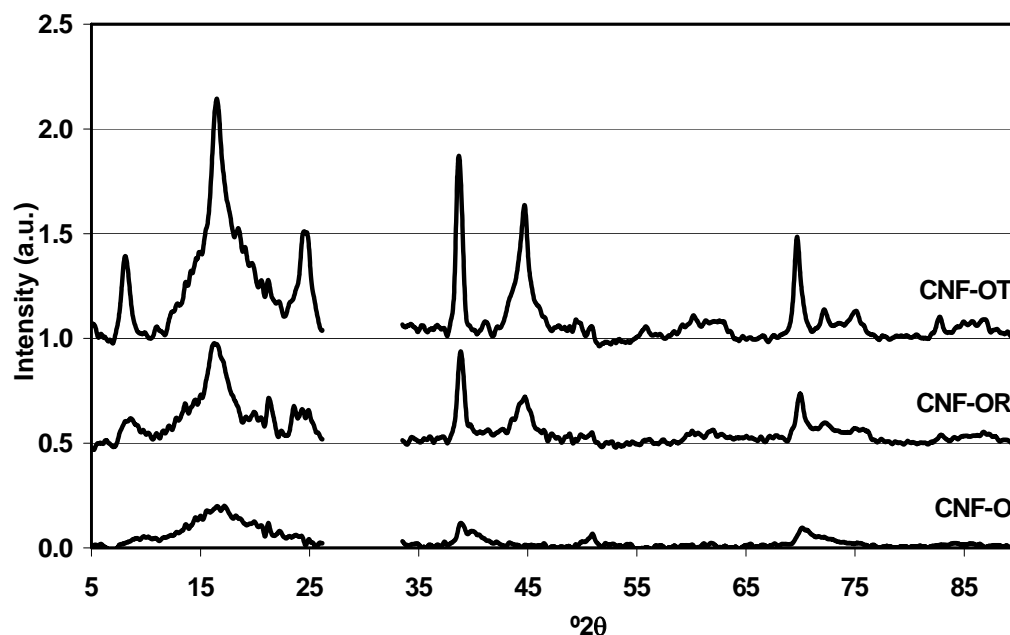


Figure 9: XRD patterns of dried nickel hydroxide precipitates on CNF-O, CNF-OR and CNF-OT. Patterns were normalized to the graphite (002) reflection and the graphite contributions have been subtracted.

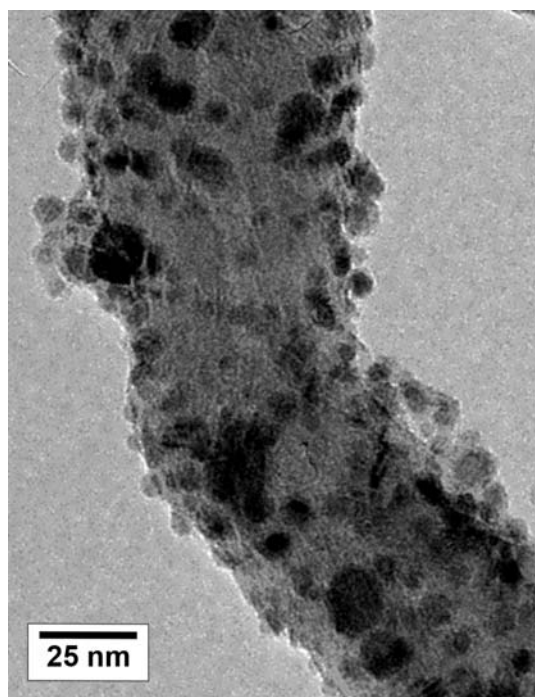


Figure 10: TEM image of nickel particles dispersed on CNF-O after reduction at 773 K.

Mechanism of deposition precipitation of nickel

In Figure 11 the proposed model for precipitation of nickel onto silica and carbon is summarized. The mechanism for nickel-on-silica (A-D) resembles that described by Buratin et al. [51] with one exception, viz. ion adsorption does not take place prior to the nucleation of the supported nickel phase at our experimental conditions (Figure 11A). At nucleation silanol groups interact with nickel ions which results in the formation of Si-O-Ni(OH)(OH)_2 (Figure 11B and C). The strong chemical interaction between nickel hydroxide and silica is indicated by the formation of nickel phyllosilicate (Figure 11D).

For the carbon support with carboxylic acid groups, nickel-ion adsorption does occur prior to nucleation of Ni(OH)_2 , Figure 11E. Starting at $\text{pH}=3.5$ all acid sites are already occupied by nickel-ions while close to nucleation ($\text{pH}=5.8$) about 4 nickel ions per acid site have been adsorbed (Figure 11F and G). Some of these small nickel clusters serve as nucleation sites for the formation of nickel hydroxide platelets (Figure 11H). Growth of these platelets occur at $\text{pH}=5.7$, just below the pH at nucleation.

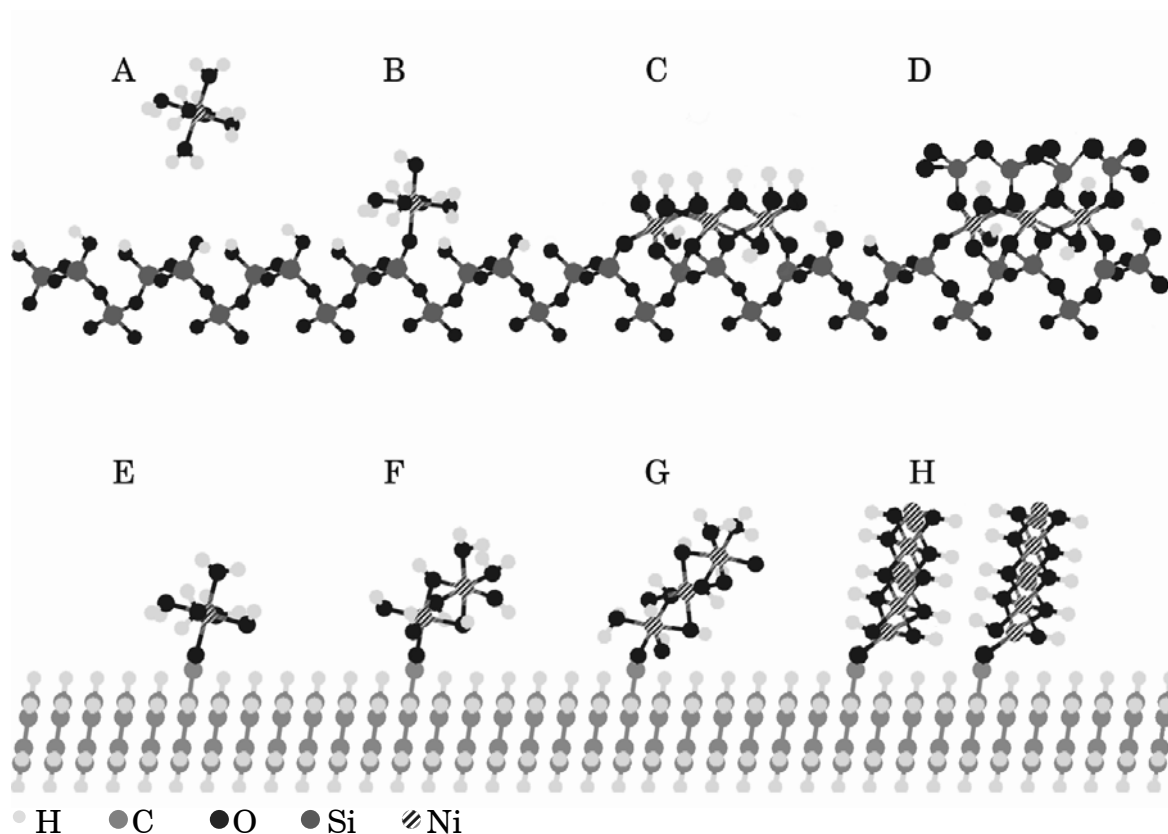


Figure 11: Schematic representation of the mechanism of deposition precipitation of nickel. Top: Nickel deposition precipitation on silica; (A) before nucleation there is no significant interaction between silanol groups and $\text{Ni}(\text{OH}_2)_6^{2+}$; (B) nucleation on silica support at $\text{pH}=5.8$; silanol groups interact with nickel ions, which results in the formation of $\text{Si-O-Ni}(\text{OH})(\text{OH}_2)_4$. (C) Nickel hydroxide is formed at pH of 5.4 and (D) the final nickel phyllosilicates. Bottom: Precipitation on CNF-O (Figure 11E-H). (E) Nickel ion adsorption takes place on carboxyl groups; (G) Nucleation of $\text{Ni}(\text{OH})_2$ at $\text{pH}=5.8$; (H) Growth of $\text{Ni}(\text{OH})_2$ sheets at $\text{pH}=5.7$.

Conclusions

Deposition precipitation of nickel hydroxide onto silica and modified carbon nanofiber support material has been studied by time dependent pH and metal loading studies in combination with characterization of the dried catalyst precursors. With silica the previously studied strong interaction between the deposited nickel hydroxide or nickel phyllosilicate and the support is apparent from the low steady state pH ($\text{pH}=5.4$) at which precipitation takes place. From a study of the extent of nickel deposition onto the silica with time of precipitation it is clearly shown that prior to nucleation of the nickel phase on the support ($\text{pH}=5.8$) no nickel-ion adsorption occurs. From this it is strongly suggested that nickel-ion adsorption coincides with the nucleation phase for the

silica support. For surface-oxidized carbon nanofibers (CNF-O) extensive adsorption occurs right from the start of the deposition precipitation (pH=3.5). At the maximum of the pH curve (pH=5.8) that reveals nucleation of a new phase already 22% of the nickel present has been deposited onto CNF-O in strong contrast with silica. The steady-state pH at which precipitation takes place (pH=5.7) is well above that observed with silica and below that of blank experiments thus pointing to deposition of the nickel hydroxide phase onto the carbon support. Characterization of the dried catalysts shows small platelets (40x5 nm) of nickel hydroxide adhered to the CNF-O. After reduction of the sample at 773 K a 20 wt% Ni/CNF-O sample is obtained with well-dispersed metallic nickel particles of 8 nm on the carbon nanofibers. The oxidized carbon nanofibers contain acidic groups of the carboxylic type. After removal of these groups by either chemical reduction or by thermal treatment, deposition precipitation takes place separate from the support and large nickel hydroxide platelets (> 500 nm) are observed. Acid groups on the modified carbon support are concluded to play a key role in the success of deposition precipitation of nickel hydroxide onto carbon nanofibers.

Acknowledgments

The authors acknowledge C. van der Spek and J.W. Geus for performing the TEM and SEM measurements and the financial support of STW (grant UPC 5487).

References

1. Clause, O., Kermarec, M., Bonneviot, L., Villain, F., Che, M., *J. Am. Chem. Soc.*, (1992), 114, 4709.
2. Che, M., Clause, O., Marcilly, Ch., in “Preparation of Solid Catalysts” (Ertl, G., Knozinger, H., Weitkamp, J., Eds.), Wiley-VCH: Weinheim, (1999), 315.
3. Van Dillen, A.J., Terorde, R.J.A.M., Lensveld, D.J., Geus, J.W., De Jong, K.P., *J. Catal.*, (2003), 216, 257.
4. Lekhal, A., Glasser, B.J., Khinast, J.G., *Chem. Eng. Sci.*, (2004), 59, 1063.
5. Bergwerff, J.A., Visser, T., Leliveld, B.R.G., Rossenaar, B.D., De Jong, K.P., Weckhuysen, B.M., *J. Am. Chem. Soc.*, (2004), 126, 14548.
6. Regalbuto, J.R., Navada, A., Shadid, S., Bricker, M.L., Chen, Q., *J. Catal.*, (1999), 184, 335.
7. Schreier M., Regalbuto, J.R., *J. Catal.*, (2004), 225, 190.
8. Miller, J.T., Schreier, M., Kropf A.J., Regalbuto, J.R., *J. Catal.*, (2004), 225, 203.
9. Lambert, J.-F., Che, M., *J. Mol. Catal. A-Chem.*, (2000), 162, 5.
10. Lambert, J.-F., Hoogland, M., Che, M., *J. Phys. Chem. B.*, (1997), 101, 10347.
11. Marceau, E., Lauron-Pernot, H., Che, M., *J. Catal.*, (2001), 197, 394.
12. Negrier, F., Marceau, E., Che, M., *Chem. Comm.*, (2002), 11, 1194.
13. Carrier, X., Lambert, J. F., Che, M., *J. Am. Chem. Soc.*, (1997), 119, 10137.
14. Louis, C., Cheng, Z. X., Che, M. *J. Phys. Chem.*, (1993), 97, 5703.
15. Hermans, L.A.M., Geus, J.W. *Stud. Surf. Sci. Catal.*, (1979), 3, 113.
16. Che, M., Cheng, Z.X., Louis, C., *J. Am. Chem. Soc.*, (1995), 117, 2008.
17. Geus, J.W., Van Dillen, A.J., in “Preparation of Solid Catalysts” (Ertl, G., Knozinger, H., Weitkamp, J., Eds), Wiley-VCH: Weinheim, (1999), 460.
18. Serp, P., Kalck, P., Feurer, R., *Chem. Rev.*, (2002), 102, 3085.
19. Lashdaf, M., Lahtinen, J., Lindblad, M., Venaelaenen, T., Krause, A.O.I., *Appl. Catal. A-Gen.*, (2004), 276, 129.
20. Campanati, M., Fornasari, G., Vaccart, A., *Catal. Today*, (2003), 77, 299.
21. Schmidt, F., *Appl. Catal. A-Gen.*, (2001), 221, 15.
22. Perego, C., Villa, P.L., *Catal. Today*, (1997), 34, 281.
23. Pernicone, N., *Catal. Today*, (1997), 34, 535.

24. De Jong, K.P., *Curr. Opin. Solid St. M.*, (1999), 4, 55.
25. Beck, J.S., Vartuli, J.C., Roth, W.J., Leonowicz, M.E., Kresge, C.T., Schmitt, K.D., Chu, C.T-W., Olson, D.H., Sheppard, E.W., McCullen, S.B., Higgins, J.B., Schlenker, J.J.L., *J. Am. Chem. Soc.*, (1992), 114, 10834.
26. Zhao, D., Feng, J., Huo, Q., Melosh, N., Fredrickson, G.H., Chmelka, B.F., Stucky, G.D., *Science*, (1998), 279, 548.
27. Kruk, M., Jaroniec, M., Kim, T.-W., Ryoo, R., *Chem. Mat.*, (2003), 15, 2815.
28. Figueiredo, J.L., Pereira, M.F.R., Freitas, M.M.A., J.J.M., *Carbon*, (1999), 37, 1379.
29. Rodríguez-Reinoso, F., *Carbon*, (1998), 36, 159.
30. De Jong, K.P., Geus, J.W., *Catal. Rev.-Sci. Eng.*, (2000), 42, 481.
31. Helveg, S., Lopez-Cartes, C., Sehested, J., Hansen, P.L., Clausen, B.S., Rostrup-Nielsen, J.R., Abild-Pedersen, F., Norskov, J.K., *Nature*, (2004), 427, 426.
32. Planeix, J.M., Coustel, N., Coq, B., Brotons, V., Kumbhar, P.S., Dutartre, R., Geneste, P., Bernier, P., Ajayan, P.M., *J. Am. Chem. Soc.*, (1994), 116, 7935.
33. Iijima, S., *Nature*, (1991), 354, 564.
34. Baker, R.T.K., Laubernds, K., Wootsch, A., Paal, Z., *J. Catal.*, (2000), 193, 165.
35. Salman, F., Park, C., Baker, R.T.K., *Catal. Today*, (1999), 53, 385.
36. Ros, T.G., Van der Lee, M.K., Van Dillen, A.J., Geus, J.W., Koningsberger, D.C., *J. Mol. Catal. A-Chem.*, (2002), 186, 13.
37. Hoogenraad, M.S., Onwezen, M.F., Van Dillen, A.J., Geus, J.W., *Stud. Surf. Sci. Catal.*, (1996), 101, 1331.
38. Hoogenraad, M.S., van Leeuwarden, R.A.G.M.M., Van Breda Vriesman, G.J.B., Broersma, A., Van Dillen, A.J., Geus, J.W., *Stud. Surf. Sci. Catal.*, (1995), 91, 263.
39. Vieira, R., Pham-Huu, C., Keller, N., Ledoux, M.J., *Chem. Comm.*, (2002), 9, 954.
40. Pham-Huu, C., Keller, N., Ehret, G., Charbonniere, L.J., Ziessel, R., Ledoux, M.J., *J. Mol. Catal. A-Chem.*, (2001), 170, 155.
41. Toebes, M.L., Prinsloo, F.F., Bitter, J.H., Van Dillen, J.A., De Jong, K.P., *J. Catal.*, (2003), 214, 78.
42. Bezemer, G.L., Van Laak, A., Van Dillen, A.J., De Jong, K.P., *Stud. Surf. Sci. Catal.*, (2004), 147, 259.
43. Toebes, M.L., Zhang, Y., Hajek, J., Nijhuis, T.A., Bitter, J.H., Van Dillen, A.J., Murzin, D.Y., Koningsberger, D.C., De Jong, K.P., *J. Catal.*, (2004), 226, 215.

44. Serp, P., Corrias, M., Kalck, P., *Appl. Catal. A-Gen.*, (2003), 253, 337.
45. Geus, J.W., Dutch Patent Application, (1967), 6705, 259, and: Dutch Patent Application, (1968), 6813, 236
46. Hermans, L.A.M., Geus, J.W., *Stud. Surf. Sci. Catal.*, (1979), 3, 113.
47. De Roos, G., Fluit, J.M., Hermans, L.A.M., Geus, J.W., *Z. Anorg. Allg. Chem.*, (1979), 449, 115.
48. Van Dillen, A.J., Geus, J.W., Hermans, L.A.M., Van der Meijden, J., *Stud. Surf. Sci. Catal.*, (1977), 2, 677.
49. De Jong, K.P., *Stud. Surf. Sci. Catal.*, (1991), 63, 19.
50. Burattin, P., Che, M., Louis, C., *J. Phys. Chem. B.*, (1997), 101, 7060.
51. Burattin, P., Che, M., Louis, C., *J. Phys. Chem. B.*, (1998), 102, 2722.
52. Burattin, P., Che, M., Louis, C., *J. Phys. Chem. B.*, (1999), 103, 6171.
53. Burattin, P., Che, M., Louis, C., *J. Phys. Chem. B.*, (2000), 104, 10482.
54. Nares, R., Ramirez, J., Gutierrez-Alejandre, A., Louis, C., Klimova, T., *J. Phys. Chem. B.*, (2002), 106, 13287.
55. Wigmans, T., van Doorn, J. and Moulijn, J.A., *Surf. Sci.*, (1983), 135, 532.
56. Prinsloo, F.F., Hauman, D., Slabbert, R., *Carbon'01, An International Conference on Carbon, Lexington, KY, United States*, (2001), 940.
57. Bitter, J.H., Van der Lee, M.K., Slotboom, A.G.T., Van Dillen, A.J., De Jong, K.P., *Catal. Lett.*, (2003), 89, 139.
58. Toebes, M.L., Bitter, J.H., Van Dillen A.J., De Jong, K.P., *Catal. Today*, (2002), 76, 33.
59. Boehm, H.P., *Carbon*, (1994), 32, 759.
60. Boehm, H.P., *Carbon*, (2002), 40, 145.
61. Ros, T.G., Van Dillen, A.J., Geus, J.W., Koningsberger, D.C., *Chem.-Euro. J.*, (2002), 8, 1151.
62. Hoogenraad, M.S., Ph.D. thesis, Utrecht University, the Netherlands, (1995).
63. Toebes, M.L., van Heeswijk, J.M.P., Bitter, J.H., Van Dillen, A.J., De Jong, K.P., *Carbon*, (2004), 42, 307.
64. McCann, G.M., McDonnell, C.M., Magris, L., O'Ferrall, R.A.M., *J. Chem. Soc. Perkin Trans. 2*, (2002), 4, 784.
65. Pines, E., Magnes, B.-Z., Lang, M.J., Fleming, G.R., *Chem. Phys. Lett.*, (1997), 281, 413.
66. Abd El Wahed, M.G., *Acta Chim. Hung.*, (1990), 127, 51.
67. Weller Z., *Elektrochem. Angew. Phys. Chem.*, (1952), 56, 662.
68. Kieffer, R., *C. R. Hebd. Seances Acad. Sci.*, (1954), 238, 700.
69. Boehm, H.P., *Adv. Catal.*, (1966), 16, 179.
70. Plyasunova, N.V., Zhang, Y. Muhammed, M., *Hydrometallurgy*, (1998), 48, 43.

Chapter 4

71. Richens, D.T., *The chemistry of aqua ions*, Wiley-VCH: New York, (1997).

5

Sintering of carbon nanofibers supported nickel catalysts used for methanation

Abstract

Sintering of well-dispersed metallic nickel on carbon nanofibers catalysts was studied under methanation conditions and in CO containing atmospheres. It was found that the kinetics of sintering follows Ostwald ripening in which the rate of sintering is controlled by a 2-D or 3-D diffusion field of $\text{Ni}(\text{CO})_4$. However, thermodynamical validation indicates that the rate of carbonyl formation strongly limits the mean carbonyl concentration, which highly slows down the sinter process.

Introduction

One of the major problems with heterogeneous catalysts is their activity loss with time-on stream. Next to support collapse possible causes for deactivation are poisoning, coking, volatilization and sintering. We will focus on sintering, in particular that of supported nickel catalysts under methanation conditions. Sintering generally refers to surface loss of the active phase per gram of catalyst or per gram of metal, caused by migration of atoms or crystallites of the active metal. In the latter case, also called thermal sintering, particles migrate over the surface, collide and coalesce. Growth of crystallites caused by the loss of atoms from the smaller crystallites is usually referred to as chemical sintering, chemical coarsening or ‘Ostwald ripening’.

A key parameter for sintering is the temperature. With thermal sintering a high mobility of the metal particles is required, generally observed only above the Tammann temperature, i.e. the temperature half of the melting point of the bulk metal, for nickel 863 K. From the literature it is well known that the susceptibility to thermal sintering is next to temperature affected by the gas phase composition [1,2], particle shape and size [3], roughness and pore size distribution of the support [4], the presence of impurities in the support or the metal [5-7], and the nature of the metal-support interaction [3,8,9].

Most studies on sintering of nickel particles concern nickel on oxidic supports [9-22]. To suppress thermal sintering, strong interaction between metal and support is beneficial. For silica-supported nickel catalysts prepared by homogeneous deposition precipitation Coenen et al. found that a strong interaction exists between metal and silica supports as long as an interlayer of hydro-silicate is maintained [23]. This interlayer is the unreduced fraction of the nickel precursor formed during precipitation and drying. Van Stiphout found with Ni/SiO₂ catalysts that sintering via crystallite migration predominated only at temperatures above 673 K, i.e., after reduction of the nickel hydro-silicate interlayer, while sintering at temperatures lower than 573 K predominantly proceeded via nickel carbonyl, Ni(CO)₄ [24].

In view of the methanation conditions we used, we will concentrate on this low temperature sintering. Observations of this type of sintering are reported in literature when nickel catalysts are exposed to CO for example during methanation experiments [25-28]. To prevent the nickel catalysts for sintering Shen et al. reported “safe” methanation conditions, which are based on a maximal permissible nickel carbonyl partial pressure of 10⁻⁶ Pa [25]. These safe operating conditions were sensitive to temperature and CO pressure. Above this partial pressure, at low temperature or high CO pressure, sintering occurs resulting in a bimodal system of small spherical and large faceted crystallites [27-29].

Chemical sintering occurs in 5 steps: the formation at and desorption of $\text{Ni}(\text{CO})_4$ from the nickel particle surface, inter particle carbonyl transport, adsorption and dissociation of $\text{Ni}(\text{CO})_4$ on the surface of the second particle whereby nickel atoms are deposited on [25,29]. Transport of nickel from one particle to another can occur through the gas phase or via the support surface. In the first case a particle grows due to the net flux of $\text{Ni}(\text{CO})_4$ towards the (spherical) particle surface while in the latter case a particle grows by a net 2 dimensional flux of $\text{Ni}(\text{CO})_4$ over the support surface towards its outer contour.

In this work we study the properties of carbon nanofiber supported nickel catalysts under methanation condition. Carbon nanofibers (CNF) are graphite-like materials with a high aspect ratio. They are mechanically strong and do not show microporosity, which makes them suitable as catalyst support [30,31]. First we measured the thermal stability of the nickel dispersion on CNF in hydrogen atmosphere during reduction of differently prepared Ni/CNF catalysts. We will show that the method of catalyst preparation strongly determines the thermal stability of the metal dispersion. Secondly, we studied the sensitivity towards sintering under methanation conditions and in CO atmospheres under dynamic and static conditions for a 10wt% nickel catalyst on surface oxidized CNF. Our approach has been to validate the measured sinter kinetics with thermodynamic calculations.

Theory

The competitive growth of differently sized particles dispersed in a matrix, via so-called Ostwald ripening, has originally been described for changes in particle size of precipitates in a liquid medium. This competitive growth originates from the different concentration gradients around particles of different size [32]. The Gibbs-Thomson relation describes the solubility particle radius dependency for gas-solid systems:

$$c_r = c_e \exp\left[\frac{2\gamma v}{RT} \cdot \frac{1}{r}\right] \approx c_e \left[1 + \frac{2\gamma v}{RT} \cdot \frac{1}{r}\right] \quad (1)$$

in which c_e is the solute concentration at a plane interface ($r = r_\infty$), c_r the solubility at the surface of a particle with radius r , γ the specific gas-solid interfacial energy, v the molar volume, R the gas constant and T the absolute temperature. The assumption made in equation 1, the linear approach, is only realistic if the exponential factor is $\ll 1$. If so, the Gibbs-Thomson relation simplifies to:

$$c_r - c_e = \frac{\alpha}{r} \quad \text{where } \alpha = (2\gamma / RT) v c_e \quad (2)$$

The solute concentration at a surface of a particle with curved interface (r_1) is larger than that at the surface of a particle with plane interface (r_∞) but smaller than that at the surface of a particle with a curved interface (r_2) in case $r_2 < r_1$. This difference in concentration induces a diffusive flux of atoms from the smaller to the larger particles. Due to this process the average particle radius increases, while the total number of particles as well as the total free surface enthalpy decrease. The diffusive flux describing the transport of material is given by Fick's first law:

$$J = -D_{eff} \frac{\partial c}{\partial x} \quad (3)$$

in which D_{eff} is the diffusion coefficient, $\partial c / \partial x$ describes the concentration gradient and x is the distance between particles. Hence, differentiation of the concentration distribution towards x gives the diffusive flux. Furthermore, if the interaction between the particles can be ignored, i.e., if their dimensions are small compared to their mean distance x , the flux J of solute passing the particle boundary per unit area is given by (3) resulting in a change in volume for particle 1:

$$dV_1 = JA_{old} v dt \quad (4)$$

in which A_{old} is the surface area of nickel particle 1 before growth. The transport of matter results in a decrease in volume of particle smaller than particle 1 which is equal to the increase in volume of particle 1. So the volume of particle 1_{new} equals the sum of V_{old} and the dV_1 . If the particles shape is half spherical, the radii of the particle can be calculated.

$$r_{new} = \sqrt[3]{\frac{3(V_{old} + dV_1)}{2\pi}} \quad (5)$$

The radius at which there is no growth or shrinkage is defined as the critical radius r_c with $r_c = \alpha/\Delta$, wherein Δ , is the super saturation ($c_r - c_e$). If $r < r_c$ the particle shrinks, whereas a particle with radius $r > r_c$ will grow.

The average particle growth rate, which is the change in average particle size over the catalyst per unit of time, can then be calculated according equation 6:

$$\frac{d\bar{r}}{dt} = \frac{(\bar{r}_t - \bar{r}_{t=0})}{(t - t_0)} = \frac{(\bar{r}_{1new} - \bar{r}_{t=0})}{dt} \quad (6)$$

To elucidate whether deactivation of our Ni/CNF catalyst is due to thermal or due to chemical sintering we join the widely adopted phenomenological approach of Lifshitz, Slyosov and Wagner (LSW) who derived

for Ostwald ripening the asymptotic kinetic law [33,34], based on steady state conditions of the diffusive flux and a time-invariant volume fraction during sintering. This approach has been used and extended, for example, by Chakraverty, who applied the concepts of LSW to clusters on surfaces [35]. Ardell [36] concentrated on the influence of the dimensionalities of both the dispersed particles (d) and the diffusion field (D). For the rate of growth of the mean particle radius $\bar{r}(t)$ he formulated the relation:

$$\bar{r}(t) = kt^n \quad (7)$$

in which the exponent n is given by the integer values for these dimensionalities d respectively D :

$$n = \frac{1}{3+d-D}; D \leq d \quad (8)$$

In Table 1 a survey is given for a limited number of combinations of d and D . Depending on the dimensionality of the diffusion field for chemical sintering we must expect values of n ranging from 1/3 to 1/4. Lower values for n in the order of 1/10 indicate thermal sintering [36].

Table 1: Values of n for relevant dimensionalities of the dispersed particles d and the diffusion field D [36].

d	D	n
3	3	1/3
3	2	1/4
2	2	1/3

Experimental

Preparation of the CNF supports

A 20 wt% Ni/SiO₂ catalyst was prepared by deposition precipitation (DP) as described by Van Dillen et al. [37] using silica (Degussa, Aerosil 200), nickel nitrate (Acros) and urea (Acros). After filtering and drying at 393 K the catalyst precursor was calcined in static air at 873 K. Prior to the carbon nanofiber growth 1 g of the precursor, sieve fraction 425 – 850 μm, was placed in a quartz fixed bed reactor and reduced in situ for 2 h in a flow of a mixture of H₂ (80 ml/min) and N₂ (320 ml/min) at 1 bar and at 973 K (heating rate 5 K/min). Next, the fibers were grown at 823 K in a mixture of CO (120 ml/min), H₂ (42 ml/min) and N₂ (238 ml/min) for 24 h. The product was refluxed for 2 h in 200 ml of a 1 M KOH aqueous solution to remove the silica support. Next, after filtering and thoroughly washing with de-ionised water, part of the fibers were treated for 0.5 h in a refluxing mixture of 1:1 v/v H₂SO₄: HNO₃ to remove exposed nickel and to introduce oxygen containing surface groups [38]. The fiber support thus prepared is further denoted as CNF-ox. Another part of the fibers was, after the treatment in KOH, refluxed in concentrated HCl, which means that only exposed nickel was dissolved but no oxygen containing surface groups were introduced. These fibers are further denoted as CNF-as.

Preparation of 10 wt% Ni/CNF catalysts

Incipient wetness impregnation was preceded by evacuation of the support materials, CNF-as and CNF-ox. For CNF-as a solution of Ni(NO₃)₂.6H₂O (Acros) in ethanol (0.688 g/ml) was used to impregnate 2.5 g of fibers. For 2.5 g CNF-ox a solution of this nickel salt in water was applied. Since the pore volume was measured to be 1 ml/g, 2.5 ml solution was added drop wise under static vacuum. Solvent evaporation and drying was carried out at 393 K for 18 hours. These catalysts are further encoded as Ni/CNF-as and Ni/CNF-ox.

Nickel deposition by deposition precipitation (DP) was executed according to the procedure we described earlier [39]. In a suspension of 1.5 g CNF-ox in 200 ml de-ionised water 0.8 g of Ni(NO₃)₂.6H₂O (Acros) was dissolved. After adjustment with diluted nitric acid of the pH at a value of about 3 the temperature was brought at 363 K and an aqueous solution (10 ml) containing 0.6 g urea was added. During the precipitation the temperature was kept at 363 K. After 18 hours and subsequent cooling to room temperature the loaded carbon nanofibers were thoroughly washed with de-ionised water and dried at 393 K for 18 hours (Ni-DP/CNF-ox).

Methanation and sintering

Methanation experiments were done in a plug-flow reactor with a diameter of 1 cm at 1.20 bar total pressure. The total gas flow passed down-flow through the reactor and amounted to 100 ml/min. Gas flows of CO, H₂ and N₂ were controlled via mass flow controllers and a backpressure controller to set the total pressure in the setup at 1.20 bar. A tubular oven was placed around the reactor to control the process temperature. During methanation samples of the gas stream were analyzed by a gas chromatograph. Both the flame ionization detector (FID) and the thermal conductivity detector (TCD) were calibrated prior to the measurements.

The reactor was loaded with 250 mg Ni/CNF catalyst, where it was reduced in a flow of 20 vol% H₂ and 80 vol% N₂ (total flow = 100 ml/min) at 573 K to obtain the methanation catalyst. Next, the catalyst was fed at 673 K with a syngas mixture of 1 vol% CO and 3 vol% H₂, total flow 100 ml/min at 1.20 bar. The temperature was decreased with 60 K/h to 453 K and kept at this value for 20 minutes. Finally, the temperature was increased again (60 K/h) to 673 K. With an interval of 30 minutes the gas composition was determined with the gas chromatograph.

For both static and dynamic sintering experiments the same methanation setup was used, however, gases from the reactor were not analyzed by gas chromatograph. For the static sinter experiments the valves on the quartz reactor were closed. First the CO-rich gas was led through the reactor for 4 minutes at 1.20 bar to be sure that the reactor and catalyst were totally filled with gases of the desired composition. After this time the valves on the reactor were closed simultaneously.

Sintering experiments under static conditions were executed for 6, 16, 24, 48 and 96 hours. The reactor was loaded with 200 mg Ni/CNF-ox where it was reduced at 573 K and next was subjected to 4 or 20 vol% CO in N₂ atmosphere at 423 K. Dynamic sintering experiments were done for 24 and 48 hours also in 4 and 20 vol% CO atmosphere with a total gas flow of 100 ml/min. After the indicated periods of time the reactor with the nickel catalyst was flushed with N₂ before the reactor was cooled down to room temperature.

Characterization

Characterization of the samples was done using X-ray diffraction (XRD), Transmission Electron Microscopy (TEM), Temperature Programmed Reduction (TPR) and Thermal gravimetric analysis (TGA). XRD patterns were recorded at room temperature with an Enraf Nonius PDF 120 powder diffractometer system equipped with a position-sensitive detector with a 2θ

range of 120° using Co $K\alpha_1$ ($\lambda = 1.78897 \text{ \AA}$) radiation. For the determination of the average metal particle size the Debye-Scherrer equation was applied.

TEM images were obtained using a Philips CM-200 FEG operated at 200 kV. Samples were, after ultrasonic treatment in ethanol, dispersed on a holey carbon film on a copper grid. To establish the average nickel particle size diameters at least 200 different particles distributed over 5 to 10 different TEM images were measured using Analysis Pro (3.2) soft-imaging system software.

TGA was used to determine the nickel content of the samples. To this end the rest-weight (NiO) was taken after heating a sample in a flow of 5 vol% oxygen in argon up to 1273 K.

TPR analyses were done using a Micromeritics Autochem II 2920 apparatus equipped with a TCD detector. During measurements 5 vol% H_2 in argon was passed through the samples with a flow of 50 ml/min. Prior to reduction the samples were dried at 393 K. H_2 consumption profiles were measured from 300 K to 973 K, heating rate 5 K/min.

Thermodynamic calculations

For calculations of the thermodynamic equilibrium compositions for the methanation reaction and the partial pressure of nickel carbonyl as function of the process temperature the computer program “HSC-4 chemistry for windows” was used [40]. Hereby the pressure was set to be constant at 1.20 bar while the temperature increases.

Results and discussion

Thermal sintering

The hydrogen-reduction of dried Ni/CNF catalysts was studied by TPR. Roughly three regions can be recognized in the TPR patterns as shown in Figure 1, the first one up to 580 K, the second one up to around 740 K and the third one up to the final temperature of the measurements at 973 K. In the first region samples prepared by impregnation start to consume hydrogen from 470 K and show a peak around 550 K. Reduction of Ni-DP/CNF-ox already starts at 400 K, but a peak at 550 K is lacking; only a shoulder is recognizable around 580 K. This difference between the impregnated samples and the DP sample is related to the presence of nitrate. After drying the impregnated carbon nanofibers, substantial amounts of nitrate remain that are reduced at ~ 550 K, probably next to part of the nickel (II). The shoulder at 580 K for the Ni-DP/CNF-ox sample may also originate from nitrate localized between the sheets of turbostratic α -Ni(OH) $_2$ which is formed during precipitation [41]. In the

second region (550 – 740 K) the bulk of the nickel (II) amount is reduced, the amount of hydrogen consumption depending on the degree of reduction already attained in region 1. In the third region, above 740 K, the interaction of the formed metallic nickel particles with the support determines the temperature at which gasification of the CNF support starts [39,42].

In Figure 2 TEM images are shown of the three differently prepared catalyst precursor samples after reduction at 573 K and 773 K. In Table 2 the respective average nickel particle sizes derived from TEM images are represented. The differences between the samples after reduction at 573 K turned out to be relatively small: 7 nm for Ni-DP/CNF-ox, 6 nm for Ni/CNF-as and 6 nm for Ni/CNF-ox. The latter was also treated in H₂ for 24 h, which resulted in 6 nm particles too. The particle size distributions after reduction at 573 K are narrow in all cases.

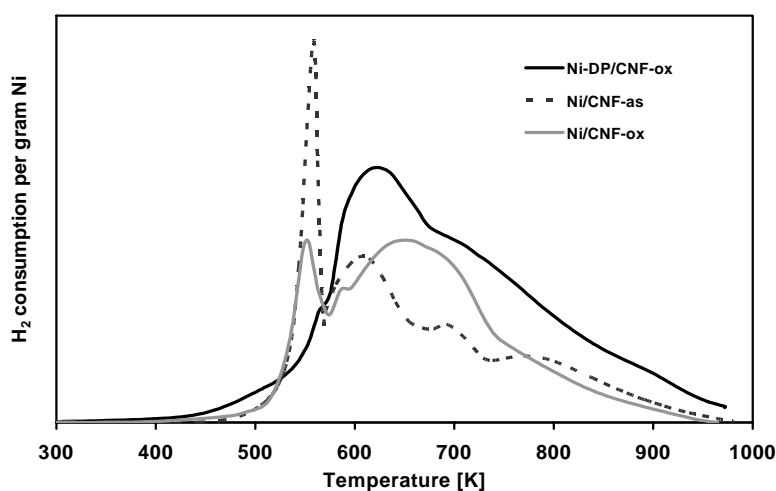


Figure 1: TPR profiles of nickel loaded carbon nanofibers. Hydrogen consumption is scaled on 1 gram nickel.

Table 2: Average nickel particle size after reduction at 573 and 773 K for 1 hour.

Ni catalyst	Average Ni d _p [nm]	Average Ni d _p [nm]
	Reduction 573 K	Reduction 773 K
Ni/CNF-as	6	27
Ni/CNF-ox	6	10
Ni-DP/CNF-ox	7	9

Upon reduction at 773 K the average diameter of the nickel particles of Ni-DP/CNF-ox catalyst increased from 7 to 9 nm, while that of the Ni/CNF-ox precursor increased from 6 to 10 nm. The growth of the average nickel particle diameter in the Ni/CNF-as catalyst was more significant, i.e., from 6 to 27 nm. Although sintering of the nickel phase for all catalysts was limited at 573 K, to our judgement lack of metal-support interaction makes Ni/CNF-as less thermally stable. With this catalyst the amount of surface oxygen groups obviously is too low to provide stabilisation of the nickel metal particles [38].

Methanation experiments

We tested the Ni/CNF-ox catalyst in the methanation reaction between 423 K and 673 K. In Figure 3 the composition of the product gas stream is given. From this figure it may be concluded that the conversion measured upon decreasing the temperature from 673 K to 453 K coincides within the experimental error with that measured upon increasing the temperature. At temperatures below 550 K only methane is formed. Above this temperature CO₂ is found in the product gas too. There is an optimum in the CH₄ production around 633 K caused by the thermodynamic equilibrium of the methanation reaction at high temperatures. In Figure 3 the calculated equilibrium amount of methane is also plotted as function of temperature (CH₄_{eq}), which shows the same trend above 650 K as the measured curve. The average molar carbon-balance calculated as C_{in}/C_{out} over the whole temperature range turned out to be 1.03 ± 0.05 .

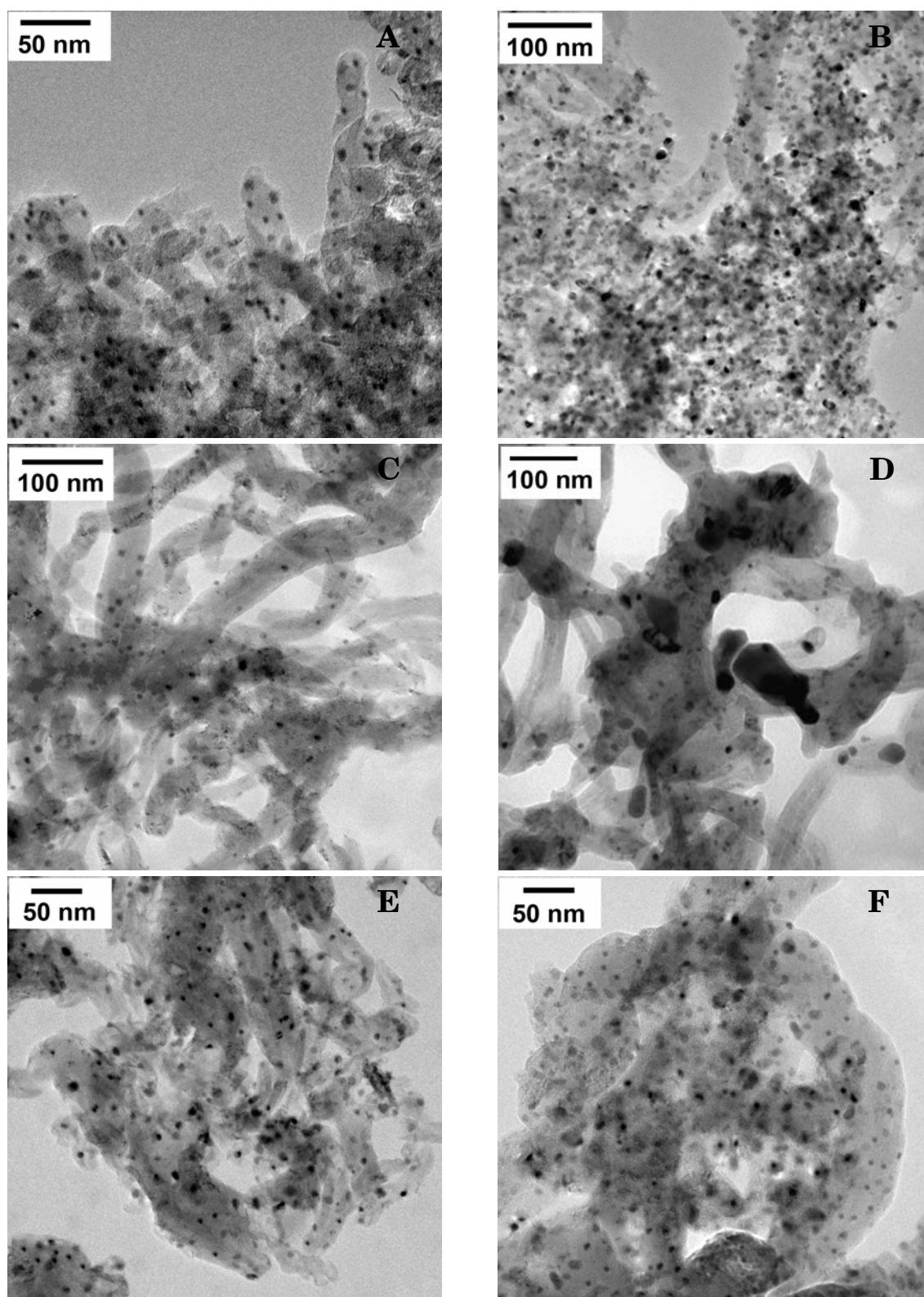


Figure 2: TEM images (A) and (B) show Ni-DP/CNF-ox, (A) reduced at 573 K and (B) at 773 K. (C) and (D) are images of Ni/CNF-as, (C) reduced at 573 K and (D) at 773 K. (E) and (F) are images of Ni/CNF-ox, (E) reduced at 573 K and (F) at 773 K.

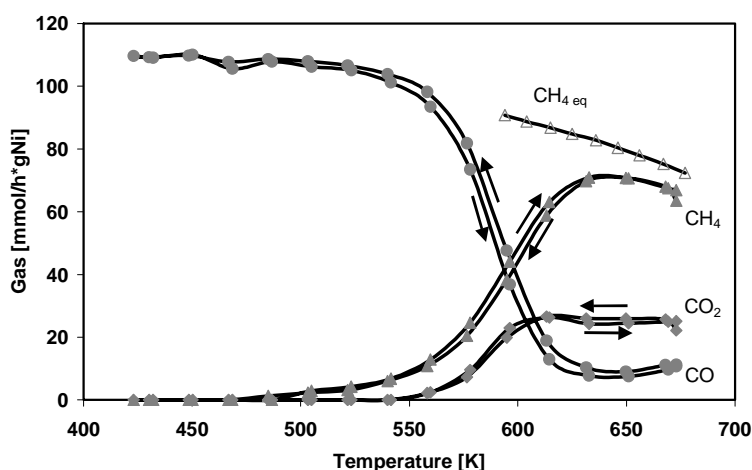


Figure 3: Products and reactants flows during methanation of H_2 :CO (3:1 v/v) over the Ni/CNF-ox catalyst and the thermodynamic equilibrium amount of methane as function of the process temperature.

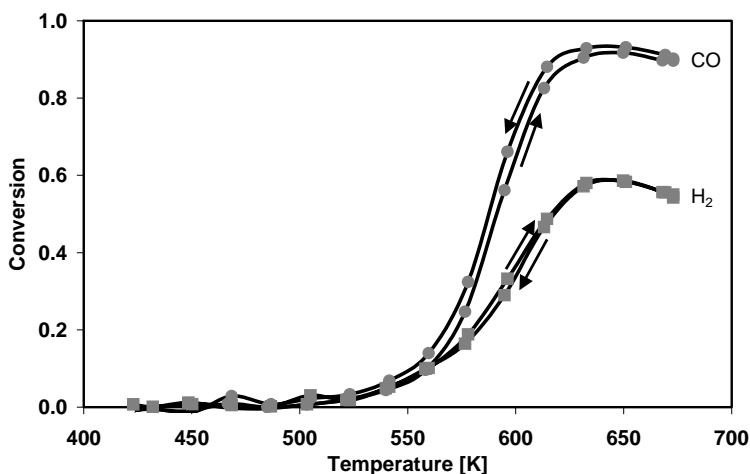
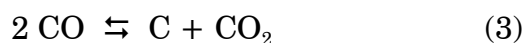
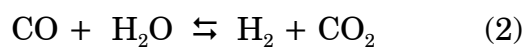


Figure 4: CO and H_2 conversion with Ni/CNF-ox as function of the methanation temperature.

In Figure 4 the derived conversion of CO and H_2 are given as function of the methanation temperature. Above about 550 K the conversion of CO exceeds that of hydrogen; however, the CO and H_2 are fed stoichiometrically according to reaction (1). CO_2 formed above 550 K could originate from two different reactions: the water-gas shift and/or the Boudouard reaction, reactions (2) and (3) respectively.



If only the water-gas shift reaction (2) would be involved, hydrogen should be produced in amounts equal to that of CO₂ and the apparent H₂ conversion should be lower than that of CO. Correction of the CO conversion with respect to the water-gas shift reaction leads to similar conversion levels for CO and H₂ over the whole methanation temperature range. Furthermore it is unlikely that the Boudouard reaction is responsible for (part of) the CO₂ production. In the first place over the whole temperature range the carbon balance within the experimental error is very close to unity, which excludes deposition of excessive amounts of carbon. In the second place, if carbon, even if only in small amounts, would be deposited on the nickel phase, the catalyst should deactivate. From the coinciding curves, see Figure 3, measured while decreasing and, next, increasing the temperature it may be concluded that deactivation does not occur and that CO₂ production must exclusively be due to the water-gas shift reaction.

Results of above measurements demonstrate that under the chosen reaction conditions between 500 K, the lowest temperature at which the presence of methane is measured in the product gas, and 550 K methane is selectively formed.

Methanation experiments with Ni/CNF-ox were executed at 523 K in a syngas mixture of 10 vol% CO and 30 vol% H₂. In the given reaction mixture (10 ml/min CO, 30 ml/min H₂, 60 ml/min N₂) we observed severe deactivation as shown in Figure 5. As we measured with XRD line broadening this activity drop could not be caused by a decreased nickel surface due to sintering only. After 90 h an increase of the average particle size from 4 nm to 6 nm was measured. This could have resulted in a conversion decrease with only a factor 1.7 due to loss of active surface. A possible additional explanation might be the decrease in surface specific activity. From literature it is well known that in methanation the specific activity in terms of turn over number (TON) or frequency (TOF) of a nickel catalyst depends on the types of exposed crystal planes [43,44] and with this on the crystal size and shape.

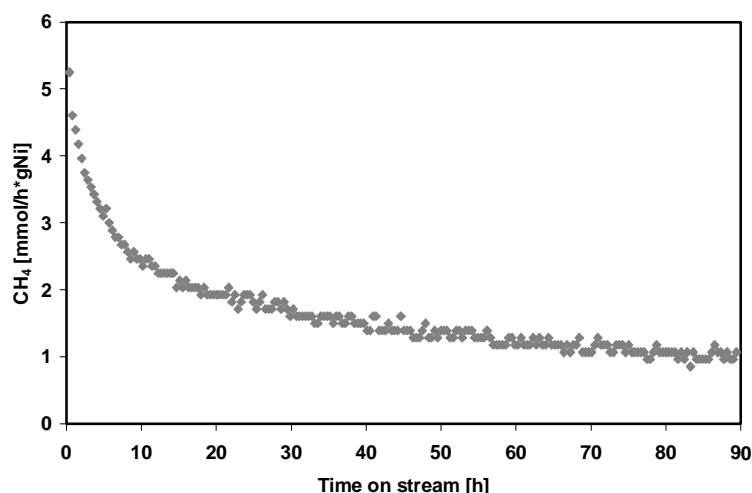


Figure 5: Methanation activity during 90 hours time on stream for Ni/CNF-ox at 523 K, H₂:CO (3:1 v/v) and GHSV_{CO}=2000 L/(L*h).

Chemical sintering

Although sintering under methanation conditions is significant, in view of our aim to reveal the mechanism of sintering the shift in average particle size is too small to expect results with sufficient accuracy within this period of 90 hours. More severe sintering conditions can be established by lowering the temperature and the CO content. This lower temperature and higher CO partial pressure will result in a higher partial pressure of nickel carbonyl. In Figure 6 the equilibrium composition of the Ni-CO system containing 0.34 mmol Ni; 0.11 mmol CO and 0.46 mmol Ar is given as function of temperature.

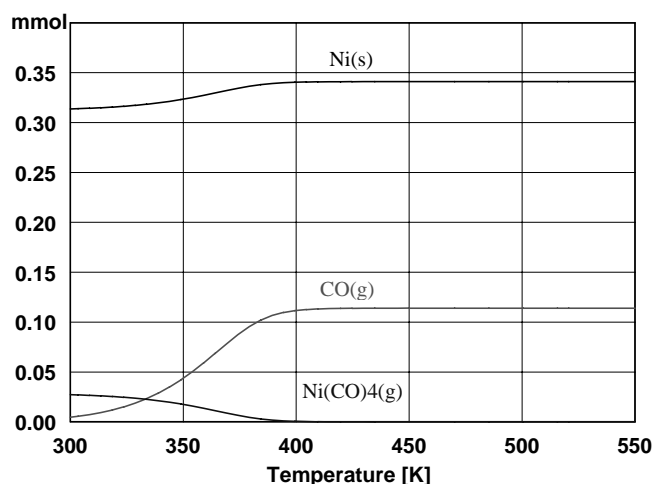


Figure 6: Equilibration compositions as function of the temperature for nickel carbonyl formation: $4 \text{ CO} + \text{Ni} \rightleftharpoons \text{Ni}(\text{CO})_4$. Calculation based on the amounts in static sinter experiments: 0.34 mmol Ni, 0.11 mmol CO and 0.46 mmol Ar.

Dynamic sinter experiments in which the freshly reduced catalyst was exposed to a 4 vol% and a 20 vol% CO containing gas flow (100 ml/min), were executed for 24 hours. From XRD line broadening it was found that in the 4 vol% CO flow the average Ni particle size had increased from 5 nm to 10 nm in 24 hours. In the 20 vol% flow this increase in 24 hours was larger, i.e., from 5 nm to 23 nm. TEM images of used samples clearly reflect the changes taking place during the sinter experiments, see Figure 7. After 48 hours of dynamic sintering the results were even more pronounced. In this latter case we verified the nickel loading using TGA measurements to reveal to what extent nickel was lost during the dynamic sinter experiment. Within the experimental error ($\sim 1\%$) no significant nickel loss was found. From the above results we conclude that because sintering occurred without measurable loss of Ni the rate of decomposition of $\text{Ni}(\text{CO})_4$ is sufficient and does not affect the rate of sintering.

For our study on the sinter mechanism one of the pre-requisites to apply theory was the time-invariant volume fraction of the system. First we focus on static sinter experiments. After the indicated periods of time (6, 16, 24, 48 and 96 h), numerous TEM images were taken and from these the numerical average nickel particle sizes were calculated by careful measuring the radii of the particles. Representative TEM images are shown in Figure 8. An important observation is that the small particles (6-13 nm) are spherical, while larger particles at least those larger than 50 nm expose faceted surfaces.

In Figure 9 the particle size distributions are given of the fresh catalyst after reduction and these after 6, 12, 16, 24, 28 and 96 hour of sintering. The found average nickel particle sizes as collected in Table 3 and plotted in Figure 10 as a function of sinter time clearly demonstrate that the degree of sintering nicely develops with time. A linear trend line is added with a slope of 0.31 ± 0.06 .

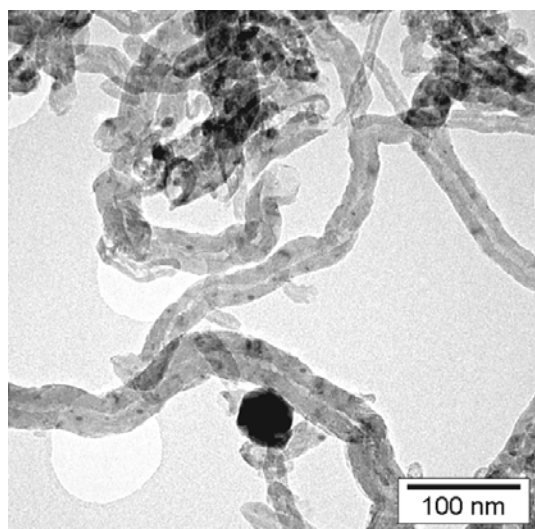


Figure 7: TEM image of Ni/ CNF-ox after 24 hours of dynamic sintering in 20 vol% CO.

Table 3: Average nickel particle radii of Ni/CNF-ox after static sintering, calculated from TEM images.

Sinter time [h]	Average radii \bar{r}_{TEM} [nm]	\bar{r} / \bar{r}_0	$\ln(t)$	$\ln(\bar{r} / \bar{r}_0)$
0	2.5	1.00		0.00
6	3.2	1.26	1.79	0.23
16	4.9	1.93	2.77	0.66
24	5.3	2.09	3.18	0.74
48	6.6	2.62	3.87	0.96
96	7.5	2.96	4.56	1.08

From XRD analyses of fresh and sintered Ni/CNF-ox samples the dimension of particle growth is deduced. Figure 11 shows the diffraction patterns of the nickel catalyst after 0, 6, 16 and 96 hours of static sintering. The diffraction patterns are corrected for the carbon contributions by subtracting the XRD signal of bare carbon nanofibers from that of the loaded materials. The 3-D growth of the nickel particles is demonstrated by the increasing signal intensities and decreasing line widths with sinter time, which holds for all indicated (hkl) reflections of nickel (111), (200), (220) and (311).

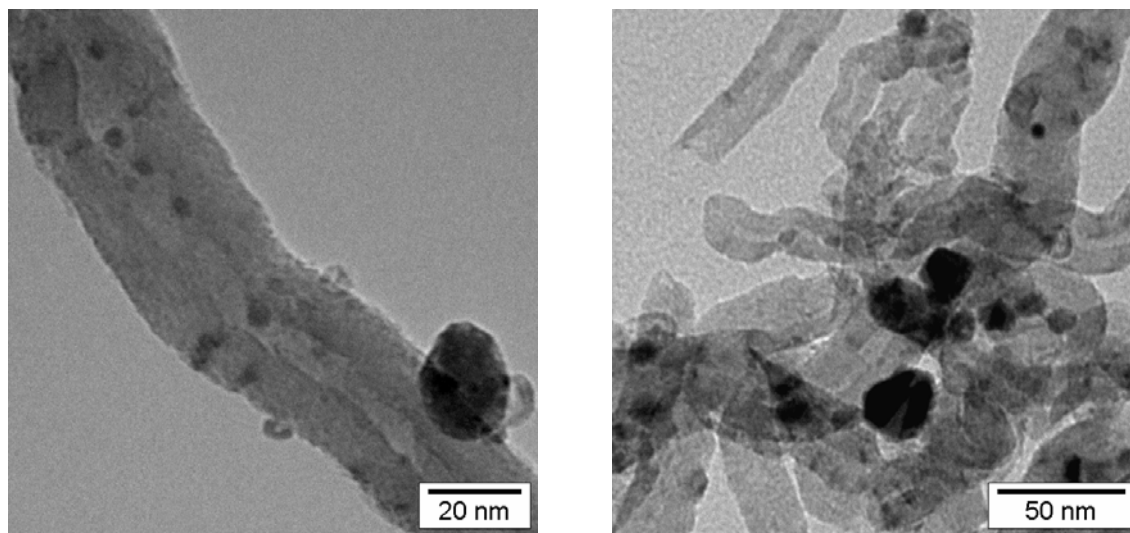


Figure 8: TEM images of nickel on Ni/CNF-ox after reduction at 573 K and static sintering in 20 vol% CO for left 16 hours and right 48 hours.

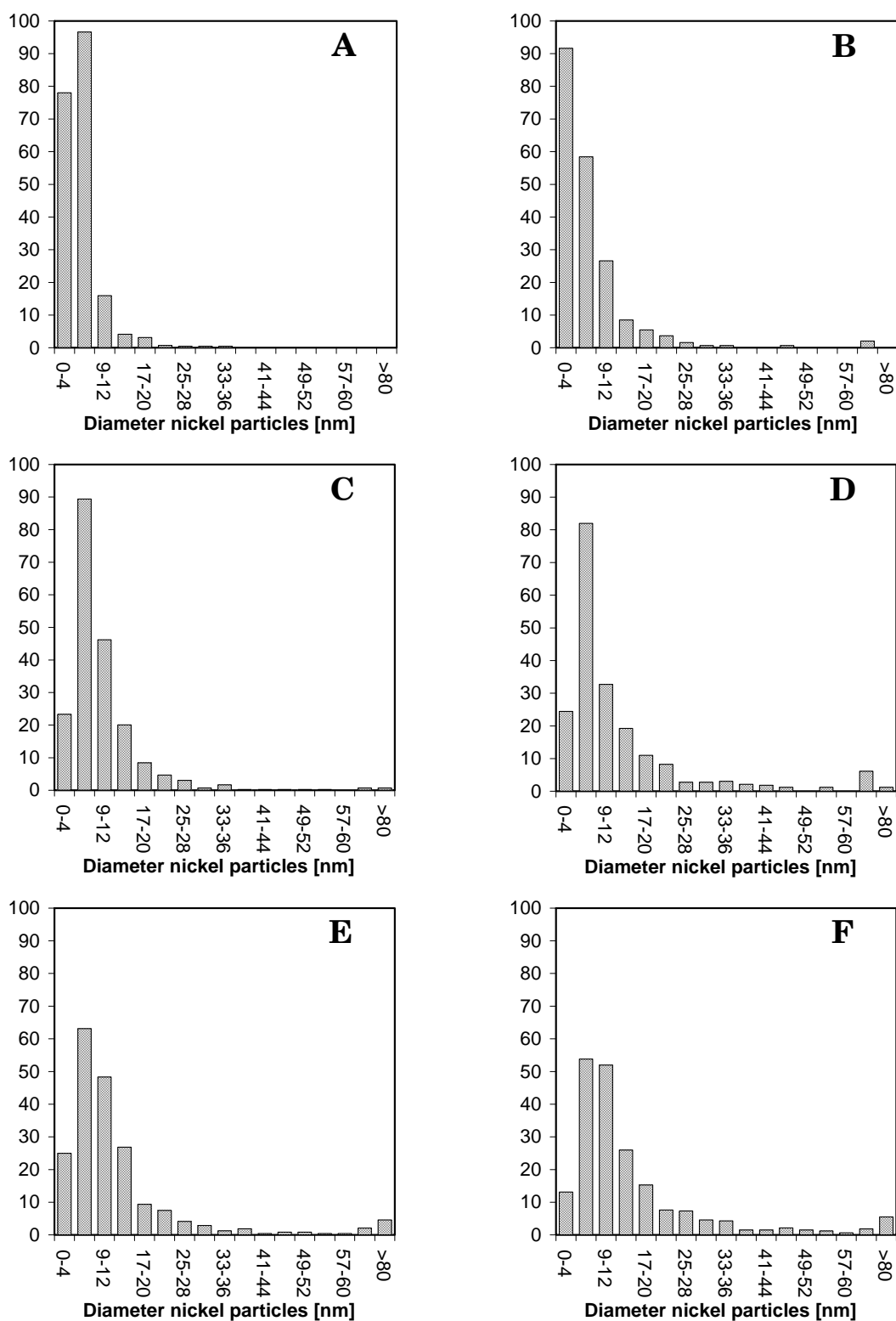


Figure 9: Particle size distribution of Ni/CNF-ox after reduction at 573 K in hydrogen and static sintering at 423 K in 20 vol% CO; (A) fresh reduced catalyst 0h sintering, (B) 6 h, (C) 12 h, (D) 16 h, (E) 48 h and (F) after 96 h sintering.

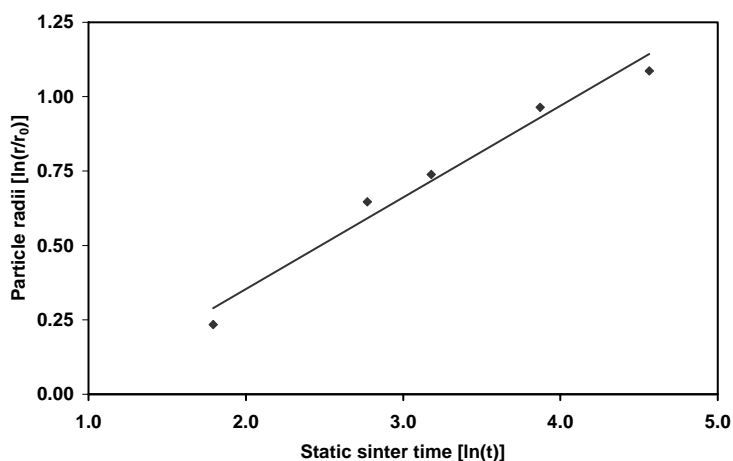


Figure 10: Particle radii $[\ln(r/r_0)]$ as function of $[\ln(t)]$ for Ni/CNF-ox during static sintering.

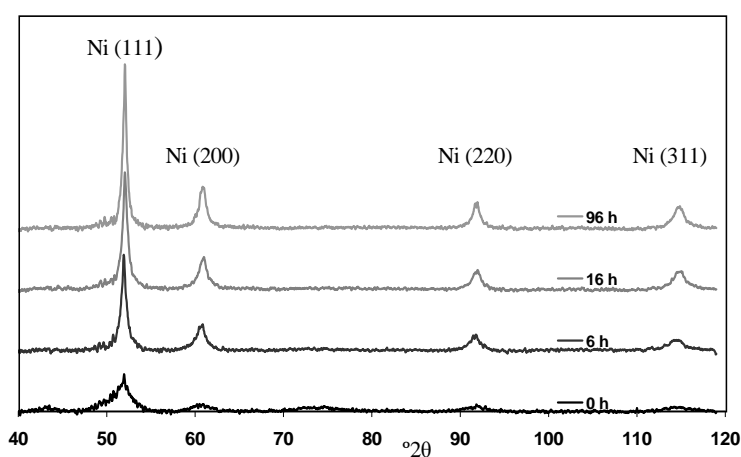


Figure 11: XRD pattern of Ni/CNF-ox after 0, 6, 16 and 96 hours static sintering. Carbon nanofiber contributions are subtracted from the XRD patterns.

As explained in the introduction from the slope of the $\ln(r/r_0)$ versus $\ln(t)$ plot the mechanism of sintering can be discussed. Above results demonstrate that sintering occurs via an Ostwald-like mechanism. Although the dimensionality of growth of the particles (d) obviously is 3, the dimensionality (D) of the diffusion field remains unclear. With a slope of 0.31 ± 0.06 , D could be 2 or 3.

It has to be admitted that thermodynamic validation of the observed sinter process using the Gibbs-Thomson relation is a daring challenge, not in the last place because of lack of reliable quantities for parameters and constants describing the various steps in the overall process. Therefore, in a number of cases, we had to make estimations. In Table 4 most of the constants and parameters used with their interrelation are collected.

From the average nickel particle sizes measured with TEM we calculated the nickel particle radius growth rate (rate_{obs}) as shown in Table 5. In case sintering obeys Ostwald kinetics the rate of sintering occurs due to concentration gradients of carbonyl between Ni particles of different size. In the thermodynamical approach the nickel carbonyl flux between the particles can be found by Fick's first law, (equation 3), i.e., by the diffusion coefficient times the concentration gradient. From the TEM results we estimated the mean particle distance to be 50 nm. Using the "HSC-4" program a value for c_e of $2.7 \cdot 10^{-3} \text{ mol/m}^3$ was calculated. The difference in concentration over this distance between two particles of different size we derived using the Gibbs-Thomson relation.

For transport of nickel carbonyl via the gas phase, the diffusion coefficient (D_g) we took equal to that for an ideal gas in a porous medium, being about $10^{-6} \text{ m}^2/\text{s}$. For transport over the surface estimation of the diffusion coefficient was more difficult. With a commonly used value for D_0 of $4 \cdot 10^{-10} \text{ m}^2/\text{s}$ as given by Carman et al. [46], combined with an activation energy for diffusion over carbon of 14.2 kJ/mol [46], a value measured for CCl_2F_2 being a similarly electron rich compound as $\text{Ni}(\text{CO})_4$, a surface diffusion coefficient (D_s) of $7 \cdot 10^{-12} \text{ m}^2/\text{s}$ could be calculated.

For transport via the support surface the concentration of nickel carbonyl is calculated via equation 1, next the partial pressure of nickel carbonyl around nickel particles is calculated in equilibrium with the coverage of nickel carbonyl on the surface of the carbon nanofibers. This coverage (c_{rs}) we calculated by multiplying time of adsorption (τ_0) with the number of molecules impinging upon the surface per second per square centimeter [45]. Difference in c_{rs} values around small and large nickel particles is the driving force for flux of matter, which we calculated using equation 3. Just like the calculations for 3-D transport this surface flux results in a change of volume. The new radius of the particles we calculated according to equations 4 and 5. The change in average radii during a set period of time was calculated using equation 6. These calculations resulted in calculated growth rates (dr/dt) of $\sim 10^{-11} \text{ m/s}$ for both 3-D and for 2-D diffusion, which is a factor ~ 1000 higher than the rates observed ($\sim 10^{-14} \text{ m/s}$), see table 5.

Table 4: Parameters and constants used for calculations.

Diffusion coefficient in pores	$D_g = 1 \cdot 10^{-6} \text{ m}^2/\text{s}$	
Diffusion coefficient over surface	$D_s = D_0 e^{-E_{act}/RT}$ [45]	$D_s = 7 \cdot 10^{-12} \text{ m}^2/\text{s}$
	$D_0 = 4 \cdot 10^{-10} \text{ m}^2/\text{s}$ [46]	
Activation energy for surface diffusion	$E_{act} = 14.2 \text{ kJ/mol}$ [46]	
	$R = 8.314 \text{ J/mol K}$ [47]	
	$T = 423 \text{ K}$	
Conc. $\text{Ni}(\text{CO})_4$ above flat Ni surface	$c_e = 2.7 \cdot 10^{-3} \text{ mol/m}^3$	
Specific interphacial surface energy (s-g)	$\gamma = 1.8 \text{ J/m}^2$ [47]	
Molar volume Ni (s)	$v = 6.6 \cdot 10^{-6} \text{ m}^3/\text{mol}$ [47]	
Time of adsorption	$\tau = \tau_0 e^{E_{ab}/RT}$ [45]	$\tau = 4.9 \cdot 10^{-5} \text{ s}$
	$\tau_0 = 5 \cdot 10^{-14} \text{ s}$ [45]	
Adsorption energy $\text{Ni}(\text{CO})_4$ on carbon	$E_{ab} = 72.8 \text{ kJ/mol}$ [48]	
Surface concentration around particle with radius r	$c_{rs} = n \tau$ [45]	
Number of molecules striking surface	$n = P_{\text{Ni}(\text{CO})_4} / (2\pi MRT)^{1/2}$ mol/m ² [45]	
Volume of reactor	$V_{\text{reactor}} = 16.71 \cdot 10^{-6} \text{ m}^3$	

Table 5: Average Ni particle radii of Ni/CNF-ox after static sintering and particle growth rate_{obs} and rate_{calc} based on Gibbs Thomson and Fick's law.

Ni radii r_{TEM} [m]	Sinter time [s]	rate_{obs} dr/dt [m/s]	Gas phase transport rate _{calc} [m/s]	Surface transport rate _{calc} [m/s]
$2.5 \cdot 10^{-9}$	0			
		$3.1 \cdot 10^{-14}$	$4.5 \cdot 10^{-11}$	$4.6 \cdot 10^{-11}$
$3.2 \cdot 10^{-9}$	21600			
		$4.7 \cdot 10^{-14}$	$3.3 \cdot 10^{-11}$	$3.7 \cdot 10^{-11}$
$4.9 \cdot 10^{-9}$	57600			
		$1.4 \cdot 10^{-14}$	$2.3 \cdot 10^{-11}$	$2.8 \cdot 10^{-11}$
$5.3 \cdot 10^{-9}$	86400			
		$1.6 \cdot 10^{-14}$	$1.5 \cdot 10^{-11}$	$1.5 \cdot 10^{-11}$
$6.6 \cdot 10^{-9}$	172800			
		$4.9 \cdot 10^{-14}$	$7.8 \cdot 10^{-12}$	$7.4 \cdot 10^{-12}$
$7.5 \cdot 10^{-9}$	345600			

How can we explain this difference between the observed and the calculated rates? Answer to this question could be found in the fact that in our calculations we have used the equilibrium concentration (c_e) for $\text{Ni}(\text{CO})_4$ i.e., $2.7 \cdot 10^{-3} \text{ mol/m}^3$. Only when it is assumed that the actual pressure is much lower we can approach growth rates similar to those observed. From our dynamic sinter experiments we concluded that within the catalyst bed a concentration must have existed during the process much lower than the calculated one. After 48 hours of dynamic sintering and about 0.29 m^3 gas had passed through the nickel catalyst causing a maximal nickel loss of at most 1 wt% ($1.7 \cdot 10^{-6} \text{ mol Ni}$) was indicated. From this amount a maximal mean nickel carbonyl concentration of $5.9 \cdot 10^{-6} \text{ mol/m}^3$ can be calculated. This concentration is at least 1000 times smaller than the concentration (c_e) calculated with the HSC-4 program.

That the actual concentration is much lower than the calculated concentration could be due to the fact that the formation of nickel carbonyl is slow and might be the rate-determining step of the sinter process. That the carbonyl formation is a process indeed has earlier been demonstrated by, e.g., Mazurek et al. and Trivin et al., who showed that the high initial rate of carbonyl formation steeply drops and reaches steady state value much below that predicted by thermodynamics [49,50].

The proposition that the carbonyl formation rate is the rate-determining step in the overall sinter process has to be combined with sintering that follows Ostwald kinetics, however, at a steady state carbonyl concentration much lower than the equilibrium concentration, due to an extremely low rate of carbonyl formation in combination with a high rate of carbonyl decomposition. Ostwald kinetics implies now that the rate of formation of nickel carbonyl is a function of particle size similar to equation 1. Taking a value for the calculated steady state concentration of $5.9 \cdot 10^{-6}$, the value we derived from our dynamic sinter experiments, instead of c_e ($2.7 \cdot 10^{-3} \text{ mol/m}^3$) we find a growth rate of $\sim 10^{-12} \text{ m/s}$. To bring the calculated growth rates in accordance with the observed growth rate the actual concentration should have been in the order of 10^{-10} mol/m^3 , which is not impossible.

Conclusions

We demonstrated that CNF could be loaded with 10 wt% nickel via incipient wetness impregnation and deposition precipitation. But only when pre-oxidized fibers are used thermally stable nickel particles can be obtained. Pre-oxidation appears necessary to provide interaction between the polar precursor compounds and the carbon surface as well as after reduction between the metallic nickel phase and the carbon nanofiber surface (surface oxygen atoms) up to elevated temperatures. Catalyst precursors thus prepared can be fully reduced already at 573 K and sintering in hydrogen during reduction at 773 K is highly suppressed.

The low reduction temperature of 573 K means a significant advantage of such Ni/CNF catalysts over oxide supported nickel catalysts that generally demand reduction temperatures up to 900 K or higher.

Measurements of the methanation of CO using 10 wt% Ni/CNF-ox catalyst show that CH₄ production starts at low temperatures, here at 500 K, but that the water-gas shift reaction contributes to the CO conversion from 550 K and above. It turned out that under methanation condition some sintering occurs, which leads to deactivation. This deactivation cannot be explained fully by loss of surface alone due to sintering but also might originate from facetation during growth of the originally small, spherical nickel particles.

Sintering is related to the formation of nickel carbonyl and follows the mechanism of Ostwald ripening. Results show a linear relation between $\ln(\bar{r}/\bar{r}_0)$ and $\ln(t)$ with a slope of 0.31 ± 0.06 . This value includes the theoretical value of 0.33 as proposed by Ardell for a dimensionality of 2 and 3 for particle growth as well as carbonyl transport. The steady state concentration of nickel carbonyl depends on its formation and dissociation. Since there is no significant loss of nickel demonstrable during dynamic sinter experiments the nickel carbonyl formation rate must be the rate determining step, causing a maximal nickel carbonyl concentration which is at least 1000 times smaller than the thermodynamic equilibrium concentration as calculated from thermodynamics. From the particle growth rate observed, the change in average radii with time (dr/dt) we estimate that the nickel carbonyl concentration in the reactor must have been in the order of 10^{-10} mol/m³.

Acknowledgments

The authors acknowledge H. van der Wiel for execute all chemical sinter experiments; C. van der Spek and J.W. Geus for performing the TEM measurements; O.L.J. Gijzeman and W.K. Kegel for helpful discussions about Oswald ripening and diffusion processes and the financial support of STW (grant UPC 5487).

References

1. Bartholomew, C.H., Sorensen, W.L., *J. Catal.*, (1983), 81, 131.
2. Flynn, P.C., Wanke, S., *J. Catal.* (1975), 37, 432.
3. Geus, J.W., in: *Sintering and Catalysis*, (Kuczynski, G.C., Ed.), Material Science Research, Plenum Press, New York, (1975), 10, 29.
4. Frank, J.P., Martino, G., in: *Progress in Catalyst Deactivation*, NATO Advances Study Institute series E, (Figueiredo, J.L., Ed.), Nijhoff, Boston, (1982), 54, 355.
5. Oudet, F., Vejux, A., Courtine, P., *Appl. Catal.*, (1989), 50, 79.
6. Chen, J., Heck, R.M., Farrauto, R.J., *Catal. Today*, (1992), 11, 517.
7. Heck, R.M., Farrauto, R.J., in: *Catalytic Air Pollution Control*, Van Nostrand Reinhold, New York, (1995), 65.
8. Bartholomew, C.H., in: *Catalyst Deactivation (1994)*, *Stud. Surf. Sci. Catal.*, Elsevier, Amsterdam, (1994), 88, 1.
9. Forzatti, P., Lietti, L., *Catal. Today*, (1999), 52, 165.
10. Rostrup-Nielsen, J.R., in: *Catalysis, Science and Technology*, (Anderson, J.R., Boudart, M., Eds.), Springer, Berlin, (1984), 5, Chap. 1.
11. Rostrup-Nielsen, J.R., Sehested, J., Nørskov, J.K., *Adv. Catal.*, (2002), 47, 65.
12. Richardson, J.T., Crump, J.G., *J. Catal.*, (1979), 57, 417.
13. Teixeira, A., Giudici, R., *Chem. Eng. Set.*, (1999), 54, 3609.
14. Kuo, H.K., Ganesan, P., Deangelis, R.J., *J. Catal.*, (1980), 64, 303.
15. Bartholomew, C.H., Sorensen, W.L., *J. Catal.*, (1983), 81, 131.
16. Bartholomew, C.H., *Appl. Catal. A.*, (1993), 107, 1.
17. Sehested, J., Carlson, A., Janssens, T.V.W., Hansen, P.L., Datye, A.K., *J. Catal.*, (2001), 197, 200.
18. Sehested, J., *J. Catal.*, (2003), 217, 417.
19. Richardson, J.T., Propp, J.L., *J. Catal.*, (1986), 98, 457.
20. Rasmussen, F.B., Sehested, J., Teunissen, H.T., Molenbroek, A.M., Clausen, B.S., *Appl. Catal.*, (2004), 267, 165.
21. Bartholomew, C.H., Pannel, R.B., Fowler, R.W., *J. Catal.*, (1983), 79, 83.
22. Sehested, J., Gelten, J.A.P., Remediakis, I.N., Bengaard, H., Nørskov, J.K., *J. Catal.*, (2004), 223, 432
23. Coenen, J.W.E., *Stud. Surf. Sc. Catal.*, (1979), 3, 89.
24. Van Stiphout, P.C.M., Stobbe, D.E., V.D. Scheur, F.T., Geus, J.W., *Appl. Catal.*, (1988), 40, 219.
25. Shen, W.M.; Dumesic, J.A., Hill, C.G. Jr., *J. Catal.*, (1981), 68, 152.
26. Vannice, M.A., Garten, R.L., *J. Catal.*, (1979), 56, 230.

27. Agnelli, M., Kolb, M., Mirodatos, C., *J. Catal.*, (1994), 148, 9.
28. Van Stiphout, P.C.M., PhD thesis, Utrecht University, Utrecht, The Netherlands, (1987).
29. De Groot, P., Coulon, M., Dransfeld, K., *Surf. Sci.*, (1980), 94, 204.
30. Serp, P., Kalck, P., Feurer, R., *Chem. Rev.*, (2002), 102, 3085.
31. De Jong, K.P., Geus, J.W. *Catal. Rev.-Sci. Eng.*, (2000), 42, 481.
32. Baldan, A., *J. Mat Sci.*, (2002), 37, 2171.
33. Landau, L.D., Lifshitz, E.M., Pitaevski, L.P., *Kinet. Phase Trans.*, (1981), 12, 427.
34. Lifshitz, I.M., Slyozov, V.V., *J. of Phys. Chem. Solids*, (1961), 19, 35.
35. Chakraverty, B.K., *J. Phys. Chem. Solids*, (1967), 28, 2401.
36. Ardell, A.J., *Mater. Sci. Eng.*, (1997), 238, 108.
37. Van Dillen, A.J., Geus, J.W., Hermans, L.A.M., Van der Meijden, J.J., *Proc. Int. Congr. Catal.*, (1977), 2, 677.
38. Toebes, M.L., Van der Lee, M.K., Tang, L.M., Huis in 't Veld, M.H., Bitter, J.H., Van Dillen, A.J., De Jong, K.P., *J. Phys. Chem. B.*, (2004), 108, 11611.
39. Bitter, J.H., Van der Lee, M.K., Slotboom, A.G.T., Van Dillen, A.J., De Jong, K.P., *Catal. Lett.*, (2003), 89, 139.
40. HSC Chemistry 4.2 for windows, Outokumpu Research Oy, Pori, Finland, A Roine.
41. Genin, P., Delahaye-Vidal, A., Portemer, F., Tekaia-Elhsissen, K.; Figlarz, M., *Eur. J. Solid State and Inorganic Chem.*, (1991), 28, 505.
42. Silva, L.M.S., Orfao, J.J.M., Figueiredo, J.L., *Appl. Catal., A.*, (2001), 209, 145.
43. Van Meerten, R.Z.C., Beaumont, A.H.G.M., Van Nisselrooij, P.F.M.T., Coenen, J.W.E., *Surf. Sci.*, (1983), 135, 565.
44. Bartholomew, C.H., Pannell, R.B., Butler, J.L., *J. Catal.*, (1980), 65, 335.
45. "The dynamical character of adsorption", De Boer, J.H., Oxford, (1953).
46. Carman, P.C., Raal, F.A., *Math. Phys. Sci.*, (1951), 209, 38.
47. Handbook of chemistry and physics, Lide, D.R. (Eds.), 78th edition (1998).
48. Golden, T.C., Hsiung, T.H., Snyder, K.E., *Ind. Eng. Chem. Res.*, (1991), 30, 502.
49. Mazurek, H., Mehta, R.S., Dresselhaus, M.S., Dresselhaus, G., Zeiger, H.J., *Surf. Sci.*, (1982), 118, 530.
50. Trivin, H., Bonnetain, L., *Compt. Rend. (Paris)*, 1970, C 270, 13.

6_A

Summary and concluding remarks

Carbon nanofibers (CNF) are promising catalyst support materials due to their physico-chemical properties. The material combines the advantages of graphite and active carbon. CNF are strong, pure, inert, non microporous and have a high surface area (100-200 m²/g). In addition the reclaim of metals supported on CNF is easy via oxidation of the support. Nevertheless some doubts were raised about the suitability of CNF. In particular the bulk density of the materials was claimed to be too low to be suitable for a commercial application. In the current study we explored routes to obtain dense carbon nanofibers bodies suitable as catalyst support. This work is described in chapter two. Next new routes to the deposition of nickel on carbon nanofibers we investigated (chapter 3 and 4). Finally the stability of Ni/CNF catalysts in CO atmospheres, relevant for the use of these catalysts during methanation of synthesis gas, was studied and described in chapter 5.

The carbon nanofibers used in this research were catalytically grown using Ni/SiO₂ growth catalysts and a mixture of carbon monoxide and hydrogen as carbon containing growth gas. CNF growth was performed at 773 K and results in fish-bone (herring-bone) type of carbon nanofibers. In this type of fiber the graphene sheets are orientated with an angle with respect to the central axis of the fiber. Depending on the properties of the growth catalysts (see chapter 2) the fibers have uniform diameters ranging from 10 to 30 nm and lengths up to 1000 micrometer. The individual fibers entangle to form macroscopic bodies. The degree of entanglement determines the density and strength of the bodies.

In Chapter 2 we show that the macroscopic properties i.e., mechanical strength and the bulk density of those carbon nanofiber bodies can be tuned via the metal loading of nickel in the Ni/SiO₂ growth catalyst. A metal loading of 20 wt% resulted in CNF bodies with a bulk density of 0.9 g/ml and a bulk crushing strength of 1.25 MPa. Low loaded Ni/SiO₂ growth catalysts (5 wt%) resulted in fiber bodies with a lower density (0.4 g/ml). This was related to a difference in the growth mechanism of the low and high density CNF bodies. When using 5 wt% nickel growth catalyst the sintering of the metal particles preceding the growth was less significant compared to that in the 20 wt% Ni catalyst. Therefore from the 20 wt% Ni catalyst carbon nanofibers were grown with a larger diameter (~22 nm). These fibers grow discontinuous in a “rice shell” resulting in highly interwoven fibers with a high density. The thinner fibers (~12 nm) from the 5 wt% Ni/SiO₂ catalyst grow in a continuous straight manner resulting in less entanglement of the fibers thus a lower density and mechanical strength.

Due to the inertness of CNF, which is advantage during catalytic operation of these materials, the deposition of a metal is challenging. In order to apply nickel on the inert carbon nanofibers oxygen containing groups were introduced via oxidation (H₂SO₄/HNO₃). In chapter 3 two preparation methods are described, incipient wetness impregnation and deposition precipitation for depositing nickel on the oxidized CNF. Both methods are widely used, however deposition precipitation is in general used in combination with oxidic supports while incipient wetness impregnation can be applied on a broad spectrum of support types. The reason why deposition precipitation is thought to be only successful in combination with oxidic supports originates from the mechanism of this process. It is thought that it is essential to form a mixed phase between metal precursor and support and this is only possible for oxidic supports, not for carbon. However we showed that also with CNF deposition precipitation can be successfully applied. We succeeded in preparing a 45 wt% Ni/CNF catalyst with a narrow nickel metal particle size distribution centered around 9 nm. Incipient wetness impregnation can also yield highly dispersed metallic nickel

catalysts (Ni particle size 7 nm) but only up to 10 wt% of nickel. For both techniques, i.e., impregnation and deposition precipitation, the presence of oxygen groups on the surface of the CNF support is essential in order to form well-dispersed thermally stable nickel particles.

In chapter 4 a detailed study is reported on the mechanism of deposition precipitation of nickel onto carbon nanofibers and the role of the oxygen groups in that process. Three types of carbon nanofibers were used. All were of the fishbone CNF but vary in the nature and number of oxygen surface groups. One type of CNF contained mainly carboxylic groups (CNF-ox), one with mainly alcohol type of groups (CNF-OH) and the last type with mainly basic type of oxygen containing surface groups (CNF-B). During the deposition precipitation process the pH increases from acid to neutral. As a result of that the negative charge on the CNF surface increases. The interaction between $\text{Ni}^{2+}(\text{aq})$ and the deprotonated negatively charged carboxylic acid surface groups (COO^-) present on CNF-ox leads to ion adsorption on the fiber surface. It turns out that this nickel adsorption is essential to yield well-dispersed Ni/CNF catalysts. We found that oxygen containing surface groups with higher pK_a values compared to carboxylic acid surface groups e.g., alcohol type (CNF-OH) or other basic types (CNF-B) are not involved in this adsorption step. This results, after reduction, in large nickel particles some of them not even attached to the support. The adsorption is the first step in the deposition precipitation process. The second step is the growth of nickel hydroxide plates, which takes place at the adsorbed nickel species and results in an anchored nickel hydroxide phase. Since on the CNF-ox a large number of anchoring sites (COO^-) were present a large number of nickel ions were adsorbed which results in a large number of small nickel-hydroxide phases, yielding after reduction small nickel particles.

The catalytic activity for methanation of 10 wt% Ni/CNF-ox is reported in chapter 5. Methanation is the conversion of synthesis gas, CO and H_2 to methane. It is shown that the intrinsic surface activity of the catalyst is comparable to Ni/ SiO_2 (at atmospheric pressure), which indicated that the CNF support does not have an effect on the activity of the nickel. During methanation for 90 hours at 523 K a deactivation of the catalyst was observed. This could be related to sintering of the Ni particles i.e., a loss of active surface area. Therefore the sintering process either thermally or chemically was studied in detail. Metallic nickel particles supported on CNF-ox are thermally stable in hydrogen up to 773 K. Therefore, the loss of catalytic activity of nickel must be due to chemical sintering i.e., Ostwald ripening via the formation and transport of nickel carbonyl which results in a decrease of the active nickel surface area and facetation of the growing nickel particles. A detailed description of the process for the Ni/CNF catalysts is given in chapter 5.

6_B

Samenvatting en conclusies

Kooldraden zijn een veelbelovend materiaal voor gebruik als katalysatordrager door hun speciale fysische en chemische eigenschappen. Ze combineren de voordelen van grafiet en actieve kool in één soort materiaal. De kooldraden zijn sterk, inert, niet microporeus en hebben een hoog specifiek oppervlak per gram materiaal (100-200 m²/g). Tevens is het mogelijk om zuurstofhoudende groepen op het oppervlak van deze kooldraden te introduceren zodat het aanbrengen van het katalytisch actieve metaal wordt vereenvoudigd. Toch bestaan er twijfels over de toepasbaarheid van kooldraden. In het bijzonder de bulkdichtheid van deze materialen bleek in veel gevallen te laag om in commerciële processen te worden toegepast. In deze studie hebben we syntheseroutes onderzocht om kooldraden te ontwikkelen met een hoge bulkdichtheid, zodat ze geschikt zijn als katalysatordragermateriaal. Dit werk is beschreven in hoofdstuk 2. Vervolgens zijn nieuwe syntheseroutes

ontwikkeld voor het aanbrengen van metallisch nikkel op de kooldraden (hoofdstuk 3 en 4). Uiteindelijk is de stabiliteit van de nikkel-op-kooldraden katalysator getest in een koolmonoxide atmosfeer, aangezien deze katalysator werd ontworpen voor de omzetting van synthesegas (koolmonoxide en waterstof) tot methaan. Deze studie is beschreven in hoofdstuk 5.

De kooldraden die in dit onderzoek gebruikt zijn, zijn katalytisch gegroeid met behulp van een groeikatalysator bestaande uit Ni/SiO₂. Kooldradengroei vond plaats door een mengsel van koolmonoxide- en waterstofgas over de groeikatalysator te leiden bij een temperatuur van 773 K. De gevormde kooldraden hebben een “visgraat” structuur, dat wil zeggen dat de grafietlagen waaruit de kooldraad is opgebouwd een hoek maken ten opzichte van de lengteas van de kooldraad. Afhankelijk van de eigenschappen van de groeikatalysator (zie hoofdstuk 2) hebben de draden een diameter tussen 10 en 30 nanometer en een lengte tot ongeveer 1000 micrometer. De individuele kooldraden verweven tijdens het groeien en vormen zo macroscopische kooldraadlichamen. De mate waarin de kooldraden in elkaar zijn verweven en raken bepaalt de dichtheid en mechanische sterkte van de lichamen.

In hoofdstuk 2 tonen we aan dat de macroscopische eigenschappen zoals de sterkte en dichtheid van kooldraadlichamen kunnen worden gestuurd tijdens de groei via de belading van het nikkel in de Ni/SiO₂ groeikatalysator. Een belading van 20 massa% nikkel resulteert in kooldraadlichamen met een bulkdichtheid van 0.9 g/ml en een sterkte van 1.25 MPa. Laag beladen groeikatalysatoren (5 massa% nikkel-op-silica) resulteren in kooldraadlichamen met een lagere dichtheid, namelijk 0.4 g/ml. Dit fenomeen, het verschil in dichtheid door verschillende metaalbeladingen, ontstaat door verschillende mechanismen van de kooldraadgroei. Wanneer de 5% groeikatalysator werd gebruikt was de sinterring, het samensmelten van meerdere deeltjes tot één groter deeltje, van het nikkel voorafgaand aan de kooldradengroei significant minder vergeleken met de sinterring van nikkeldeeltjes op de 20 massa% groeikatalysator. Daardoor vormt deze laatste groeikatalysator dikkere kooldraden (~ 22 nm). Deze kooldraden groeien niet continu in de tijd maar via het “rice shell” mechanisme – *groeien, stoppen, groeien, stoppen, etc.* – wat ervoor zorgt dat de kooldraden sterk in elkaar zijn geweven en dus resulteert in hoge bulkdichtheid kooldraadlichamen. Dunnere draden gegroeid met de 5% nikkel groeikatalysator, groeien wel continu en zijn minder in elkaar geweven. Deze zijn hierdoor minder sterk en hebben een lagere bulkdichtheid.

Omdat de kooldraden inert zijn, wat een voordeel is indien het materiaal gebruikt wordt als katalysatordragermateriaal, is het moeilijk om er een metaal aan te hechten. Om nikkeldeeltjes te hechten aan de kooldraden worden

zuurstofhoudende groepen op het oppervlak van de kooldraden geïntroduceerd via een oxidatieve behandeling in een mengsel van geconcentreerd salpeterzuur en zwavelzuur. In hoofdstuk 3 worden twee technieken beschreven om nikkel op de kooldraden af te zetten, impregnatie en depositie-precipitatie. Beide methoden worden veel gebruikt, echter depositie-precipitatie wordt in het algemeen gebruikt in combinatie met oxidische dragermaterialen. Impregnatie is een techniek welke gebruikt wordt op een breed spectrum van verschillende dragermaterialen. De reden waarom wordt gedacht dat depositie-precipitatie alleen succesvol kan worden gebruikt in combinatie met oxidische dragermaterialen komt voort uit het mechanisme van dit proces. Aangenomen wordt dat het essentieel is dat tijdens dit proces een verbinding ontstaat tussen drager en metaalhydroxide wat alleen mogelijk is uitgaande van oxidische katalysator dragers en niet met koolstof. Echter wij hebben aangetoond dat het wel mogelijk is om nikkel op kooldraden af te zetten via deze depositie-precipitatie techniek. Op deze manier kon een 45 massa% nikkel-op-kooldraden katalysator gemaakt worden waarin de uiteindelijke nikkeldeeltjes gemiddeld 9 nanometer groot zijn. De impregnatie techniek kan ook leiden tot goed verdeeld metallisch nikkel op kooldraden, hierbij zijn de nikkeldeeltjes ongeveer 7 nanometer in diameter groot. Echter deze katalysatorbereiding is alleen succesvol tot een belading van circa 10% nikkel. Voor beide technieken, impregnatie en depositie-precipitatie geldt dat de aanwezigheid van zuurstofhoudende groepen op het oppervlak van de kooldraden essentieel is voor het verkrijgen van goed verdeelde nikkeldeeltjes welke ook thermisch stabiel zijn.

In hoofdstuk 4 is een gedetailleerd mechanisme beschreven van depositie-precipitatie van nikkel op kooldraden en de belangrijke rol die de zuurstofhoudende groepen op het oppervlak van de kooldraden hierbij spelen. Voor dit onderzoek zijn drie typen kooldraden gebruikt. Allemaal “visgraat” type kooldraden maar met verschillen in soort en aantal zuurstof bevattende groepen. Een type kooldraden welke voornamelijk carboxylzuurgroepen aan het oppervlak bevat (CNF-ox), een type met voornamelijk alcoholgroepen (CNF-OH) en een type met voornamelijk basische groepen (CNF-B). Depositie-precipitatie start vanuit een zure oplossing waarna gedurende de eerste periode de pH van de oplossing stijgt naar neutraal. De interactie tussen $\text{Ni}^{2+}(\text{aq})$ en de gedeprotoneerde, negatief geladen, carboxylzuurgroepen (COO^-) aanwezig op de CNF-ox kooldraden leiden tot adsorptie van nikkelionen. Het is aangetoond dat deze adsorptie van nikkelionen essentieel is voor het goed verdelen en verankeren van nikkel op en over de kooldraden. Verder hebben we aangetoond dat zuurstofhoudende groepen met een hogere pK_a waarde dan carboxylzuurgroepen zoals alcohol (CNF-OH) of andere typen basische groepen

(CNF-B) niet betrokken zijn bij de ion-adsorptie. Dit laatste leidt na reductie van het nikkeldhydroxide tot grote nikkelfragmenten welke veelal niet aan de dragers vastzitten. Na de adsorptie volgt de groei van nikkeldhydroxide. De vorming van het plaatvormige nikkeldhydroxide vindt plaats op geadsorbeerde nikkelionen en resulteert in een verankerde nikkeldhydroxide fase. Aangezien de CNF-ox kooldraden een groot aantal carboxylzuurgroepen bezit resulteert depositie-precipitatie in een goede verdeling van het nikkel en na reductie van het hydroxide tot kleine metallische nikkeldeeltjes.

De katalytische activiteit van de 10% nikkel-op-kooldraden is getest voor de vormingsreactie van methaan uit synthesegas (CO en H₂). De intrinsieke activiteit per oppervlakteatoom, de zogenaamde “turn over frequency (TOF)”, verschilt niet met die van nikkel-op-silica welke een goede methanisatie katalysator is. Dit geeft aan dat de kooldraden geen negatieve effecten hebben op de activiteit van de katalytisch actieve fase. Tijdens het methaniseren met de 10% nikkel-op-kooldraden katalysator (90 uur bij 523 K) werd een deactivatie van de katalysator waargenomen. Dit kan het gevolg zijn van sintering, het verlies van actief oppervlak doordat kleine nikkeldeeltjes samenklonteren en één groter deeltje vormen. Hiertoe is zowel het thermische als chemische sintergedrag van nikkel-op-kooldraden onderzocht. Metallische nikkeldeeltjes op zuurstofgroepen bevattende kooldraden zijn in waterstof milieu thermisch stabiel tot 773 K. Dus is het verlies van activiteit afkomstig van chemische sintering. Chemische sintering vindt plaats via “Ostwald ripening”, de vorming en transport van nikkel carbonyl vanaf de kleine nikkeldeeltjes naar de grote deeltjes leidt tot facettering van de grote deeltjes en een verlies aan actief metaal oppervlak. Een gedetailleerde beschrijving van deze processen is gegeven in hoofdstuk 5.

Dankwoord

Nu is dan eindelijk het moment aangebroken dat ik iedereen kan bedanken voor de hulp die ik heb gehad tijdens mijn promotieonderzoek en natuurlijk ook tijdens het schrijven van dit proefschrift.

Allereerst mijn promotor Krijn de Jong, Krijn het is als de dag van gisteren dat we samen in overleg waren of ik deze promotiestap zou maken. Het onderwerp dat je me aanbood, het methaniseren van koolmonoxide heeft me gedurende mijn promotieonderzoek altijd geboeid. Natuurlijk, wil ik bijna zeggen. Maar ik had ook wel eens twijfels. Op die momenten dat het even niet liep zoals ik het wilde, wist je me altijd weer te motiveren. Indien nodig bood je direct de helpende hand en werden er spijkers met koppen geslagen. Je enorme enthousiasme als ik je nieuwe TEM beelden toonde zal ik niet gauw vergeten. Zeker niet die keer na het zien van nikkelhydroxide plaatjes aan de kooldraden. Krijn bedankt! Zonder jou hulp en ideeën was dit proefschrift niet geweest wat het nu gelukkig geworden is.

Harry Bitter, mijn copromotor en projectleider van dit promotieonderzoek, natuurlijk wil ik ook jou bedanken. Je hebt het project in goede banen geleid en gaf me goede aanwijzingen en leerzame tips. Ik liep vaak bij je binnen om van gedachte te wisselen over allerlei zaken, vaak wetenschappelijke maar ook gewoon voor de gezelligheid. Veel hebben we gesproken over mijn methanisatie-opstelling, resultaten van metingen, presentaties voor STW, NCCC en Carbon maar vooral over het groei-mechanisme van kooldraden met een hoge en lage dichtheid. Het is een materiaal waar we nog lang niet alles van weten, hoewel we er wel steeds meer van begrijpen. Dankzij jouw hulp kan ik nu het dankwoord schrijven en is het proefschrift nu een feit. Genoeg over de wetenschap, naast projectleider was je ook een gezellige collega. Harry fijn dat je deur altijd open stond... of was dat voor het uitzicht? In ieder geval heb je me ook nog kreeft zonder slap leren eten! Kortom, Harry bedankt voor alles het was een gezellige en leerzame tijd!

Jos van Dillen, natuurlijk wil ik ook jou heel hartelijk bedanken voor alle wetenschappelijke discussies en inzet die hebben bijdragen aan dit onderzoek. Onze samenwerking leidde veelal tot nieuwe ideeën en inzichten welke nodig waren om het model van thermische en chemische sintering uit te werken, 2-D of 3-D? Fijn dat je altijd tijd vrij wilde maken als ik je weer eens (even...) nodig had.

John Geus ook jouw wil ik bedanken voor de prettige, zeer leerzame samenwerking en natuurlijk ook voor alle moeite die je hebt gedaan om zoveel mooie TEM en SEM foto's te maken. We hebben vele uren achter de microscopen gezeten en de samenwerking was altijd goed. De brand in het Kruitgebouw leek even "roet in het eten" te gooien, maar gelukkig werden de microscopen vernieuwd en wist je al snel weer de knoppen te bedienen. John bedankt ook voor al je enthousiasme, het werkte motiverend!

Mijn kamergenoten wil ik bedanken voor de gezelligheid. Naast wetenschap was er ook tijd voor gezellige "koffie praat". Er was altijd wel wat gebeurd om over te praten en te lachen, of niet, maar dan wisten we nog wel iets anders. Immers het was altijd "feest" in N205. Ja toch Rudy, je zult mijn muziek nog gaan missen of blijf je gewoon bij je "zware metalen"? Ik wil je voordragen voor een "EHBC" nominatie als die bestaat tenminste! Je Eerste Hulp Bij Computer-problemen is namelijk geweldig en dat heeft me heel wat kostbare tijd gescheeld. Je wist wel een oplossing, of dook gelijk het Internet op om naar een oplossing te zoeken. Rudy ook wens ik je veel succes met de "laatste loodjes" van je onderzoek en dan het schrijven van je boekje. Rudy succes en houdoe...

Bibi bedankt voor de gezelligheid en alle (kilo's?) snoepjes die je wekelijks meebracht. Ik geloof overigens dat er samen met mij heel wat meer mensen je hiervoor dankbaar zijn, of zouden moeten zijn. Immers "onze" snoeppot, die van jou dus eigenlijk, wisten velen goed te vinden. Sinds je met deze traditie begon, is het in onze kamer nog nooit zo druk geweest. Niet alleen AIO's, maar ook stafleden (wees gerust ik noem geen namen) kwamen steeds vaker even iets vragen of liepen zomaar even binnen. Bibi veel plezier en succes in je nieuwe baan.

"Daphne, trein van 17:34?" Zo spraken we vaak af als we na de koffie van 15.00 uur weer aan het werk gingen. We hebben heel wat samen gereisd en veel gelachen. In de trein was er altijd wel een onderwerp om over te kletsen. Daphne veel succes met je promotieonderzoek en nu je in de eindfase bent ook succes met het schrijven. Doe Olaf de hartelijke groeten en wens hem ook veel succes.

Laurens leuk om je hotel-kamergenoot te zijn, van het NCCC in Noordwijkerhout tot de NIOK cursus in Schiermonnikoog het was altijd gezellig. Ook hebben we enorm gelachen bij onze eerste BHV oefening, de deurprocedure! En later natuurlijk nog het brand blussen voor gevorderden, de één hand procedure waar jij voor slaagde. Je gesponsorde verjaardag zal ik niet snel vergeten, zeker Albert Heijn of was het Page als hoofdsponsor? Bedankt voor de gezelligheid Laurens, succes bij Corus en uh... nog plannen met de vrouw dit weekend?

Dan mijn “buufjes”, dames bedankt voor alles, van koffie tot faxen, van nietjes tot afspraken plannen alles was zo geregeld en nog tijd voor gezelligheid ook, Monique en Dymph bedankt!

Mijn studenten, Arnold, Hanneke, Bas en Vincent bedankt voor jullie werk en inzet. Jullie behaalde resultaten hebben bijgedragen aan de inhoud van dit proefschrift. Het was fijn om gemotiveerde studenten te begeleiden, bedankt voor jullie inzet en succes.

Op de “Uni” wil ik verder al mijn collega’s, ex-collega’s, postdocs, vaste vakgroepmedewerkers, de staf, de glasblazerij en de audiovisuele dienst bedanken voor alle gezelligheid en leuke werksfeer, die vooral tot uitdrukking kwam tijdens de koffiepauzes, LIIT’s en BBQ’s, en de hulp die ik in de afgelopen jaren heb gekregen.

Tot slot, maar zeker niet in de laatste plaats bedank ik mijn ouders, broers en zus en mijn schoonfamilie. Pa en Ma, jullie hebben altijd willen begrijpen wat ik aan het doen was, hoe het in zijn werk gaat om van biomassa aardgas te maken en hoever ik al was gevorderd met mijn werkzaamheden, zonder jullie steun en liefde was ik nooit zo ver gekomen. Lieve Monique fijn dat je me hebt gesteund in mijn werk, vooral tijdens die momenten dat het niet ging zoals ik dat graag wilde. Zonder jouw hulp, liefde en vertrouwen was het niet gelukt.

Inge we houden van je, je bent ons wonder!

Martijn

